A SATELLITE AND ASH TRANSPORT MODEL AIDED APPROACH TO ASSESS THE RADIATIVE IMPACTS OF VOLCANIC AEROSOL IN THE ARCTIC

A Dissertation
Presented to
The Academic Faculty

by

Cindy L. Young

In Partial Fulfillment
of the Requirements for the Degree
Doctor of Philosophy in the
School of Earth and Atmospheric Sciences

Georgia Institute of Technology
May 2014

A SATELLITE AND ASH TRANSPORT MODEL AIDED APPROACH TO ASSESS THE RADIATIVE IMPACTS OF VOLCANIC AEROSOL IN THE ARCTIC

Approved by:

Dr. Josef Dufek, Advisor
School of Earth and Atmospheric Sciences
Georgia Institute of Technology

Dr. James Wray
School of Earth and Atmospheric Sciences
Georgia Institute of Technology

Dr. Irina Sokolik
School of Earth and Atmospheric Sciences
Georgia Institute of Technology

Dr. Athanasios Nenes
School of Chemical and Biomolecular Engineering
Georgia Institute of Technology

Dr. Christian Huber
School of Earth and Atmospheric Sciences
Georgia Institute of Technology

Dr. Judith Curry
School of Earth and Atmospheric Sciences
Georgia Institute of Technology

Date Approved: 1/6/2014

To all of my teachers, both in academics and in life.

“You cannot teach a man anything; you can only help him find it within himself.”
--Galileo Galilei

“Listen to the mustn'ts, child. Listen to the don'ts. Listen to the shouldn'ts, the impossibles, the won'ts. Listen to the never haves, then listen close to me... Anything can happen, child. Anything can be.”
--Shel Silverstein

ACKNOWLEDGEMENTS

I would like to thank my academic advisors, Dr. Irina Sokolik and Dr. Josef Dufek, for their support and guidance. I thank the faculty and staff of the Department of Earth and Atmospheric Sciences, especially: Dr. Ellery Ingall and Ms. Meg Grantham for their mentorship over the years, Dr. Carol Paty for sound advice, Dr. James Wray for allowing my mind to travel to distant moons sometimes, Dr. Judith Curry for her help and support, and all of the committee members who helped review this dissertation. I also thank the students I have taught over the years for helping me to become a better teacher, and I acknowledge Dr. Mark Flanner at the University of Michigan for the use of the SNICAR model. I give a special thanks to my fellow graduate students, both current and past, and to my group mates: Jennifer Telling, Ozge Karakas, Mary Benage, Xin Xi, Zheng Lu, Joe Estep, Josh Mendez, Taryn Black, Wim Degruyter, and Leah Courtland.

To Dr. Jennifer Telling, I extend the warmest of thanks. I am not sure where I would be without her love and friendship, which keeps my life balanced and bearable. Mr. John Bumgarner, who fed me dinner and bubble tea while writing this document, I thank for loving and supporting me in so many ways throughout the years. I do not know what I would have done without it. I would also like to thank my family and John's family for their encouragement and understanding. I especially would like to remember my grandparents who have passed away: Ms. Betty Henderson and Mr. Pat Young. I would like to honor the grandparents I have who are still living: Mr. George Henderson and Ms. Opal Young. It has been through their loving-kindness and continued faith in me that I have been able to achieve my goals.

My K-12 teachers deserve my eternal gratitude. From the DoD schools in the Far East, to Union County School Systems in Georgia, to Young Harris College and Piedmont College, I received excellent instruction and was inspired. For my K-12 friends, I am forever grateful, for they helped foster in me the audacity to follow my dreams. I also thank all of my friends in the Shaolin Tai Chi and Kung Fu Club, both present and past members, especially Dr. Tracy Westeyn Brown and Master Tremayne Brown. Additionally, I thank all of my friends in the Yellow Jacket Flying Club and the friends and family I have been blessed to know at Many Forks Baptist Church.

Not to be forgotten are my cats: Marlee, Kyra, Sven, Skyler, Sylvan, Stella, Oliver, and Sage (passed), who are rock stars. Their daily companionship and love has kept me grounded throughout the years. Finally, I am thankful for the promise that I can do all things through Christ who strengthens me.

TABLE OF CONTENTS

LIST OF TABLES

LIST OF FIGURES

LIST OF ABBREVIATIONS

AI	Aerosol Index
AOD	Aerosol Optical Depth
AVO	Alaska Volcano Observatory
CALIOP	Cloud-Aerosol with Orthogonal Polarization
CALIPSO	Cloud-Aerosol Lidar and Infrared Pathfinder Satellite Observations
CVO	Cascades Volcano Observatory
DARF	Direct Aerosol Radiative Forcing
DARFE	Direct Aerosol Radiative Forcing Efficiency
$DARFE_{atm}$	Direct Aerosol Radiative Forcing Efficiency of the atmosphere
$DARFE_{surface}$	Direct Aerosol Radiative Forcing Efficiency at the surface
$DARFE_{TOA}$	Direct Aerosol Radiative Forcing Efficiency at the top of the atmosphere
DISORT	Discrete Ordinate Radiative Transfer
FAA NEXRAD	Federal Aviation Administration Next Generation Weather Radar
GCM	General Circulation Model
HR	Heating Rate
HYSPLIT	HYbrid Single-Particle Lagrangian Integrated Trajectory
LW	Longwave
MFR	Mass Flow Rate
MODIS	Moderate Resolution Imaging Spectroradiometer
NASA	National Aeronautics and Space Administration
NOAA/OAR/ESRL PSD	National Oceanic and Atmospheric Adminstration
OAR	Office of Oceanic and Atmospheric Research
ESRL	Earth Science Research Laboratory

PSD	Physical Sciences Department
NRCS	Natural Resources Conservation Service
NWS	National Weather Service
OMI	Ozone Monitoring Instrument
OPAC	Optical Properties of Aerosols and Clouds
SBDART	Santa Barbara Disort Atmospheric Radiative Transfer model
SNICAR	SNow, ICe , and Aerosol Radiative model
SNOTEL	SNow TELemetry
SW	Shortwave
SWE	Snow Water Equivalent
SZA	Solar Zenith Angle
TOA	Top Of the Atmosphere
USGS	United State Geological Survey
UTC	Coordinated Universal Time
UV	Ultraviolet
VATDM	Volcanic Ash Transport and Dispersion Model
WRF-Chem	Weather Research Forecasting model coupled with Chemistry

LIST OF SYMBOLS

A	Suzuki coefficient
A_{vent}	Area of the volcanic vent
C	Scaled average concentration
C_d	Drag coefficient
c_p	Specific heat
d	equal volume sphere
d_n	average between the minimum and maximum axis
F_{down}	Downward radiative flux
F_{net}	Net radiative flux
$F_{net.\ total}$	Sum of net shortwave and longwave radiative fluxes
$F_{net,\ LW}$	Net longwave radiative flux
$F_{net,\ SW}$	Net shortwave radiative flux
F_{up}	Upward radiative flux
H	Maximum plume height
H_{event5}	Maximum plume height for the event 5 eruption
K_1	Shape factor
K_2	Shape factor
K_e	Normalized extinction coefficient
K_X, K_Y, K_Z	Diagonal terms of the scaled eddy diffusivity tensor
M	Snowmelt
MFR_{event5}	Mass Flow Rate for the event 5 eruption
m_Q	Physical constant converting radiation to Snow Water Equivalent
N	Number of model grid points for which measured loadings were available

n_c	particle number concentration
r	particle radius (equation 2.1)
r	Constant restricted degree-day factor (equation 4.1)
R	Specific gas constant
Re	Reynolds number
R_{eff}	Effective radius
S(z)	Vertical mass distribution function
S_*	Scaled average source term
S_0	Normalization factor
T	Plume temperature
T_d	Daily mean temperature
V_X, V_Y,V_Z	Scaled average wind speed
W_{0k}	Deposit loading at point k for the measured samples
W_k	Deposit loading at point k for the model simulation
X	Gas mass fraction
Z	Column altitude
Δ	Metric for determining the difference between measured and modeled loadings
δ	Dirac's distribution for filiform and instantaneous release
ε_p	Particle volume fraction
λ	Dimensionless parameter
ν	Velocity
ρ	Air density
ρ_*	Scaled average atmospheric density
ρ_g	Density of the gas
ρ_p	Particle density

σ	Variance of the size distribution
ψ	Particle sphericity
ω_0	Single scattering albedo

SUMMARY

The Arctic radiation climate is influenced substantially by anthropogenic and natural aerosols. There have been numerous studies devoted to understanding the radiative impacts of anthropogenic aerosols (e.g. those responsible for producing the Arctic haze phenomenon) and natural aerosols (e.g. dust and smoke) on the Arctic environment, but volcanic aerosols have received less attention. Volcanic eruptions occur frequently in the Arctic and have the capacity to be long duration, high intensity events, expelling large amounts of aerosol-sized ash and gases, which form aerosols once in the atmosphere. Additionally, volcanic eruptions deposit ash, which can alter the surface reflectivity, and remain to influence the radiation balance long after the eruptive plume has passed over and dissipated. The goal of this dissertation is to quantify the radiative effects of volcanic aerosols in the Arctic caused by volcanic plumes and deposits onto ice and snow covered surfaces.

The shortwave, longwave, and net direct aerosol radiative forcing efficiencies and atmospheric heating/cooling rates caused by volcanic aerosol from the 2009 eruption of Mt. Redoubt were determined by performing radiative transfer modeling constrained by NASA A-Train satellite data. The optical properties of volcanic aerosol were calculated by introducing a compositionally resolved microphysical model developed for both ash and sulfates. Two compositions of volcanic aerosol were considered in order to examine a fresh, ash rich plume and an older, ash poor plume. The results indicate that environmental conditions, such as surface albedo and solar zenith angle, can influence the sign and the magnitude of the radiative forcing at the top of the atmosphere and at the surface. Environmental conditions can also influence the magnitude of the forcing in the

aerosol layer. For instance, a fresh, thin plume with a high solar zenith angle over snow cools the surface and warms the top of the atmosphere, but the opposite effect is seen by the same layer over ocean. The layer over snow also warms more than the same plume over seawater. It was found that plume aging can alter the magnitude of the radiative forcing. For example, an aged plume over snow at a high solar zenith angle would warm the top of the atmosphere and layer by less than the fresh plume, while the aged plume cools the surface more. These results were compared with those reported for other aerosols typical to the Arctic environment (smoke from wildfires, Arctic haze, and dust) to demonstrate the importance of volcanic aerosols. It is found that the radiative impacts of volcanic aerosol plumes are comparable to those of other aerosol types, and those compositions rich in volcanic ash can have greater impacts than other aerosol types.

Volcanic ash deposited onto ice and snow in the Arctic has the potential to perturb the regional radiation balance by altering the surface reflectivity. The areal extent and loading of ash deposits from the 2009 eruption of Mt. Redoubt were assessed using an Eulerian volcanic ash transport and dispersion model, Fall3D, combined with satellite and deposit observations. Because observations are often limited in remote Arctic regions, we devised a novel method for modeling ash deposit loading fields for the entire eruption based on best-fit parameters of a well-studied eruptive event. The model results were validated against NASA A-train satellite data and field measurements reported by the Alaska Volcano Observatory. Overall, good to moderate agreement was found. A total cumulative deposit area of 3.7×10^6 km^2 was produced, and loadings ranged from ~7000 ± 3000 gm^{-2} near the vent to <0.1 ± 0.002 gm^{-2} on the outskirts of the deposits. Ash loading histories for total deposits showed that fallout ranged from ~5 – 17 hours.

The deposit loading results suggest that ash from short duration events can produce regionally significant deposits hundreds of kilometers from the volcano, with the potential of significantly modifying albedo over wide regions of ice and snow covered terrain.

The solar broadband albedo change, surface radiative forcing, and snowmelt rates associated with the ash deposited from the 2009 eruption of Mt. Redoubt were calculated using the loadings from Fall3D and the snow, ice, and aerosol radiative models. The optical properties of ash were calculated from Mie theory, based on size information recovered from the Fall3D model. Two sizes of snow were used in order to simulate a young and old snowpack. Deposited ash sizes agree well with field measurements. Only aerosol-sized ashes in deposits were considered for radiative modeling, because larger particles are minor in abundance and confined to areas very close to the vent. The results show concentrations of ash in snow range from ~ 6.9×10^4 – 1×10^8 ppb, with higher values closer to the vent and lowest at the edge of the deposits, and integrated solar albedo reductions of ~ 0 – 59% for new snow and ~ 0 – 85% for old snow. These albedo reductions are much larger than those typical for black carbon, but on the same order of magnitude as those reported for volcanic deposits in Antarctica. The daily mean surface shortwave forcings associated with ash deposits on snow ranged from 0 – 96 Wm^{-2} from the outmost deposits to the vent. There were no significantly accelerated snowmelts calculated for the outskirts of the deposits. However, for areas of higher ash loadings/concentrations, daily melt rates are significantly higher (~ 220 – 320%) because of volcanic ash deposits.

CHAPTER 1

INTRODUCTION

1.1 Background and motivation

An important modulator of Arctic radiation climate is the presence of aerosols [*Shindell*, 2007], both natural [*Myhre et al.*, 2007; *Stone et al*., 2007, 2008] and anthropogenic [*Ritter et al*., 2005; *Quinn et al*., 2007, 2008]. Aerosols are solid or liquid particles with diameters ranging from a few nanometers up to 100 micrometers, which interact with electromagnetic radiation. The radiative impacts aerosols on the Arctic environment are strongly controlled by the seasonality of many related factors, such as the amount of incoming solar radiation, surface albedo, precipitation, and transport of pollutants [*Quinn et al.*, 2008; *Sokolik et al*., 2011]. In the Arctic, the surface reflectivity and sun angle can vary widely depending on time of year and can change the magnitude, and even the sign, of the radiative effects [*Stone et al*., 2008]. An absorbing aerosol such as black carbon over a highly reflective surface tends to reduce the amount of solar energy reaching the surface, while leading to warming in the aerosol layer [*Stone et al*., 2008; *Shaw and Stamnes*, 1980]. Given the high surface albedos common during Arctic springtime, even aerosols with a moderate absorbing capability can have this effect [*Quinn et al*., 2008].

There is a large increase in tropospheric aerosols in the Arctic in late winter and early spring each year, which leads to the creation of Arctic haze [*Quinn et al*., 2008]. These haze-producing aerosols are associated with pollution and are largely transported from Europe and Asia. The composition of the pollution aerosol includes sulfate and nitrate, organic carbon, and

soot [*Klonecki et al*., 2003; *Stohl*, 2006; *Quinn et al*., 2008]. *Quinn et al*. [2008] identified ways in which Arctic warming due to the anthropogenic haze might be reduced. However, the effects of natural aerosols, such as smoke, dust, and volcanic aerosol, were not considered by *Quinn et al*. [2008]. There is a strong need to understand the role natural aerosols play in modulating Arctic climate. The radiative impacts of smoke [*Stone et al.*, 2008] and dust [*Stone et al.*, 2007] have been considered. However, volcanic aerosols continue to be largely overlooked in the Arctic environment. Volcanic aerosols may be expected to have a particularly strong influence on the regional Arctic climate because of the high sensitivity of the Arctic environment to radiative perturbations, as indicated by numerous studies focusing on the aforementioned other aerosol types (haze, smoke, and dust).

Volcanic eruptions frequently disrupt air travel routes and reduce air quality in populated areas. Flying through even diffuse volcanic plumes have caused in flight emergencies and millions of dollars of damage to aircraft. Volcanic ash can also be harmful to the eyes and lungs. Because of the potential dangers of volcanic aerosols to public health and aviation, the radiative effects of volcanic aerosols have received less attention and are poorly understood [*Intergovernmental Panel on Climate Change*, 2007].

Volcanic eruptions are capable of producing a huge, sporadic aerosol signal, lasting anywhere from minutes to years [*Simkin and Siebert*, 1994]. Volcanic aerosols from high northern latitude eruptions can cover large areas, as in the recent eruption of Eyjafjallajökull in Iceland, which disrupted air travel across Europe. According to the Alaska Volcano Observatory (AVO), Alaskan volcanoes alone have had an average eruption frequency of two per year over the past 40 years. Depending on the time of year, volcanic aerosol may be present along with other aerosol types. Following an eruption in Arctic springtime, dust, haze and volcanic aerosol

may all be present. For eruptions in boreal summer, wildfire smoke will be present along with volcanic aerosols. In boreal winter, aerosols from a volcanic eruption will be accompanied by haze. Despite the high frequencies and intensities of volcanic eruptions, volcanic aerosols in the Arctic are relatively neglected in assessments of Arctic aerosol.

In general, volcanic aerosols are composed of ash and sulfates coated with sulfates, water and/or ice [*Rose et al*., 2004; *Prata et al*., 2007; *Textor et al*., 2006; *Pueschel et al*., 1994]. Ash and sulfates are considered the dominant aerosol components of most eruptive plumes [e.g., *Andersson et al*., 2012]. In volcanic eruptions, sulfates are formed from a reaction between emitted volcanic sulfur dioxide (SO_2) and water. Sulfates may persist in the stratosphere for up to three years [*Clarisse et al*., 2008], causing the stratosphere to warm and the surface to cool [*Robock*, 2000]. Ash is formed through fragmentation processes within the volcanic conduit and expelled into the atmosphere during an eruption. Ash can vary greatly in shape, ranging from spherical particles to particles with nonsphericities as low as 0.4 [*Bonadonna et al*., 2012; *Alfano et al*., 2011]. The lifetime of fine ash in the stratosphere is on the order of a few weeks [*Neimeier et al*., 2009]. It is for this reason sulfates are the principal aerosol commonly used to predict the global climate perturbation expected from a given eruption [*Stenchikov et al*., 1998; *Ramachandran et al*., 2000]. However on regional scales, both volcanic ash and sulfate aerosols in the troposphere become important. In this case, sulfates and ash have similar residence times, on the order of days to weeks [*Seinfeld and Pandis*, 2006]. Therefore, ash must be considered along with sulfate in estimating the regional radiative impact of volcanic aerosol.

Volcanic aerosols can reflect and absorb shortwave (SW) radiation, and they scatter, absorb, and emit radiation in the longwave (LW) part of the spectrum. The interaction of volcanic aerosols with electromagnetic radiation can cause warming or cooling of the surface

and atmosphere, depending on the reflectivity of the underlying surface, the solar zenith angle (SZA), the optical properties of the aerosol layer, the vertical structure of temperature and humidity, and cloud characteristics. Ash deposits may lower the albedo of ice and snow covered surfaces, which would be expected to perturb the Arctic's radiation budget and cause early snowmelt, analogously to soot deposits [*Flanner et al.*, 2007] and dust deposits [*Painter et al.*, 2010]. To our knowledge, there have been no assessments of radiative impacts due to volcanic ash deposits in the Arctic [*Young et al*., 2014]. Additionally, ash [*Textor et al.*, 2006; *Lathem et al.*, 2011] and sulfates [*Boucher and Lohmann*, 1995; *Liu and Penner*, 2002] can serve as cloud condensation nuclei and ice nuclei. Thus, volcanic aerosols may have an indirect radiative effect by altering the optical properties of clouds [*Lohmann et al*., 2003, *Sokolik et al*., 2011]. Ash deposited into ocean waters may be a source of limiting nutrients, such as iron, and cause increases in marine productivity [*Langmann et al.*, 2010]. Volcanic aerosols increase the amount of diffuse radiation at the surface, which will increase the efficiency of photosynthesis [*Gu et al*., 2003]. Such changes in the marine and terrestrial biosphere may be expected to effect the CO_2 cycle. Figure 1.1 illustrates the broad impacts volcanic aerosols can have on the Arctic environment.

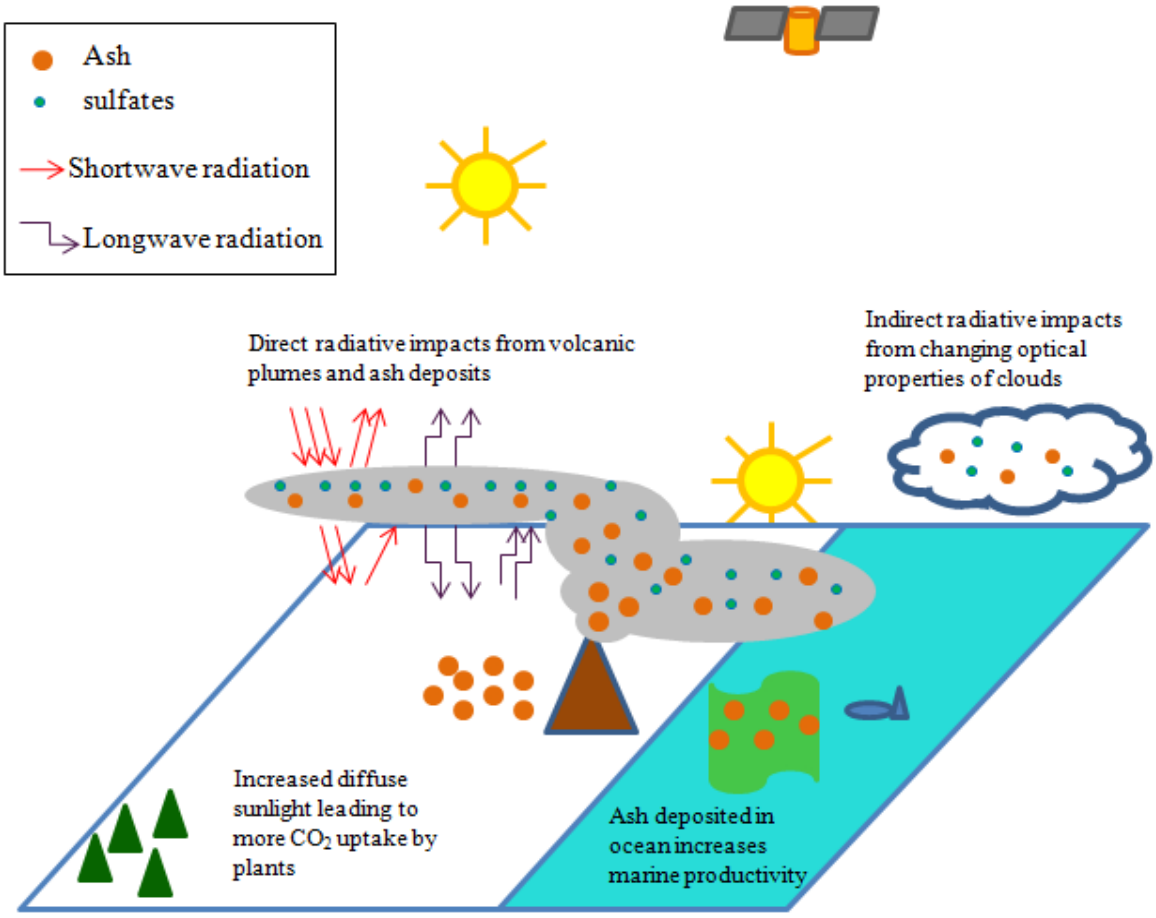

Figure 1.1: Broad impacts of volcanic aerosols on the Arctic environment

Volcanoes in the Arctic have been the source of many climatically important eruptions in the last several centuries. The June 1783 eruption of Laki, a volcanic fissure in Iceland, caused a drop in global temperatures [*Thordarson and Self*, 2003], drought and famine [*Frogner et al.*, 2006]. The June 1912 Novaerupta-Katmai eruption near Kodiak, Alaska, was the most powerful eruption of the 20th century [*Hildreth and Fierstein*, 2012]. Surface cooling was reported widely in the Northern Hemisphere throughout the summers of 1912 and 1913, with a maximum cooling of –0.9ºC for September 1912 [*Hildreth and Fierstein*, 2012; *Kimball*, 1913; *Humphreys*, 1913; *Griggs*, 1922].

Recent volcanic eruptions in the region include: Redoubt (Alaska, USA) in March-April 2009, Sarychev (Russia) in June 2009, Shiveluch (Russia) in September 2009, and

Eyjafjallajökull (Iceland) in April-May 2010. During October 2013, there were ~4 volcanoes currently erupting and ~10 volcanoes experiencing unrest above 55^{o}N (www.volcanodiscovery.com). Recent and ongoing eruptions in the Arctic have fortunately been small to medium – sized events. Although small to mid-sized volcanic eruptions are less extreme events, they occur more frequently and provide a more regular stream of ash and gases to the environment than larger eruptions. *Neely et al.* [2013] found that sulfates from small to mid-sized volcanic eruptions have helped to counteract 25% of the warming from anthropogenic sources predicted over Asia from 2000 to 2010.

The impact of volcanic aerosols on the Arctic climate is difficult to assess because of their complex nature and limited measurements of physical and chemical properties. Determining optical properties for radiative transfer calculations requires information on aerosol composition, size distributions, mixing state, shapes, and types of aerosol present. Composition must be known in order to determine the spectral refractive index. Particle counters on balloons and aircrafts have aided in measuring size distributions of stratospheric sulfuric acid aerosol [*Jager and Deshler*, 2002; *Deshler et al*., 1992, 1993, 2008; *Pueschel et al*., 1994]; however, these measurements have typically been made several weeks to months after the eruption, which does not help to determine the size distributions of "fresh" volcanic sulfate or ash. Therefore, in efforts to study the formation and aging process of volcanic sulfates, models have been developed to calculate how the size distribution evolves [*Stier et al*., 2005] and have been incorporated into general circulation models [*Niemeier et al*., 2009]. For volcanic ash, there have been few airborne measurements of size distribution, mainly due to the dangers involved in making this measurement. Although size distributions have been measured on ashfall samples [*Munoz et al*., 2004; *Martin et al*., 2009; *Riley et al*., 2003; *Scott and McGimsey*, 1994], these

values will not be representative of the actual size distribution during an eruption due to sorting which occurs during transport in the atmosphere [*Rose and Durant*, 2009]. As the volcanic plume ages, the radiative properties of the plume may be significantly altered by the changing size and composition of volcanic aerosols. Thus, it is important to examine how the aging of volcanic aerosol affects the radiative impact.

In addition to SZA, surface albedo, and optical properties of aerosol, there are more aerosol layer-specific characteristics that must be known for radiative calculations. For an aerosol plume, these are: aerosol optical depth (AOD), physical thickness, and vertical placement of the layer in the atmosphere. Sunphotometers and ground-based lidars can help determine AOD, and ground-based lidars can also be used to obtain thickness and vertical placement. However, the coverage of ground-based sensors is limited.

Similar information is needed to calculate the radiative impacts of ash deposited onto ice and snow. The model requires solar zenith angle (SZA) and underlying surface reflectance, snow layer properties (i.e., snow layer thickness, snow density for each layer, and snow effective radius), and impurity properties (i.e., particle mass mixing ratios, effective radius, and refractive index). In the case of calculating radiative impacts for ash deposits, information on ash deposit loadings and areal extents also must be ascertained. Ground measurements of ash loadings and areal extents are helpful but usually do not map out the entire extent of deposits or provide an adequate spatial resolution of samples.

Due to the limitations in ground-based sensors and field measurements, as well as the remote locations of Arctic volcanoes, satellite remote sensing is essential for monitoring aerosol from volcanic eruptions. The NASA afternoon satellite constellation A-Train provides a unique opportunity to examine eruptions and the evolution of volcanic plumes. The A-Train consists of

five polar orbiting satellites flying in close configuration, each equipped with sensors designed with varying capabilities, from passive to active sensors, measuring in wavelength ranges from the UV to radio. Combining the data retrieved from several sensors allows for an unprecedented view of volcanic eruptive plumes [*Carn et al*., 2009; *Thomas et al*., 2009].

The Moderate Resolution Imaging Spectroradiometer (MODIS) instrument flying aboard Aqua and Terra satellites, the Ozone Monitoring Instrument (OMI) on the Aura spacecraft, and the Cloud-Aerosol with Orthogonal Polarization (CALIOP) aboard the CALIPSO (Cloud-Aerosol Lidar and Infrared Pathfinder Satellite Observations) platform are sensors capable of detecting volcanic aerosols. These sensors are on polar orbiting satellites, which provide excellent coverage of the Arctic region, allowing for mapping out the spatial extent of volcanic plumes and deposits. The MODIS instrument provides true color images of ash plumes and deposits and aerosol optical depth (AOD) of volcanic plumes. The OMI sensor provides a UV aerosol index (AI), which can detect the presence of UV absorbing aerosols, such as ash, dust, and smoke. CALIPSO provides the vertical plume structure, which is useful in determining the placement of the plume in the atmosphere, the plume top height, and the plume thickness. However, in the Arctic, environmental conditions, such as meteorological clouds and high surface reflectivities, often hamper retrievals for passive instruments measuring in the visible and UV, such as MODIS and OMI, and space-based lidars, such as CALIPSO.

Transport models can aid in providing the quantitative characterization of volcanic aerosols and ash deposits. Past studies have used General Circulation Models (GCMs) to simulate the transport and deposition of volcanic ash [e.g., *Niemeier et al*., 2009]. However, the source conditions (i.e., distribution of ash in the eruptive column) of volcanic eruptions are not treated in GCMs, which handle volcanic eruptions by assigning a flux amount of material into

the atmosphere [*Kravitz et al*., 2011; *Robock et al*., 2009; *Robock et al*., 1995]. Neglecting the dynamics of the actual explosion will influence regional transport and deposition of ash. Recent development of a preprocessing tool has allowed for the computation of initial ash fields from source conditions for input into mesoscale atmospheric chemistry models, such as WRF-Chem [*Stuefer et al*., 2013]. Alternatively, volcanic ash transport and dispersion models (VATDMs) calculate initial ash fields directly from eruption source input parameters. In addition, VATDMs consider a full size spectrum of ash and can include nonspherical ash particles. Due to the dangers involved with measuring the size distributions of ash in plumes in situ, the size distributions used in VATDMs are measured from deposits in the field. These measurements are often depleted in fine ash (aerodynamic diameter < 2.5 μm) because fine particles can be swept to great distances from the volcano, where they cannot be collected and measured [*Rose and Chesner*, 1987].

1.2 Outline of Dissertation

The goal of this thesis is to perform a satellite and VATDM aided integrated analysis to quantify regional direct LW and SW radiative impacts due to volcanic aerosol from a mid-sized eruption in the Arctic, using the 2009 eruption of Mt. Redoubt in Alaska, USA as a case study. To accomplish this goal, we use satellite observations and the VATDM, Fall 3D model, considering a broad range of ash particle sizes. This model is an open source Eulerian ash dispersion and transport model, which is widely used by the ash forecasting community [e.g., *Folch et al*., 2009; *Costa et al*., 2006]. The research presented in this document contains:

(1) A range of LW and SW radiative impacts to be expected from eruptive plumes produced by mid-sized Arctic volcanoes.

(2) Areal extents, loadings and spatial temporal gradients of ash deposits loadings produced from the 2009 Mt. Redoubt eruption.

(3) The radiative impacts of ash deposits from the 2009 eruption of Mt. Redoubt.

In this thesis, the radiative impacts of plumes and ash deposits from a mid-sized Arctic eruption are calculated using the Santa Barbara Disort Atmosperhic Radiative Transfer (SBDART) model [Richiazzi et al., 1998] for plumes and the SNow, ICe, and Aerosol Radiation (SNICAR) model [e.g., *Flanner and Zender*, 2005, 2006*; Flanner et al*., 2007] for deposits. SBDART is a 1D radiative transfer model that solves the radiative transfer equation using the Discrete Ordinate Radiative Transfer (DISORT) method for a plane parallel atmosphere. Plume studies often neglect the LW radiative effects of aerosols in the Arctic, but unless these are for very small aerosols sizes, as in the case of wildfire smoke, the LW radiative effects are not negligible and should be considered along with the SW. In Arctic winter and polar nights, LW radiative effects will dominate. The SNICAR model uses a two-stream, delta-Eddington approximation, and a multi-layer solution from *Toon et al*. [1989], to solve the plane parallel radiative transfer equation for multiple layers in snow. In allowing for multiple layers, the model can address the vertical differences in snow and impurity properties. The remainder of this dissertation is outlined in Figure 1.2.

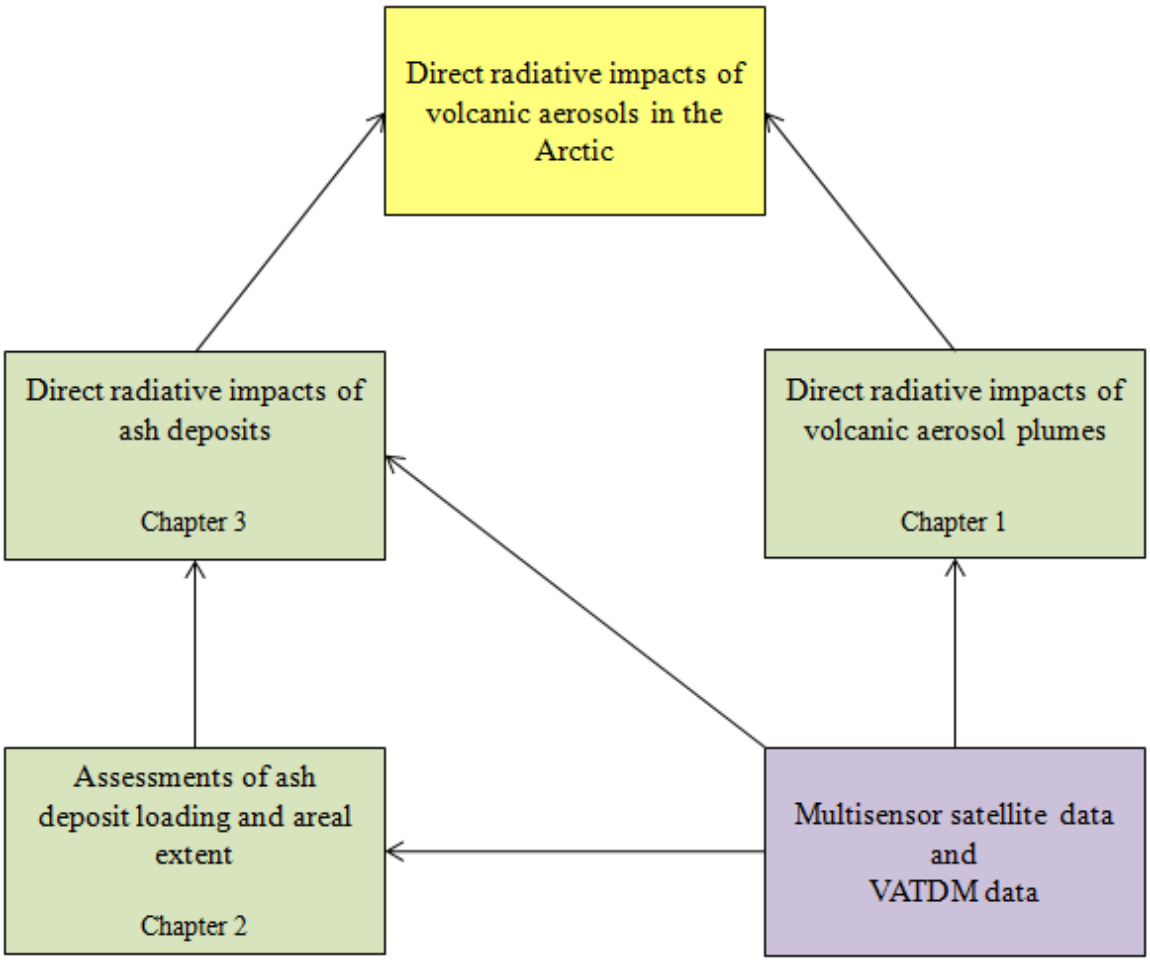

Figure 1.2: Layout and main goals of dissertation

Chapter 2 contains assessments of SW, LW, and net direct aerosol radiative forcing efficiencies and atmospheric heating/cooling rates caused by volcanic aerosol plumes from the 2009 eruption of Mt. Redoubt. The SBDART model is constrained by NASA A-Train satellite multisensor data. The optical properties of volcanic aerosol are calculated by introducing a compositionally resolved microphysical model developed for both ash and sulfates. Two compositions of volcanic aerosol are considered in order to examine a fresh, ash rich plume and an older, ash poor plume. Radiative impacts of volcanic aerosols are then compared to those of other aerosol types typical to the Arctic region (smoke, dust, and haze).

Chapter 3 characterizes loading fields of ash deposits from the 2009 eruption of Mt. Redoubt. In particular, this study investigates the loading fields and spatial/temporal loading gradients for each deposition event, as well as the spatial variability of uncertainties in model loading. The approach utilizes the capabilities of a VATDM (Fall3D) to track transport and deposition of ash, as well as obtain ash deposit loadings, AOD fields within plumes, and areal extents of deposits and plumes. The model data were validated against NASA A-train satellite data and field measurements reported by the AVO.

Chapter 4 utilizes deposit information from Chapter 3 to model radiative impacts due to volcanic ash deposits from the 2009 eruption of Mt. Redoubt. The study uses a Fall3D to investigate the size distributions of ash deposits for optical calculations of ash. Deposit information is used in the SNICAR model to calculate a range of surface albedo change and radiative forcing due to ash deposition that can be expected from a mid-sized volcanic eruption. The hydrological importance of this eruption is assessed through making estimates of snowmelt amounts. A comparison between the calculated surface albedo change and radiative forcing to other depositional events associated with different aerosol types is made. Lastly, Chapter 5 summarizes the main results of this dissertation and discusses this work into the broader context of the field. The areas in which further research is needed are then discussed.

CHAPTER 2

REGIONAL RADIATIVE IMPACT OF VOLCANIC AEROSOL FROM THE 2009 ERUPTION OF MT. REDOUBT

The work presented in this chapter is published in Atmospheric Chemistry and Physics [Young et al., 2012]

2.1 Introduction

Mt. Redoubt is a stratovolcano located in Alaska, USA. Rising to an elevation of 3108 m (10197 ft), Redoubt is the second tallest volcano in the Aleutian Range. Redoubt has been active five times since 1900, with the most recent eruptions occurring in 1989 and 2009. The last period of explosive eruptions began on March 23 2009 and lasted through April 4 2009. Eruptive plumes reached into the stratosphere on several occasions, reduced air quality and posed a threat to aviation [*Carlile and Nelson*, 2009; *Coombs and Schaefer*, personal communication, 2011]. However, little attention has been given to the regional radiative impact of volcanic aerosols. Here, we use the 2009 eruption of Redoubt as an opportunity to assess a range of the radiative impacts that may be expected from high northern latitude eruptions.

The primary mechanism by which volcanic eruptions alter the Earth's climate is through the formation of sulfate aerosols. Sulfates may persist in the stratosphere for up to three years [*Clarisse et al*., 2008], causing the stratosphere to warm and the surface to cool [*Robock*, 2000]. Ash expelled by volcanic eruptions can also interact with electromagnetic radiation, but the lifetime of fine ash in the stratosphere is only on the order of a few weeks [*Neimeier et al*., 2009]. It is for this reason sulfates are the principal aerosol commonly used

to predict the global climate perturbation expected from a given eruption [*Stenchikov et al*., 1998; *Ramachandran et al*., 2000]. However on regional scales, both volcanic ash and sulfate aerosols in the troposphere become important. In this case, sulfates and ash have similar residence times, on the order of days to weeks. Therefore, ash particles must be considered along with sulfate aerosol in estimating the regional radiative impact, as well as specific environmental conditions including surface albedo, solar zenith angle (SZA), regional weather, and other aerosol types present in the region.

Volcanic aerosols may be expected to have a particularly strong influence on the regional Arctic climate because of the high sensitivity of the Arctic environment to radiative perturbations, as indicated by numerous studies focusing on other aerosol types, both natural [*Myhre et al*., 2007; *Stone et al*., 2007, 2008] and anthropogenic [*Ritter et al*., 2005; *Quinn et al*., 2007, 2008]. The resulting forcing aerosols will have on the Arctic environment is strongly controlled by the seasonality of many related factors, such as the amount of incoming solar radiation, surface albedo, precipitation, and transport of pollutants [*Quinn et al*., 2008; *Sokolik et al*., 2011]. There is a large increase in tropospheric aerosols in the Arctic in late winter and early spring each year, which leads to the creation of Arctic haze [*Quinn et al*., 2008]. The haze-producing emissions are largely from Europe and Asia and consist of sulfate and nitrate aerosols, organic carbon, and soot [*Klonecki et al*., 2003; *Stohl*, 2006; *Quinn et al*., 2008]. The importance of surface albedo has been investigated, and in general, an absorbing aerosol (i.e., smoke) over a highly reflective surface tends to reduce the amount of solar energy reaching the surface, while leading to warming in the aerosol layer [*Stone et al*., 2008; *Shaw and Stamnes*, 1980]. Given the high surface albedos common during Arctic springtime, even aerosols with a moderate absorbing capability can have this effect [*Quinn et al*., 2008].

However, the effects of natural aerosols, such as volcanic aerosol, were not considered by *Quinn et al*. [2008] in making recommendations to mitigate Arctic warming due to anthropogenic aerosols.

The impact of volcanic aerosols on the Arctic climate is difficult to assess because of their complex nature and limited measurements of physical and chemical properties. Additional complexity comes from seasonal variations that dramatically alter the amount of incoming solar radiation and surface reflectivity. Additionally, volcanic aerosol may have an indirect effect on clouds [*Lohmann et al*., 2003, *Sokolik et al*., 2011]. It is also possible that ash deposits may lower the albedo of ice and snow covered surfaces, which would be expected to perturb the Arctic's radiation budget just as soot deposits [*Flanner et al*., 2007] and dust deposits [*Painter et al*., 2010] have been shown to do.

Performing optical and radiative transfer calculations requires information on aerosol composition, size distributions, and types of aerosol present. Composition must be known in order to determine the spectral refractive index. Satellite data has been employed to determine size distributions of sulfates after eruptions [*Stenchikov et al*., 1998; *Ramachandran et al*., 2000]. Particle counter measurements on balloons and aircraft have aided in calculating size distributions of stratospheric sulfuric acid aerosol [*Jager and Deshler*, 2002; *Deshler et al*., 1992, 1993; *Deshler*, 2008; *Pueschel et al*., 1994]; however, these measurements have typically been made several weeks to months after the eruption, which does not help to determine the size distributions of "fresh" volcanic sulfate or ash. Therefore, in efforts to study the formation and aging process of volcanic sulfates, models have been developed to calculate how the size distribution evolves [*Stier et al*., 2005] and have been incorporated into general circulation models [*Niemeier et al*., 2009]. For volcanic ash, there have been few

airborne measurements of size distribution, mainly due to the dangers involved in making this measurement. Although size distributions have been measured on ashfall samples [*Munoz et al*., 2004; *Martin et al*., 2009; *Riley et al*., 2003; *Scott and McGimsey*, 1994], these values will not be representative of the actual size distribution during an eruption due to sorting which occurs during transport in the atmosphere [*Rose and Durant*, 2009]. As the volcanic plume ages, the radiative properties of the plume are significantly altered by the changing size and composition of volcanic aerosols. Thus, it is important to examine how the aging of volcanic aerosol affects the radiative impact.

The goal of this study is to assess the range of regional radiative impact of volcanic aerosol from the 2009 eruption of Mt. Redoubt using satellite data and a radiative transfer model. We examine both the longwave (LW) and shortwave (SW) components of the direct radiative forcing at the top of the atmosphere (TOA) and at the surface, and SW and LW atmospheric heating/cooling rates. This work employs a satellite multiple sensor approach to constrain the transport, areal and vertical extent, and characteristics of volcanic plumes. The organization of the paper is as follows. Section 2 presents the data used in this study and introduces a methodology to create a compositionally resolved microphysical model for volcanic aerosols. The size distributions and refractive indices selected for optical calculations are discussed, as well as the satellite data products utilized in the radiative transfer model. Section 3 discusses results of direct aerosol radiative forcing efficiencies (DARFEs) and atmospheric heating/cooling rate profiles in terms of sensitivity to plume-specific and environmental input parameters for the Arctic region. Section 4 summarizes the important findings of this study and makes recommendations for future research.

2.2 Data and methodology

Our approach uses satellite data in conjunction with the HYbrid Single-Particle Lagrangian Integrated Trajectory (HYSPLIT) transport model for volcanic ash to constrain a radiative transfer model. The HYSPLIT computes the dispersion and transport of an evenly distributed vertical column of ash with a given size distribution placed directly over the volcano summit [*Draxler and Rolph*, 2011; *Rolph*, 2011]. The following parameters are needed to run the model: volcano latitude and longitude, volcano summit height, eruption date and time, eruption duration, and ash column height. In this study the HYSPLIT model was run for selected eruptions in order to provide supporting evidence that the aerosol plumes detected by satellites are indeed volcanic in origin.

2.2.1 Satellite data

The NASA A-Train satellite constellation provides the unique capability of passive and active collocated satellite sensors to study volcanic eruptions [*Carn et al*., 2009; *Thomas et al*., 2009]. The CALIOP lidar flies aboard the CALIPSO (Cloud-Aerosol Lidar and Infrared Pathfinder Satellite Observations) platform and measures backscatter at 532 and 1064 nm. Past studies have successfully employed CALIPSO to investigate the vertical structure of volcanic plumes [*Thomason and Pitts*, 2008; *Yuan et al*., 2011]. Vertical profiles are useful in determining the position of the plume within the atmosphere, as well as plume top heights and thicknesses. Vertical profiles of aerosol were obtained from CALIPSO version 3.01 data. The sensors OMI and MODIS have greater spatial coverage and were used both to identify and track the plumes and to validate some of the products retrieved from CALIPSO.

The OMI instrument on the Aura spacecraft has an ultraviolet – visible spectral range of 0.27-0.50 μm and provides the UV aerosol index (AI) [*Torres et al*., 2007]. The AI is a

semi-quantitative indicator of the presence of UV-absorbing aerosols, such as volcanic ash, smoke, and dust. It is important to note that sulfate aerosols do not absorb UV radiation and will have negative values of AI, in contrast to UV-absorbing aerosols which have positive AI values.

The MODIS sensor flies on both the Terra and Aqua satellites. In this study, we employed true color MODIS images, aerosol optical depth (AOD) at 550 nm, and aerosol fine mode fraction products. The MODIS level 3 Collection 5 AODs were used to constrain the areal extent of volcanic plumes and determine a range of AODs for calculation of the radiative forcing. Fine mode fraction is the ratio of small mode optical depth to the total AOD [*Remer et al*., 2005]. We used MODIS level 2 Collection 5 fine mode fraction to determine approximate proportions of fine and coarse particles present in a plume.

2.2.2 Aerosol microphysical model

The optical properties of volcanic aerosol were determined through the development of a compositionally resolved microphysical model. In general, volcanic aerosols may be composed of ash, sulfates, hydrometeors, and ash particles coated with sulfates, water, and/or ice [*Rose et al*., 2004; *Prata et al*., 2007; *Textor et al*., 2006; *Pueschel et al*., 1994]. Here, we considered only ash and sulfate, both of which have distinct size distributions and spectral refractive indices. We incorporated representative size distributions and refractive indices for ash and sulfate using data reported in the literature, as well as a range of realistic ratios of fine to coarse modes and ash to sulfate deduced from satellite data [*Kearney and Watson* 2009; *Niemeier et al*., 2009; *Pollack et al*., 1973; *Spinetti et al*., 2008; *Stenchikov et al*., 1998]. A summary of the considered cases is presented in Table 2.1.

Table 2.1: Input parameters for SBDART. Sulfate size distribution was held constant at an effective radius of 0.5 μm and σ of 0.5 [*Kearney and Watson*, 2009]. For ash, σ is set to 0.59 and held constant for all simulations [*Niemeier et al*., 2009]. Refractive indices for sulfate from OPAC were used for 70% sulfate solution. For ash, refractive indices of andesite from *Pollack et al*. [1973] were used. [a] indicates values used for the April 2 case study. [b] indicates values used in sensitivity study. For both plumes, aerosol optical depth was distributed uniformly within the layer.

Model Parameter	Input	Source of input
Vertical placement and physical thickness of the aerosol layer	2.5 to 7 km [a] 3 to 20 km [b]	CALIPSO [a] AVO estimate based on radar [b]
Aerosol Optical Depth	0.18, 0.38, 0.58 [a] 1, 2, 3 [b]	MODIS [a,b]
Surface albedo	Seawater (0.041 at 550 nm) Snow (0.973 at 550 nm)	SBDART
Solar zenith angle	55° – 75°	Realistic sun angles
Range of ash to sulfate ratio	9:1 to 1:9	MODIS fine mode fraction
R_{eff} of ash	1.5 – 5 μm	Spinetti et al., 2008

We used lognormal particle size distributions for both ash and sulfate in the following form [*Kearney and Watson*, 2009]:

$$n_c(r) = \frac{1}{\sqrt{2\pi\sigma}} e^{-\frac{(\ln(r)-\mu)^2}{2\sigma^2}} \quad (2.1)$$

where n_c is the particle number concentration, r is the particle radius, and σ is the variance of the size distribution, or the log of the standard deviation:

$$\mu = (\ln R_{eff}) - 2.5\sigma^2 , \quad (2.2)$$

where R_{eff} is the effective radius.

We assume that sulfate occurs only in the fine mode, but ash can exist in both coarse and fine modes. To simulate fresh sulfate aerosol in a young volcanic plume, an effective radius of 0.5 μm and σ of 0.5 were used [*Kearney and Watson* 2009]. The size distribution of sulfate was held constant in order to study the effects of ash fallout. For ash, σ was set to 0.59 and held constant for all simulations, as in *Niemeier et al*. [2009]. Effective radius for ash was

allowed to vary from 5 μm to 1.5 μm, according to satellite retrievals of effective radii of ash in an aging plume reported by *Spinetti et al*. [2008]. It should be noted that these previous studies do not include a truly "fine" ash portion (aerodynamic diameter < 2.5 μm), and therefore we only considered ash in the coarse mode.

Refractive indices for both SW (0.3 – 4 μm) and LW (4 – 20 μm) spectral regions for ash and sulfate were taken from the literature. The Optical Properties of Aerosols and Clouds (OPAC) data were used for 70% sulfuric acid solution [*Hess et al*., 1998] to represent sulfate aerosol. For ash, refractive indices of andesite from *Pollack et al*. [1973] were used. Sulfuric acid solutions around 70% are commonly chosen for radiative transfer modeling of volcanic aerosol and are valid for most situations [e.g., *Stenchikov et al*., 1998]. However, measurements of temperature and relative humidity in the Arctic suggest that the sulfuric acid solution can be as low as 40-50% [*Yue et al*., 1994; *Russell et al*., 1996; *Lambert et al*., 1997]. These measurements are based on temperature and relative humidity of ambient Arctic air. Temperatures and relative humidities in a fresh volcanic plume are much higher, as magmatic volatiles in arc volcanoes are water rich [*Williams and McNutt*, 2005]. Therefore, we felt the 70% sulfuric acid solution was more realistic for a fresh volcanic plume than the lower values occurring in Arctic environments.

Ratios of fine and coarse mode aerosols were constrained with MODIS fine mode fraction retrievals. For the purposes of our study, the fine mode fraction represents the particle number proportion of sulfate present in an externally mixed aerosol mixture containing ash and sulfate. In order to realistically bracket the range of radiative forcing associated with ash fallout as a plume ages, an ash rich mixture (containing smaller fractions of sulfate and larger proportions of ash) was used as a proxy for a fresh plume, and a sulfate rich mixture

(consisting of higher proportions of sulfate and a smaller ash fraction) was chosen to simulate a more evolved, aged plume.

2.2.3 Radiation transfer calculations

The 1D radiative transfer model used in this study is a modified version of the Santa Barbara Disort Atmospheric Radiative Transfer (SBDART) model. SBDART solves the radiative transfer equation using the Discrete Ordinate Radiative Transfer (DISORT) method for a plane parallel atmosphere [*Ricchiazzi et al*., 1998]. The online version of SBDART is available at http://paulschou.com/tools/sbdart/. The model takes into account gaseous absorption and absorption and multiple scattering by aerosols. The model was modified to incorporate a user defined aerosol layer and the aerosol optical characteristics computed in this study. A spectral resolution of 5 nm for the SW and 20 cm^{-1} for the LW was used in modeling the upward and downward radiative fluxes. The subarctic winter standard atmospheric model [*McClatchey et al*., 1972] was used in radiative transfer calculations over seawater and snow surfaces with solar zenith angle (SZA) ranging from 55° to 75°. The spectral surface albedo for water and snow are from *Viollier* [1980] and *Wiscombe and Warren* [1980], respectively.

Net fluxes for both the SW and LW components at the top-of-the-atmosphere (TOA) and at the surface were computed by subtracting the upward flux from the downward flux:

$$F_{net} = F_{down} - F_{up} \quad (2.3)$$

The total net flux at TOA and at the surface were then calculated by adding the respective SW and LW net fluxes

$$F_{net\ total} = F_{net,\ SW} + F_{net,\ LW} \quad (2.4)$$

Atmospheric heating rates in units of K day^{-1} were calculated as follows:

$$dT / dt = - (1 / c_p \rho) (dF_{net} / dz) , \quad (2.5)$$

where c_p is the specific heat at constant pressure ($c_p = 1004.67$ J kg $^{-1}$ K $^{-1}$), and ρ is the air density of the aerosol layer. The change in net flux with respect to altitude is represented by dF_{net} / dz. We also computed and analyzed the direct aerosol radiative forcing, DARF, and direct aerosol radiative forcing efficiency, DARFE. The latter is defined as the change in the net flux with respect to the change in AOD (550 nm):

$$DARFE = \Delta F_{net} / \Delta AOD(550 \text{ nm}) \quad (2.6)$$

To calculate DARFE for an aerosol layer, the surface DARFE was subtracted from the DARFE at TOA:

$$DARFE_{atm} = DARFE_{TOA} - DARFE_{surface} \quad (2.7)$$

For each study case, we computed $DARFE_{TOA}$, $DARFE_{surface}$, and $DARFE_{atm}$ for SW, LW, and net forcing. The units of DARF are Wm^{-2} and DARFE are $Wm^{-2}AOD^{-1}$. The definition of DARFE used in our study is similar to that of *Stone et al*. [2008] to facilitate the comparison with results for other aerosol types.

2.3 Results and Discussion

2.3.1 Optical properties of volcanic aerosol

Based on satellite data analyses (see section 2.3.2), two externally mixed aerosol mixtures with varying proportions of ash and sulfate were selected to simulate plume aging. The refractive indices for sulfate and andesite are shown in Fig. 2.1a.

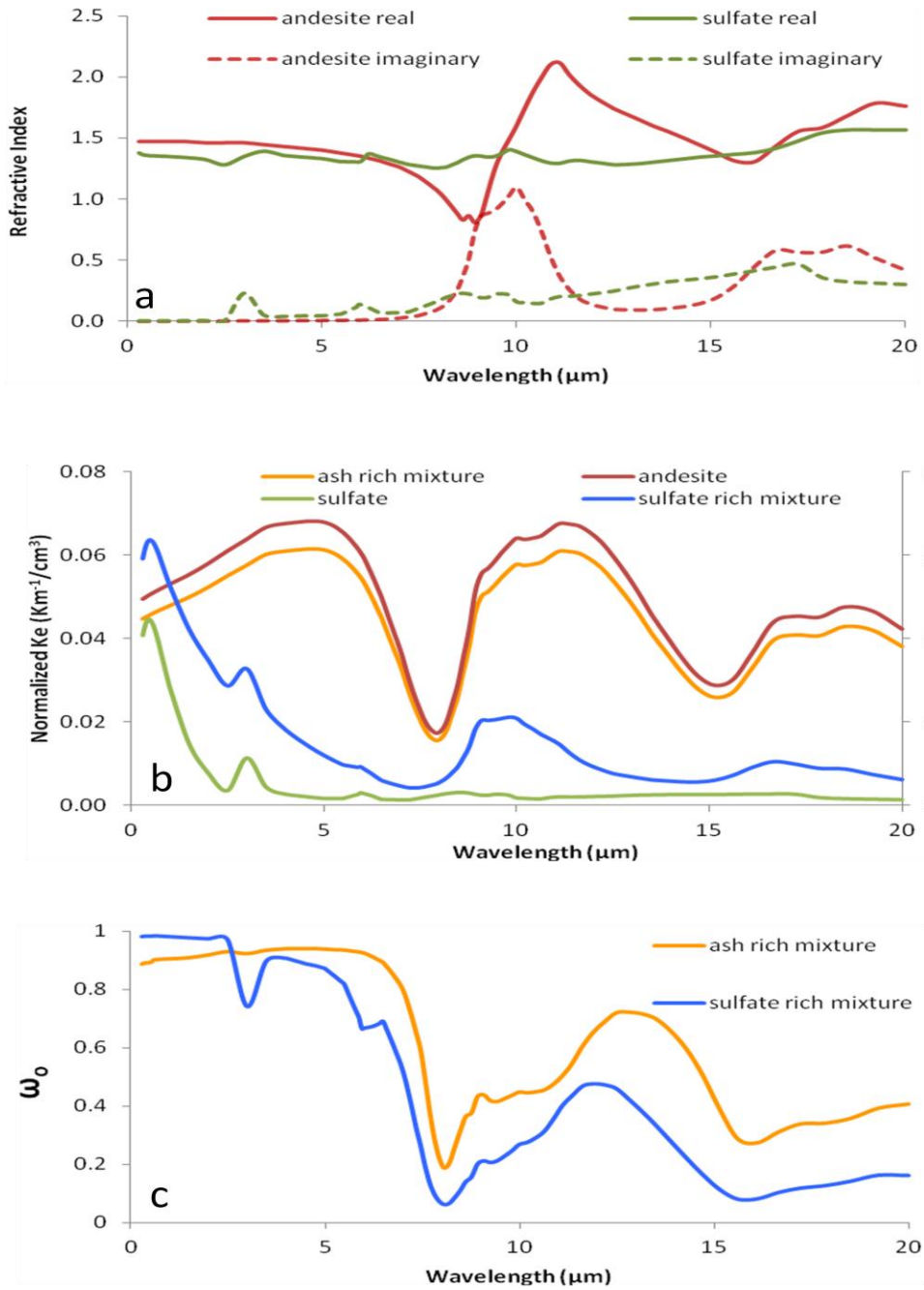

Figure 2.1: (a) Spectral dependence of refractive indices of ash and sulfate. (b) Concentration normalized extinction coefficients (K_e) versus wavelength for an ash rich mixture containing an ash to sulfate ratio of 9 to 1 and an effective radius for ash R_{eff} =5 µm compared to andesite with R_{eff} =5 µm (right axis) and for a sulfate rich mixture containing an ash to sulfate ratio of 1 to 9 and an effective radius for ash R_{eff} =1.5 µm compared to sulfate with R_{eff} =0.5 µm (left axis). (c) Single scattering albedo (ω_0) versus wavelength for an ash rich mixture containing an ash to sulfate ratio of 9 to 1 and R_{eff} =5 µm and a sulfate rich mixture containing an ash to sulfate ratio of 1 to 9 and R_{eff} =1.5 µm.

The normalized extinction coefficients, K_e, for the two aerosol mixtures and their sulfate and andesite constituents are shown in Fig. 2.1b as a function of wavelength. The normalized extinction coefficient is a measure of scattered and absorbed radiation by particles per unit concentration. Andesite absorbs and scatters both SW and LW radiation. The ash rich mixture is dominated by andesite ash. Sulfate scatters SW radiation and absorbs LW radiation, with negligible scattering in the LW because of small particle size. It is clear from Fig. 2.1b that the ash rich mixture resembles that of pure andesite, and the sulfate rich mixture more closely resembles that of sulfate. It is also apparent from Fig. 2.1b that the extinction coefficient per unit concentration is larger for both pure andesite and the ash dominated mixture at all wavelengths.

Figure 2.1c shows the single scattering albedo, ω_0, for both aerosol compositions. The single scattering albedo is the fraction of photons that would be scattered by aerosols. In the SW, the ash rich mixture absorbs light more effectively than the sulfate rich one until about 2.5 μm. At longer wavelengths, the ash rich mixture scatters radiation better than the sulfate dominated composition.

2.3.2 Satellite data analysis to constrain a radiative transfer model

The study cases presented here were selected by performing an integrated analysis of satellite data for the entire period of explosive volcano activity between March 22 and April 4. For each day in this time frame, CALIPSO overpasses were analyzed for a boxed region located 43^oN to 69^oN and 130^oW to 160^oW. A large collection region was needed to obtain a sufficient amount of data, because of CALIPSO's narrow swath. Therefore, it was expected if CALIPSO were to detect a plume, it would be after transport had carried it some distance from the source. Only data that showed clear detection of an aerosol plume with well-

developed vertical structure in CALIPSO's vertical cloud feature mask were selected. Aerosol index and SO_2 measurements from OMI and AOD from MODIS were then used to determine the likely source region of the detected aerosol plume and to provide evidence that it was volcanic in origin.

The 1724 UTC eruption on March 26 and the 1358 and 1416 UTC eruptions on April 4 were among the most violent eruptions, spewing ash well into the stratosphere [*Carlile and Nelson*, 2009; *Coombs and Schaefer*, 2011]. MODIS (Fig. 2.2) and OMI AI (Fig. 2.3) help confirm the presence of ash in these plumes, as well as provide insight into the overall transport of aerosol.

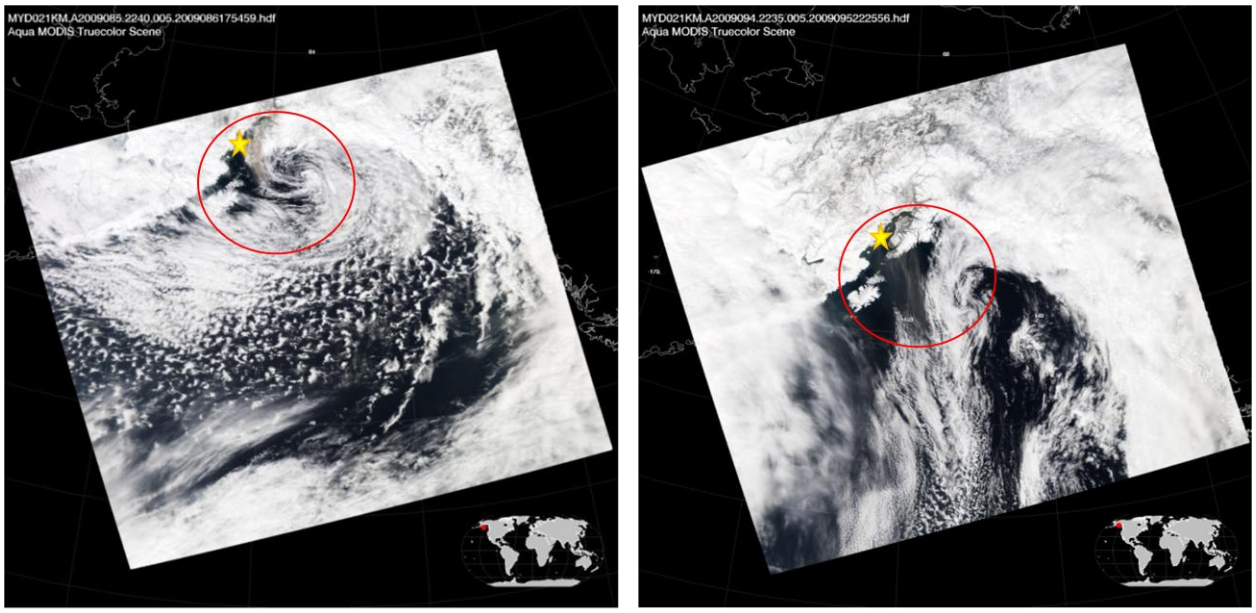

Figure 2.2: Aqua MODIS true color images on (a) March 26 at 22:40 UTC and (b) April 2 at 22:35 UTC. The aerosol plume is circled in red. The location of Mt. Redoubt is marked by a star.

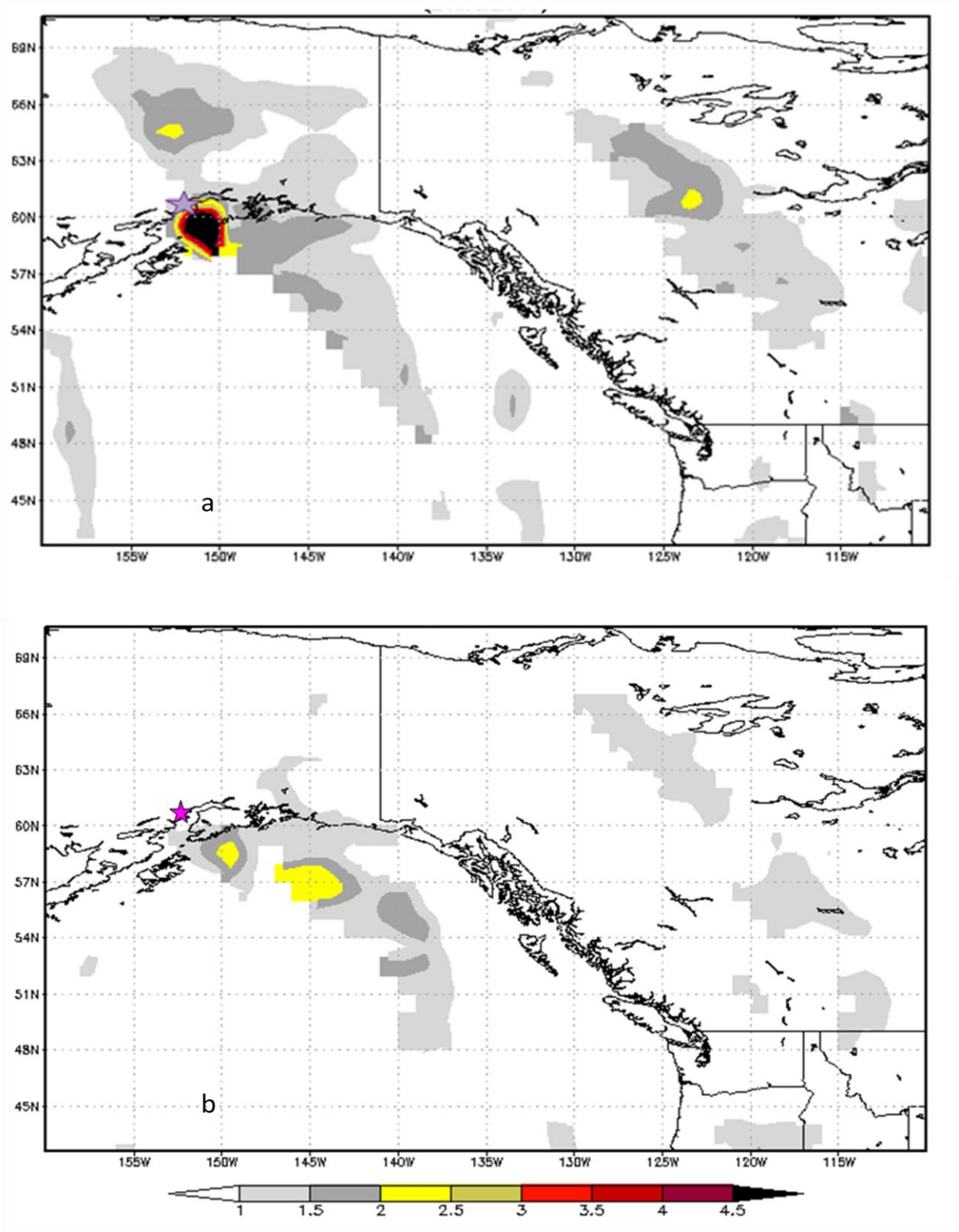

Figure 2.3: OMI AI for (a) March 26 and (b) April 4. The location of Mt. Redoubt is marked by a star.

The plume detected on April 4 (Fig. 2.2b and 2.3b) appears to be moving southeast of the volcano, over the Gulf of Alaska. However, the plume from March 26 (Fig. 2.2a and 2.3a) appears to be transporting ash both north of the volcano over Alaska, and southeast of the volcano. The transport of plumes on March 26 and April 4 over both seawater and snow surfaces illustrates the need for assessing the radiative forcing for different surface albedos.

However, CALIPSO data on March 26 and April 4 is not available due to the extensive cloud cover present during much of March and early April. After examining satellite data for the entire span of the explosive eruptions within the domain chosen, it was determined that the best data available were obtained for a plume detected on April 2. The aerosol profiles from CALIPSO reveal that the plume is completely contained in the troposphere and extends from ~ 2.5 – 7 km (Fig. 2.4a).

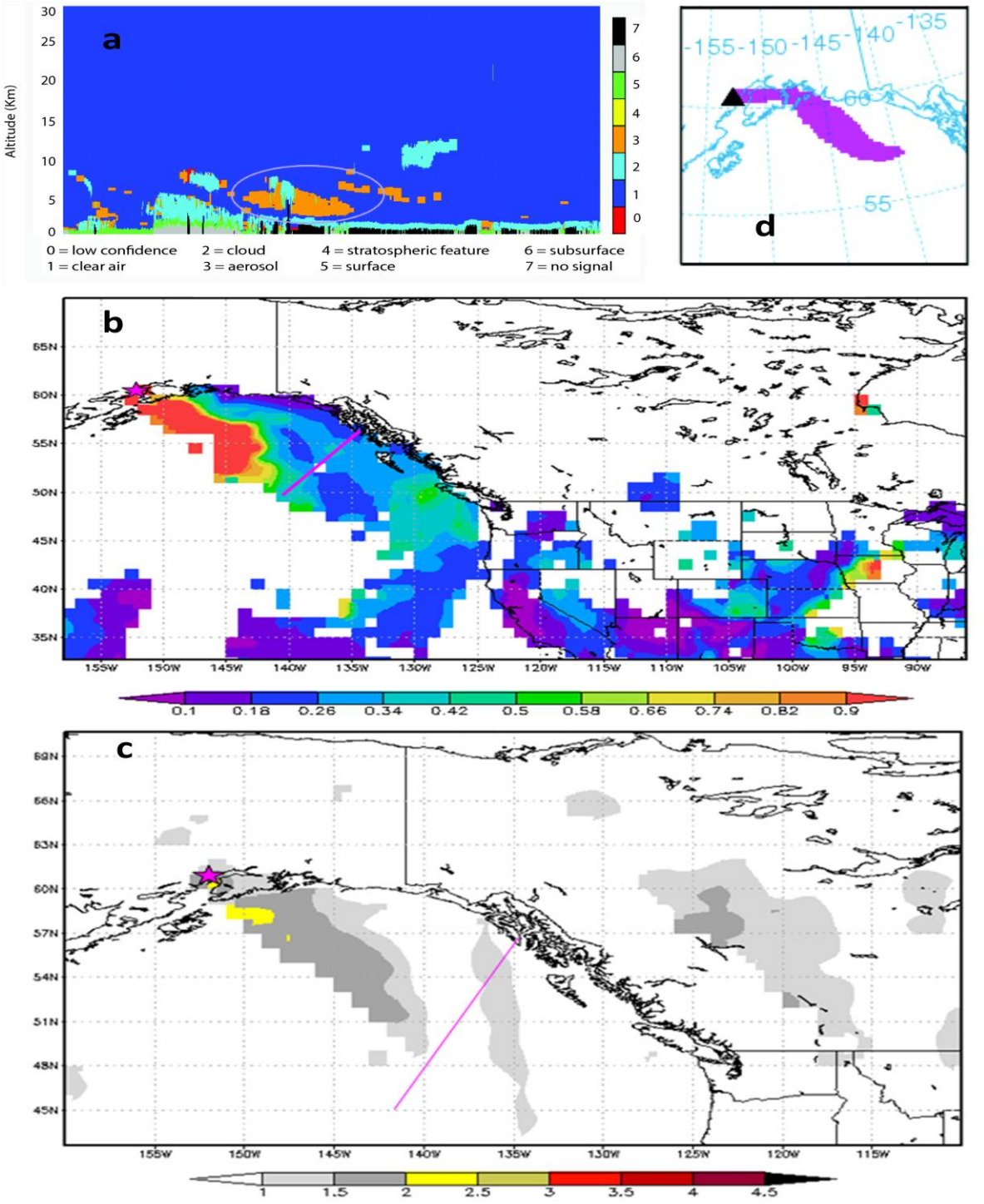

Figure 2.4: (a)Vertical feature mask from CALIPSO between 11:31 UTC and 11:45 UTC on April 2. The plume of interest is circled. (b) MODIS AOD(550 nm) daily mean for April 2. Mt. Redoubt is marked with a star. CALIPSO path is shown with a line. (c) Same as (b), except for OMI AI. (d) Transport of ash plume (shown in pink) from the April 2 eruption as predicted by the HYSPLIT model. Eruption duration of 12 hours and an ash column height of 4.6 km were used.

The plume thickness obtained from CALIPSO (Fig. 2.4a), together with total column AODs from MODIS, which range from 0.18 to 0.58 (Fig. 2.4b), suggest that this plume is moderately thin. Out of 22 CALIPSO overpasses in the selected domain, only the aerosol profile detected on April 2 clearly displays a well-defined vertical volcanic aerosol structure (Fig. 2.4a). In the absence of true color images on this day, the other sensors employed in this study, along with HYSPLIT, can confirm the volcanic origin of aerosol detected by CALIPSO. Both MODIS (Fig. 2.4b) and OMI (Fig. 2.4c) were able to detect volcanic aerosol, which appears to be traveling southeast of the volcano. On April 2, there were intermittent low level emissions throughout the day, according to plume heights compiled by the Alaska Volcano Observatory (AVO) from ground based radar estimates [*Carlile and Nelson*, 2009]. The HYSPLIT model predicts that ash from a low level eruption travels to the southeast of the volcano (Fig. 2.4d). Combined evidence from MODIS, OMI, and HYSPLIT confirms that the aerosol plume detected by CALIPSO is dominated by volcanic aerosols and that it has been carried away from its source.

For Mie calculations to determine optical properties of aerosol, it is essential to know if both ash and sulfate are present and proportions of ash to sulfate. Nonsphericity was detected in the April 2 plume using particle depolarization ratios from CALIPSO. Fragmented ash particles are expected to register nonspherical. The OMI AI image (Fig. 2.4c) also supports the presence of UV-absorbing aerosol, such as volcanic ash. The presence of ash or sulfate cannot be determined by MODIS AOD (550nm), because it detects both types of volcanic aerosol. However, proportions of fine and coarse mode aerosol can be constrained by MODIS fine mode fraction (Fig. 2.5).

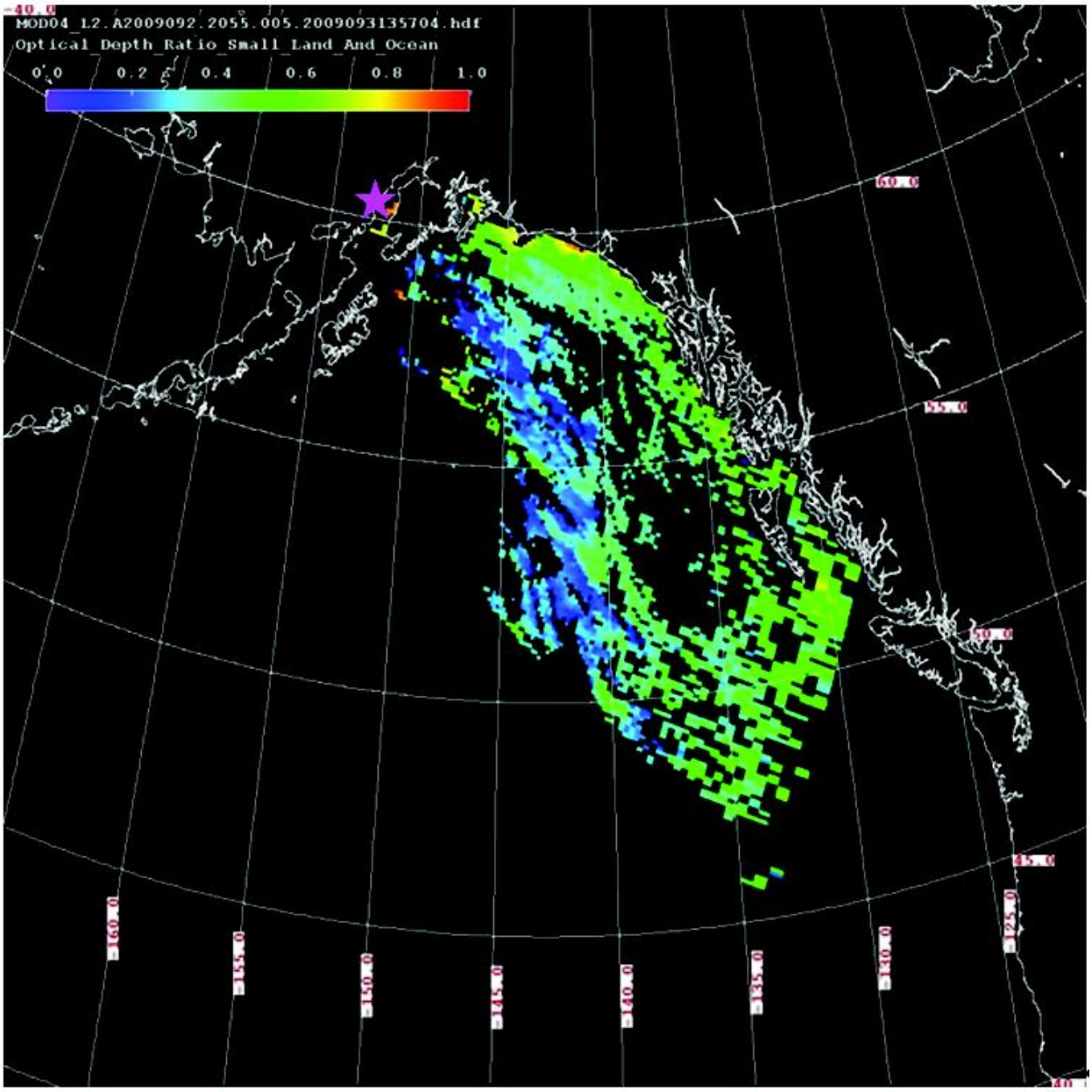

Figure 2.5: Terra MODIS fine mode fraction AOD on April 2 at 20:55 UTC. Mt. Redoubt is marked by a star.

In order to conservatively bracket the range of radiative forcing possible from this eruption, two volcanic aerosol compositions are considered, based on the highest and lowest values in the MODIS fine mode fraction (Fig. 2.5). The first composition was built to simulate a young, ash rich plume with an ash to sulfate ratio of 9 to 1, while the other composition represents an older, ash poor plume having an ash to sulfate ratio of 1 to 9.

However, the April 2 case study alone does not allow us to comprehensively assess the full range of radiative effects possible from this eruption. In order to better examine the role of vertical structure, we constructed a profile for a thick, optically opaque plume, forming directly over the volcano based on both the largest value of AOD and the maximum height for plumes detected throughout the course of the eruptions. The highest MODIS daily average AOD occurred on March 27, and values of MODIS AOD chosen ranged from 1 to 3 (Fig. 2.6).

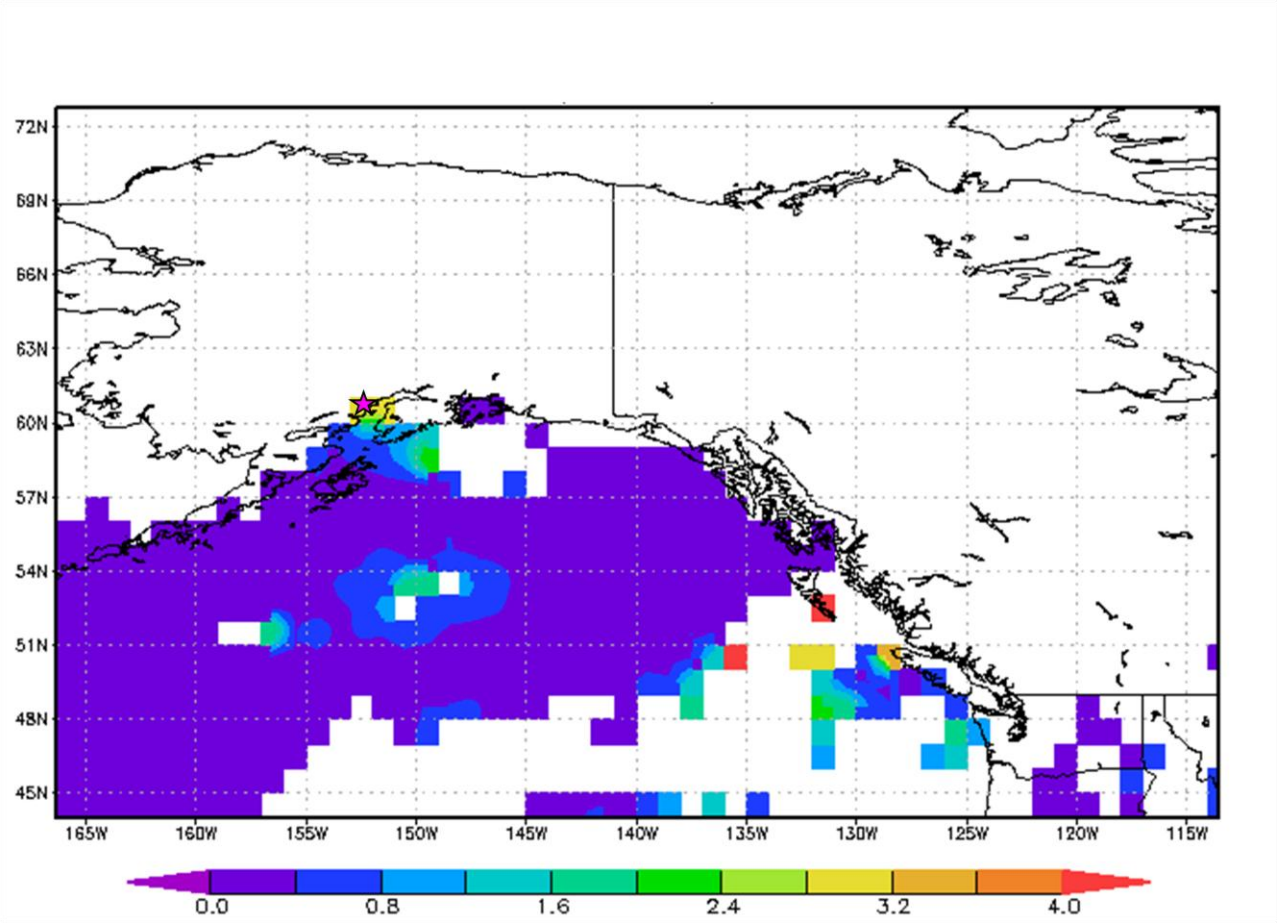

Figure 2.6: MODIS AOD(550 nm) daily average for March 27. These AOD values were the highest over the entire course of the explosive eruptions, due to aerosol produced by the very powerful eruption at 17:24 UTC on March 26 and the eruptions that followed on March 27.

The tallest plume height was produced by the 17:24 UTC eruption on March 26, reaching ~20 km [*Carlile and Nelson*, 2009; *Coombs and Schaefer*, personal communication, 2011]. The same aerosol compositions introduced for the plume detected on April 2 were used in this vertical structure in order to simulate plume aging.

2.3.3 The effect of volcanic aerosols on the Arctic radiation balance

We first consider the April 2 case and then examine the extent of the radiative effects by introducing a plume with a different vertical structure that was described in Section 3.2. Radiative forcings and heating/cooling rates were computed for the two plumes as they age and for a range of SZAs and surface albedos. Comparisons between the two plume profiles aid in determining the sensitivity of the radiative impact to plume structure and aerosol loading. Model input is summarized in Table 2.1.

2.3.3.1 Case study of volcanic plume detected on April 2

The plume detected on April 2, 2009 was an optically thin volcanic aerosol plume, stretching from 2.5 to 7 km in altitude and having a total column AOD at 550 nm ranging from 0.18 to 0.58. We use this case study to investigate the nature of volcanic aerosol and how plume aging and environmental parameters, such as surface albedo and SZA, influence the extent of the radiative impact. This is done for both SW and LW components. For a given set of environmental conditions, the effect of plume aging alone is to control the magnitudes of the radiative impact. Figure 2.7 displays the relationship between the net SW flux and AOD (550 nm) at the surface and TOA at SZA=55^{o}. Over both seawater and snow surfaces and for each AOD, the TOA net SW flux is greater for an ash rich plume than for a plume consisting primarily of sulfate (Fig. 2.7).

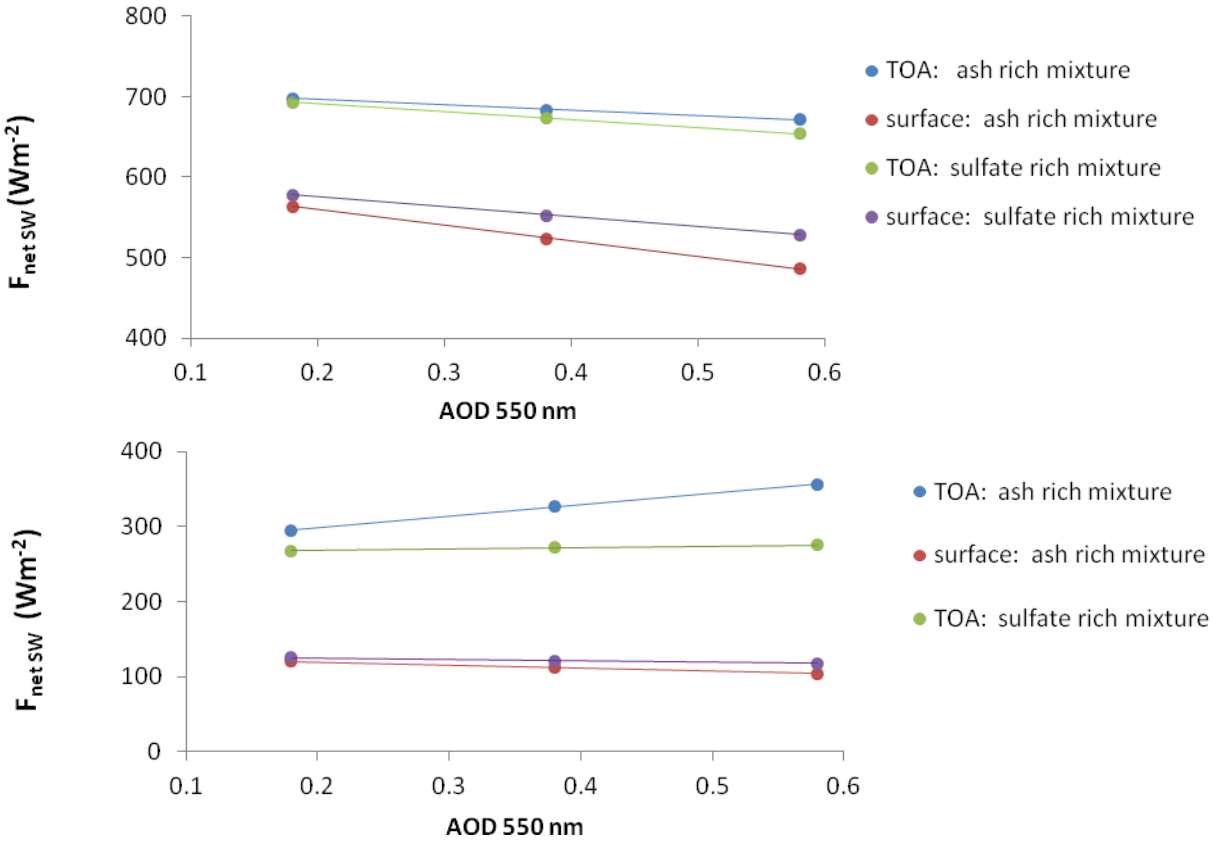

Figure 2.7: The relationship between net shortwave flux and AOD(550 nm) at an AOD range of 0.18 - 0.58 for two aerosol mixtures at the TOA and surface over seawater (top panel) and snow (bottom panel). Solar zenith angle is 55°. The R^2 regressions for all lines are greater than 0.99.

As shown in Fig. 2.1, the reason for this is that the sulfate rich mixture scatters SW radiation more efficiently than does the volcanic aerosol enriched in ash. Conversely, over both types of surfaces for each measured AOD, the net flux at the surface is less for an ash rich plume than for a plume dominated by sulfate. Due to more SW radiation being scattered by a sulfate rich plume, a smaller downward SW flux at the surface is to be expected, producing a lesser net flux at the surface than for an ash rich plume.

Figure 2.8a illustrates how aerosol composition and AOD affect the distribution of radiation in the atmosphere.

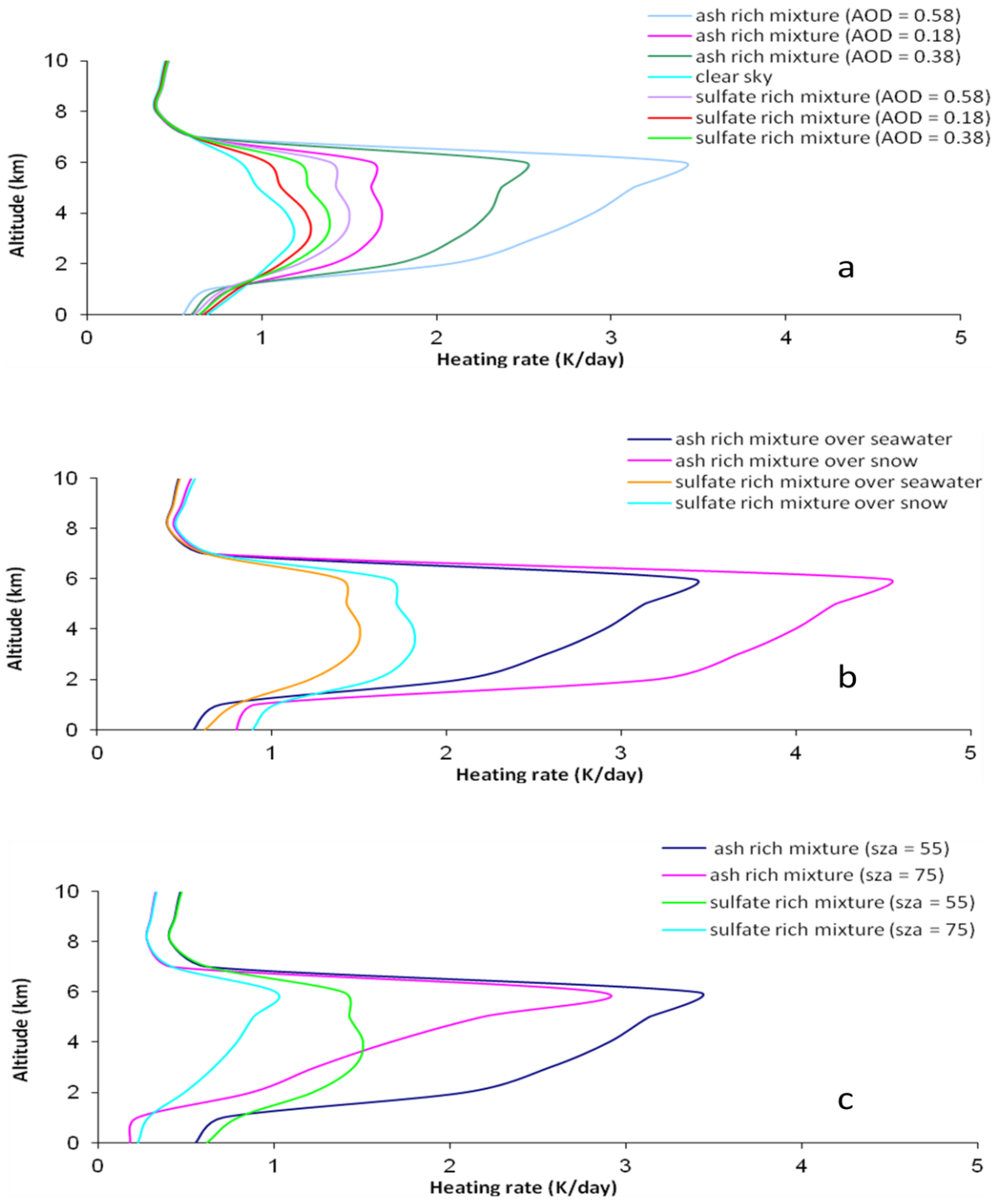

Figure 2.8: (a) The effect of aerosol composition and AOD(550 nm) of a thin plume (~2.5 – 7 km) on SW heating rate. SZA = 55^{o} and surface type is seawater for all cases. (b) The effect of aerosol composition of a thin plume (~2.5 – 7 km) and surface type on SW heating rate. SZA = 55^{o} and AOD(550 nm) = 0.58 for all cases. (c) The effect of aerosol composition of a thin plume (~2.5 – 7 km) and solar zenith angle (SZA) on SW atmospheric heating rate. The AOD(550 nm) = 0.58 and the surface type is seawater for all cases.

Ash rich mixtures lead to more heating in the layer and cooling at the surface, as do larger values of AOD. Compositions rich in ash warm more in the layer and cool more at the surface due to the ability of ash to absorb SW radiation. It is for this reason a volcanic layer containing ash will produce a more positive SW $DARFE_{atm}$, contributing to warming, and a more negative SW $DARFE_{surface}$, contributing to cooling (Table 2.2).

Table 2.2: Shortwave (SW) and total DARFE for a thin (~2 .5 – 7 km) plume in $Wm^{-2}AOD^{-1}$. DARFE was calculated for a range of AOD between 0.18 and 0.58.

Aerosol mixture	**Spectrum**	**solar zenith angle**	**surface type**	**DARFE TOA**	**DARFE surface**	**DARFE atm**
ash rich	SW	55^o	seawater	-65.7	-194.4	128.7
ash rich	SW	75^o	seawater	-64.0	-131.9	67.9
ash rich	SW	55^o	snow	151.0	-41.4	192.4
ash rich	SW	75^o	snow	55.3	-28.2	83.5
sulfate rich	SW	55^o	seawater	-98.1	-123.8	25.7
sulfate rich	SW	75^o	seawater	-90.6	-95.3	4.7
sulfate rich	SW	55^o	snow	18.7	-18.8	37.5
sulfate rich	SW	75^o	snow	-11.3	-18.3	7.0
ash rich	Total	55^o	seawater	-46.2	-155.3	109.1
ash rich	Total	75^o	seawater	-44.5	-92.8	48.3
ash rich	Total	55^o	snow	170.5	-2.3	172.8
ash rich	Total	75^o	snow	74.7	10.9	63.8
sulfate rich	Total	55^o	seawater	-91.8	-110.1	18.4
sulfate rich	Total	75^o	seawater	-84.3	-81.7	-2.6
sulfate rich	Total	55^o	snow	25.0	-5.2	30.2
sulfate rich	Total	75^o	snow	-5.0	-4.6	-0.3

However, the extent of warming in the layer and cooling at the surface in the SW not only depends on AOD and the relative age of volcanic aerosol, but also on surface albedo and SZA.

The surface albedo of the Arctic region in late winter or early springtime ranges from optically black seawater surfaces to highly reflective snow and ice surfaces. For both compositions of volcanic aerosol, surface and TOA net SW fluxes over snow are less than surface and TOA net fluxes over seawater (Fig. 2. 7). This is because the higher reflectivity of

snow causes the upward flux both at the surface and TOA to be greater, leading to smaller net fluxes. The TOA net fluxes for both compositions of volcanic aerosol increase with increasing AOD over snow and decrease with increasing AOD over seawater. This generally leads to positive $DARFE_{TOA}$ over snow and negative $DARFE_{TOA}$ over seawater for both volcanic compositions (Table 2.2). This tendency is due to multiple scattering between the surface and the volcanic layer over snow when AOD is increased. The exception to this rule, however, is the case of a sulfate rich plume over seawater at low SZA. In this case, $DARFE_{TOA}$ is negative because the effect of multiple scattering is drowned out by opposing effects of the composition and SZA.

The effect of multiple scattering over highly reflective surfaces on heating rates can be observed in Fig. 2.8b. A volcanic layer over snow will absorb more SW radiation due to multiple scattering, warming more in the atmosphere than the same layer over seawater. For a more absorbing aerosol type, such as one comprised mostly of ash, this effect is even more pronounced.

In the Arctic, the changing of seasons brings dramatic shifts of incoming SW radiation. In the summer, the sun never sets, and in winter, the region is in perpetual darkness. Here, DARFE is computed for the highest SZA for a day in mid March (55^{o}) and a lower SZA chosen to represent a middle point between the highest and lowest daily sun angles (75^{o}). A high sun (SZA = 55^{o}) leads to a larger downward SW flux at TOA. Figure 2.8c illustrates well that when more radiation is entering the system, the heating within the atmosphere is enhanced, especially for a volcanic layer containing larger proportions of absorbing ash. The effect of a low sun (SZA = 75^{o}) on SW DARFE is to decrease the extent of warming or

cooling at TOA, at the surface and in the atmosphere (Table 2.2). Therefore, an eruption occurring very close to the winter solstice would have a negligible SW radiative effect.

However, both SW and LW radiation must be considered to determine the net radiative impact of a volcanic plume. In some cases, such as during boreal winter, the LW radiation may be more important than SW radiation. From Fig. 2.1, it is apparent that ash absorbs more SW radiation. Both ash and sulfate absorb and scatter LW radiation, and ash is better overall at attenuating it (Fig 2.1). This results in net LW TOA fluxes and net surface LW fluxes for sulfate that are more negative than for ash (Fig. 2.9). The effect of volcanic aerosols on the LW cooling rate profile is shown in Fig. 2.10.

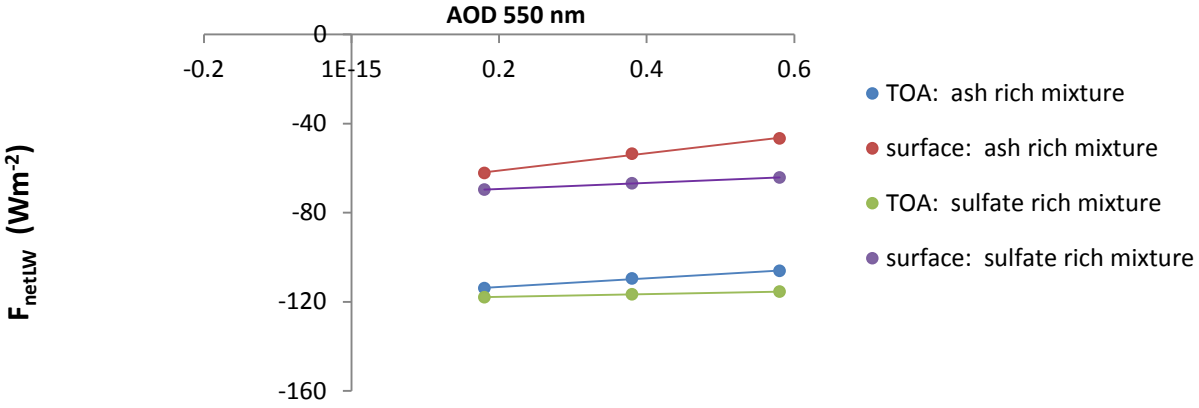

Figure 2.9: The relationship between net LW flux and AOD(550 nm) at an AOD range of 0.18 - 0.58 for two aerosol mixtures at the TOA and surface. The R^2 regressions for all lines are greater than 0.99.

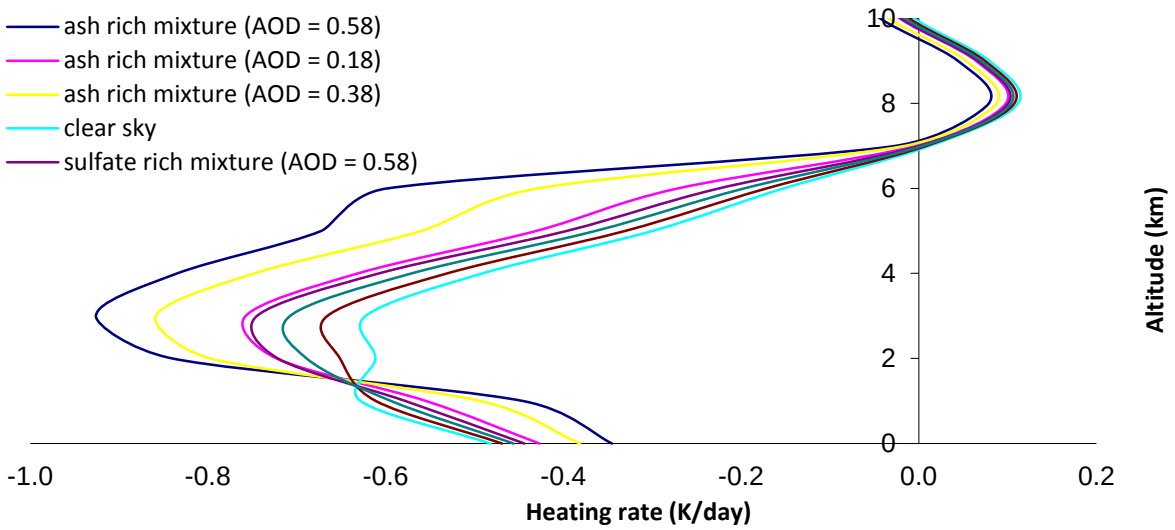

Figure 2.10: The effect of aerosol composition and AOD(550 nm) of a thin plume (~2.5 – 7 km) on LW cooling rate.

Overall, volcanic aerosols cause cooling in the atmosphere and warming at the surface. The extent of atmospheric cooling or surface warming is dependent upon the aerosol composition and AOD. Compositions rich in ash produce more pronounced cooling in the atmosphere and warming at the surface, because ash is a better absorber of SW radiation and emitter of LW radiation. This effect can also be observed in LW DARFE calculations, which range from 19.5 to 6.3, 39.1 to 13.6, and -19.6 to -7.3 $Wm^{-2}AOD^{-1}$ for ash and sulfate rich cases at the TOA, surface and within the atmosphere, respectively.

The total radiative forcing associated with this volcanic plume at TOA, at the surface, and in the atmosphere is reported in Table 2.2. The total DARFE is the sum of SW and LW DARFEs for each case. In most cases, the SW radiation contributes more to the total DARFE. However, there were three instances in which the LW radiation was significant enough to change the sign of the forcing either at the surface or in the atmosphere. These cases were all at a lower zenith angle and either consisted of ash rich plumes over snow or sulfate rich plumes over seawater and snow. The SW $DARFE_{suface}$ for an ash rich plume over snow at a

lower zenith angle produces less cooling than a similarly composed plume under other environmental conditions because of the multiple scattering effect between the aerosol layer and the snow surface and the reduction of solar radiation entering the system due to the lower zenith angle. In this case, LW radiation heats the surface more than the SW radiation cools it, causing a net radiative heating of the surface. A sulfate rich plume under low SZA will tend to warm the atmosphere less than an ash rich plume. This is due to both a reduction in incoming solar radiation and the inability of sulfate to absorb SW radiation. The single scattering albedo (550 nm) for the ash rich plume is ~ 0.89, but it is considerably higher (~ 0.98) for the sulfate rich plume, indicating there is no appreciable absorption at this wavelength (Fig. 2.1). For cases of a sulfate rich plume at low SZA over seawater and snow, LW radiation cools the atmosphere more than the SW radiation warms it, which leads to a net cooling of the atmosphere. These calculations demonstrate the importance of both SW and LW components of the forcing when determining the radiative effects of an aging volcanic plume, especially in the Arctic.

2.3.3.2 Examining the role of vertical structure of volcanic aerosol plumes

The simulated plume for an optically and physically thick eruption column was based on satellite data collected for the entire span of the eruption. A range of AODs from 1 to 3 was selected, and the plume thickness stretched from 3 km (the volcano summit) to 20 km altitude. We compared calculated DARFEs and heating rates for an optically thick plume to those produced for the optically thin plume. In this section we demonstrate that, in general, the trends for surface type, SZA, and plume composition discussed above for the thin plume still hold for the thicker plume. However, we also show that the magnitude and, in a few

cases, the sign of the forcings and the magnitudes of the heating/cooling rates are very much dependent on plume thickness and AOD.

Net SW fluxes at each AOD for the thick plume over both snow and seawater are shown in Fig. 2.11.

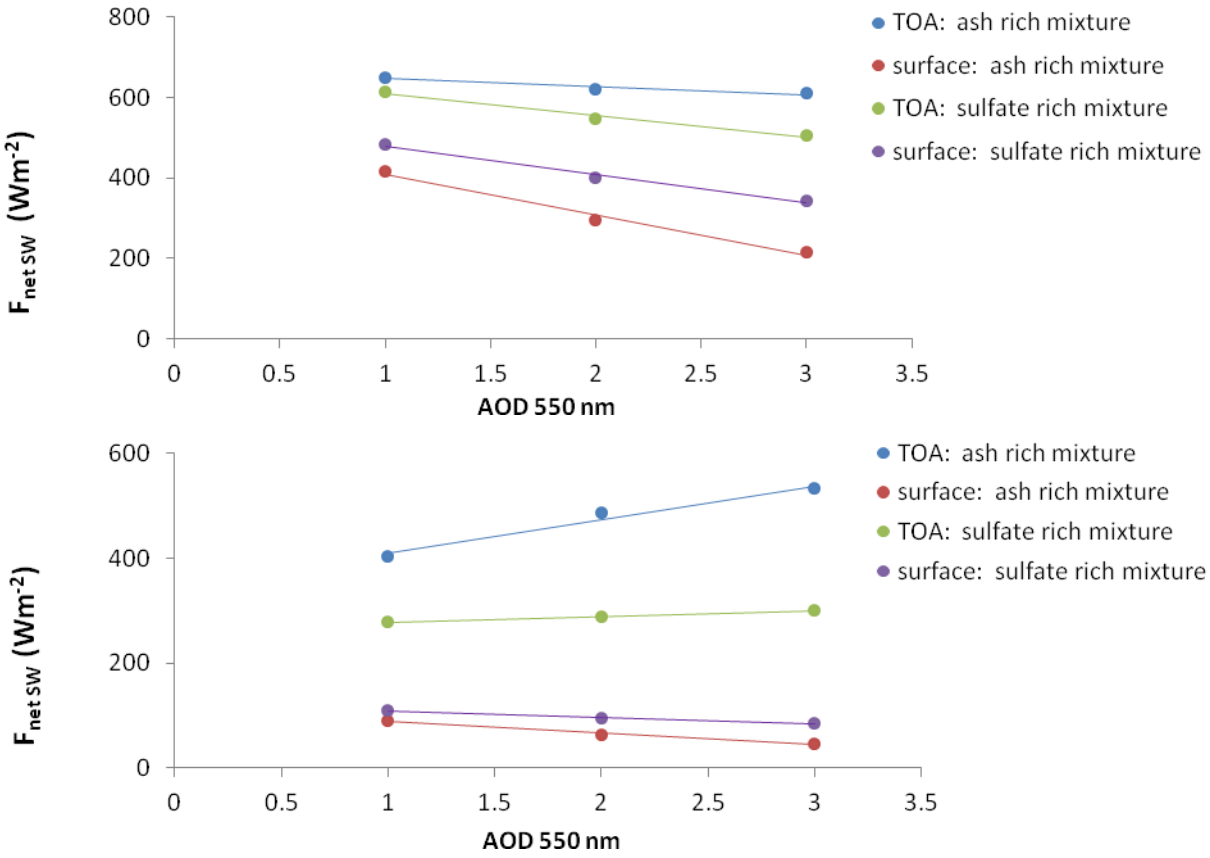

Figure 2.11: The relationship between net SW flux and AOD(550 nm) at an AOD range of 1 - 3 for two aerosol mixtures at the TOA and surface over seawater (top panel) and snow (bottom panel). SZA is 55°. The R^2 regressions for all lines are greater than 0.95.

Comparing these results to those for the thin plume in Fig. 2.8, it is apparent that net SW fluxes for the thick plume over seawater, both at the surface and TOA, are considerably less than those for the thin plume at the ranges of AOD chosen for each plume. This is because more of the incoming SW radiation is scattered and absorbed in the thick plume case, resulting in less incoming SW radiation reaching the surface, and therefore less SW radiation

reflected by the surface. Surface net SW fluxes over snow are greater for the thin plume than for the thick one for the same reasoning. However, net SW fluxes are greater for the thick plume at TOA. This is due to less outgoing radiation at TOA because of enhanced multiple scattering occurring between the snow surface and the more opaque plume. Another important comparison in net SW fluxes between plumes is the differences between the two volcanic aerosol compositions at each AOD. For the thicker plume, it seems that plume composition, and therefore plume age, can cause net SW fluxes at the surface and TOA to differ substantially more than for a thinner plume. Calculations of net SW flux must be more sensitive to composition of volcanic aerosol for a thicker plume.

Table 2.3 presents SW DARFEs computed for the thick plume. Like SW DARFE for the thin plume (Table 2.2), $DARFE_{surface}$ is negative, indicating cooling, and positive in the atmosphere, indicating warming. However, DARFE values for the thick plume cases are much smaller in magnitude than those for thin plumes. This is a result of the range of AOD over which net flux calculations were performed. The relationship between net flux and AOD can only be approximated as linear when AOD values are small. Because DARFE is computed as the slope of this line, it may depend on the ranges of AOD chosen and must always be reported with this AOD range attached in order to be a meaningful quantity. For the thin plume, the range of AOD used to compute DARFE is narrower and the AOD values are smaller. The net fluxes for the thin plume are more sensitive to changes in AOD at the range chosen, leading to larger DARFE values. However, DARFE is reported in units of $Wm^{-2}AOD^{-1}$, and therefore the thick plumes may still produce a larger forcing in Wm^{-2} depending on the exact values of AOD present.

Shortwave heating rates for the thick plume also exhibit the same general dependencies on composition, surface albedo, and SZA as described for the thin plume, with warming in the atmosphere and cooling at the surface (Fig. 2.12).

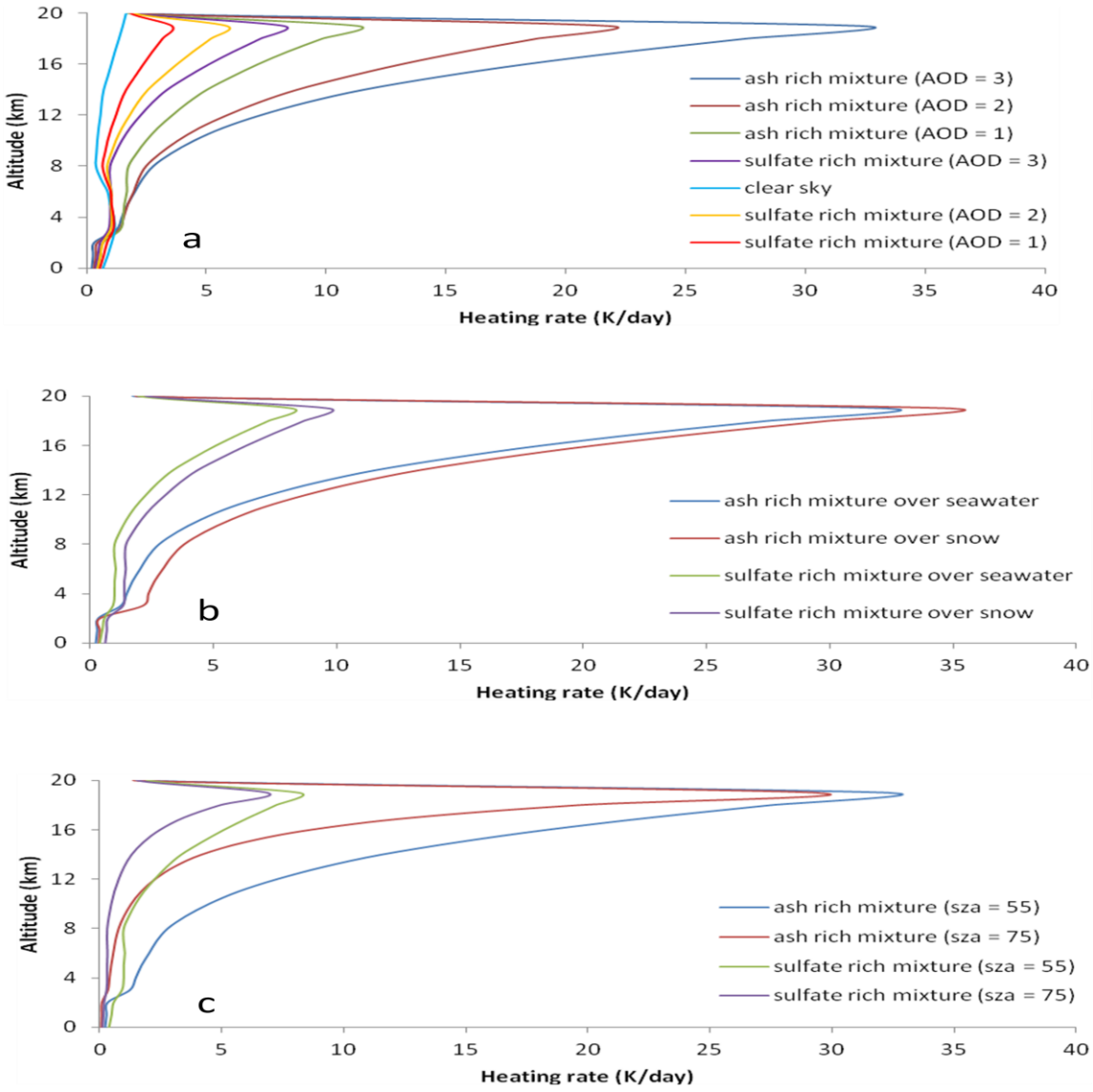

Figure 2.12: (a) The effect of aerosol composition and AOD(550 nm) of a thick plume (~3 – 20 km) on SW heating rate. SZA = 55^{o} and surface type is seawater for all cases. (b) The effect of aerosol composition of a thick plume (~3 – 20 km) and surface type on SW heating rate. SZA = 55^{o} and AOD(550 nm) = 3 for all cases. (c) The effect of aerosol composition of a thick plume (~3 – 20 km) and solar zenith angle (SZA) on SW heating rate. AOD(550 nm) = 3 and the surface type is seawater for all cases.

However, SW heating rates for the thick plume exhibit significant perturbations to clear sky conditions (Fig. 2.12a), which dwarf those due to the thin volcanic plume discussed above. Heating rates for the thick plume are particularly sensitive to aerosol composition (Fig. 2.12a), but have lesser sensitivities to surface reflectivity (Fig. 2.12b) and SZA (Fig. 2.12c). This finding emphasizes how strongly plume age controls the way SW radiation is distributed within the aerosol layer and throughout the atmosphere.

The importance of plume age is magnified in the LW part of the spectrum. Given a fixed temperature profile, the LW radiative impacts are entirely dependent on composition and opacity of the aerosol layer, which change as the plume evolves. Net LW fluxes for the thick plume increase with increasing AOD (Fig. 2.13), similarly to net LW fluxes for the thin plume.

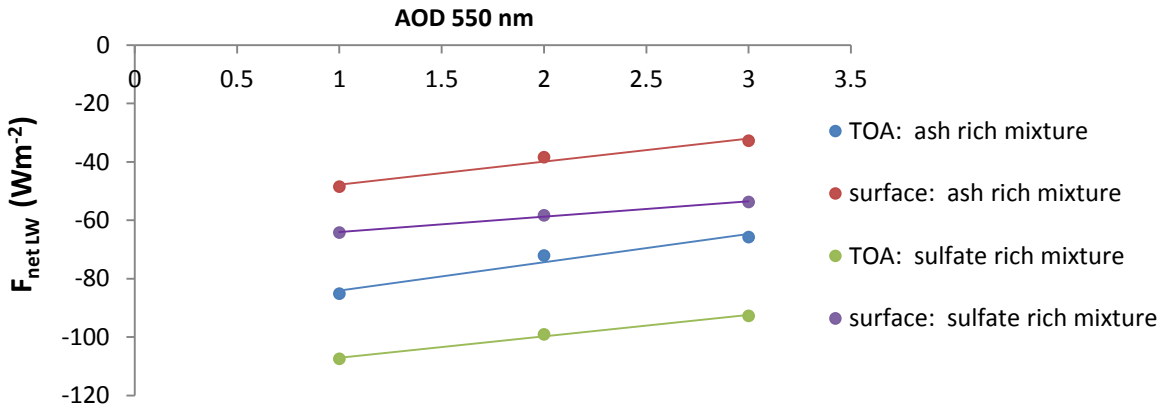

Figure 2.13: The relationship between net LW flux and AOD(550 nm) at an AOD range of 1 - 3 for two aerosol mixtures at the TOA and surface. The R^2 regressions for all lines are greater than 0.96.

However, the differences at TOA and at the surface between the two compositions of volcanic aerosols at each AOD are greater for the thick plume than for the thin plume, indicating that plume age plays a larger role in determining net LW fluxes for a thicker plume. Net LW fluxes also tend to be less negative, both at the surface and TOA, for the thick plume than for

the thin plume of the same aerosol composition. A thick layer will emit more LW radiation, producing a net LW flux at the surface which is less negative than for a thin plume. The thick plume will also scatter and absorb more outgoing LW radiation coming from both the surface and within the lower layers of the plume, producing net LW fluxes at TOA that are typically less negative.

The slopes of the lines in Fig. 2.13 give the LW DARFE for the thick plume cases, which range from 9.8 to 7.4, 8.0 to 5.3, and 1.8 to 2.1 $Wm^{-2}AOD^{-1}$ for ash and sulfate rich cases at the TOA, surface, and within the atmosphere, respectively. Longwave DARFE for the thick plume is less than those for the thin plume, because net LW fluxes for the thick plume are less sensitive to changes in AOD at the ranges of AOD chosen. Unlike the thin plume cases, $DARFE_{TOA}$ is greater than $DARFE_{surface}$ for both compositions of volcanic aerosol, leading to positive $DARFE_{atm}$ for the thick plume. For the thick plume cases, the way in which LW radiation is distributed in the atmosphere is very different. Longwave cooling rates for each aerosol composition and AOD are displayed in Fig. 2.14.

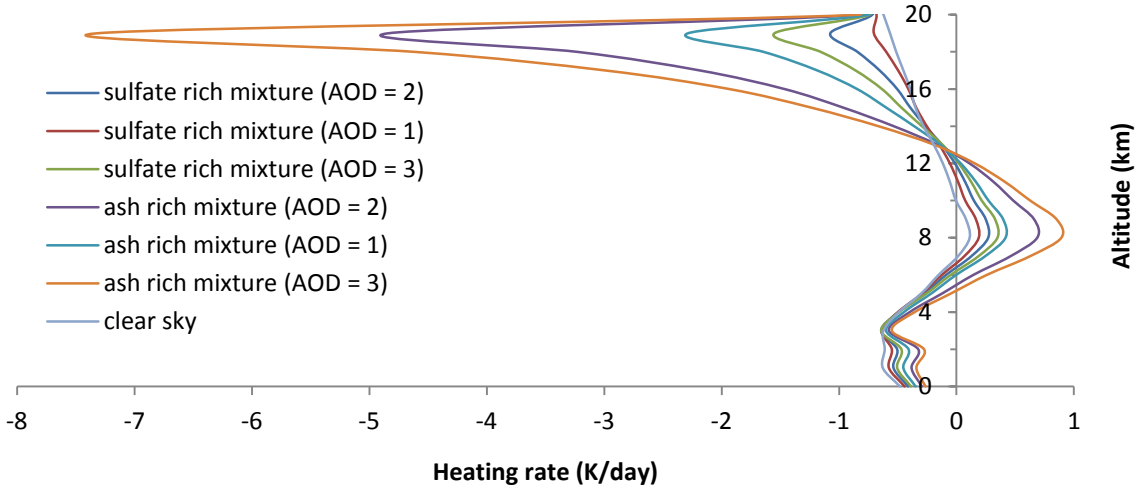

Figure 2.14: The effect of aerosol composition and AOD(550 nm) of a thick plume (~3 – 20 km) on LW cooling rate.

Emission of LW radiation in the upper layers causes cooling in the upper atmosphere, while the surface layers warm due to emission by middle to lower layers and the surface. Longwave emission from the upper and lower layers causes enhanced warming in middle layers.

The overall radiative effect of volcanic aerosol in a thick plume is given by the total DARFE, and this is reported for each case in Table 2.3.

Table 2.3: Shortwave (SW) and total DARFE for a thick (~3 – 20 km) plume in $Wm^{-2}AOD^{-1}$. DARFE was calculated for a range of AOD between 1 and 3. *For this case, $DARFE_{TOA}$ was not linear at broader AOD ranges, so it was calculated in an AOD range of 1 to 1.5.

Aerosol mixture	Spectrum	Solar zenith angle	Surface type	DARFE TOA	DARFE surface	DARFE atm
ash rich	SW	55^o	seawater	-20.1	-100.4	80.3
ash rich	SW	75^o	seawater	-6.7	-29.9	23.2
ash rich	SW	55^o	snow	64.2	-21.3	85.5
ash rich	SW	75^o	snow	17.7	-6.4	24.1
sulfate rich	SW	55^o	seawater	-54.2	-70.1	16.0
sulfate rich	SW	75^o	seawater	-20.6	-23.4	2.9
sulfate rich	SW	55^o	snow	11.0	-12.5	23.6
sulfate rich	SW	75^o	snow	-2.3*	-4.6	5.3
ash rich	Total	55^o	seawater	-10.3	-92.4	82.1
ash rich	Total	75^o	seawater	3.1	-21.9	25.0
ash rich	Total	55^o	snow	74.0	-13.4	87.6
ash rich	Total	75^o	snow	27.5	1.6	25.9
sulfate rich	Total	55^o	seawater	-46.8	-64.8	18.0
sulfate rich	Total	75^o	seawater	-13.2	-18.1	4.9
sulfate rich	Total	55^o	snow	18.4	-7.2	25.6
sulfate rich	Total	75^o	snow	5.1	0.7	4.3

For most cases, SW radiation was larger than LW. However, for four of cases under lower sun conditions, LW radiation was large enough to change the sign of the total forcing. At the surface, a net warming was produced for both ash rich and sulfate rich compositions over snow. In these cases, surface SW cooling is reduced due to a reduction of solar energy entering the system and multiple scattering between the snow surface and the aerosol layer. TOA warming was produced for an ash rich plume over seawater and a sulfate rich plume

over snow. In these cases, LW warming at TOA was enough to counteract SW cooling. For all of the thick plume cases, net warming in the atmosphere due to SW radiation is enhanced by positive values of LW DARFE.

2.3.4 Comparing radiative impacts of major aerosol types in the Arctic

The radiative effect of aerosol in a given environment depends upon aerosol-specific properties, such as optical characteristics and vertical loading. Volcanic aerosol is unique in that volcanoes are capable of producing huge loadings, forming plumes that can stretch from near surface level to well into the stratosphere. Therefore, it is obvious from the nature of volcanic eruptions that they may produce thicker plumes and may thereby drown out the signal from any other aerosols present. To compare the radiative impact of volcanic aerosol to other aerosol types, Figure 2.15 presents direct radiative forcings and heating rates for two volcanic aerosol compositions for the April 2 case from our study, mineral dust [*Stone et al*., 2007), wildfire smoke [*Stone et al*., 2008), and haze [*Quinn et al*., 2007; *Ritter et al*., 2005].

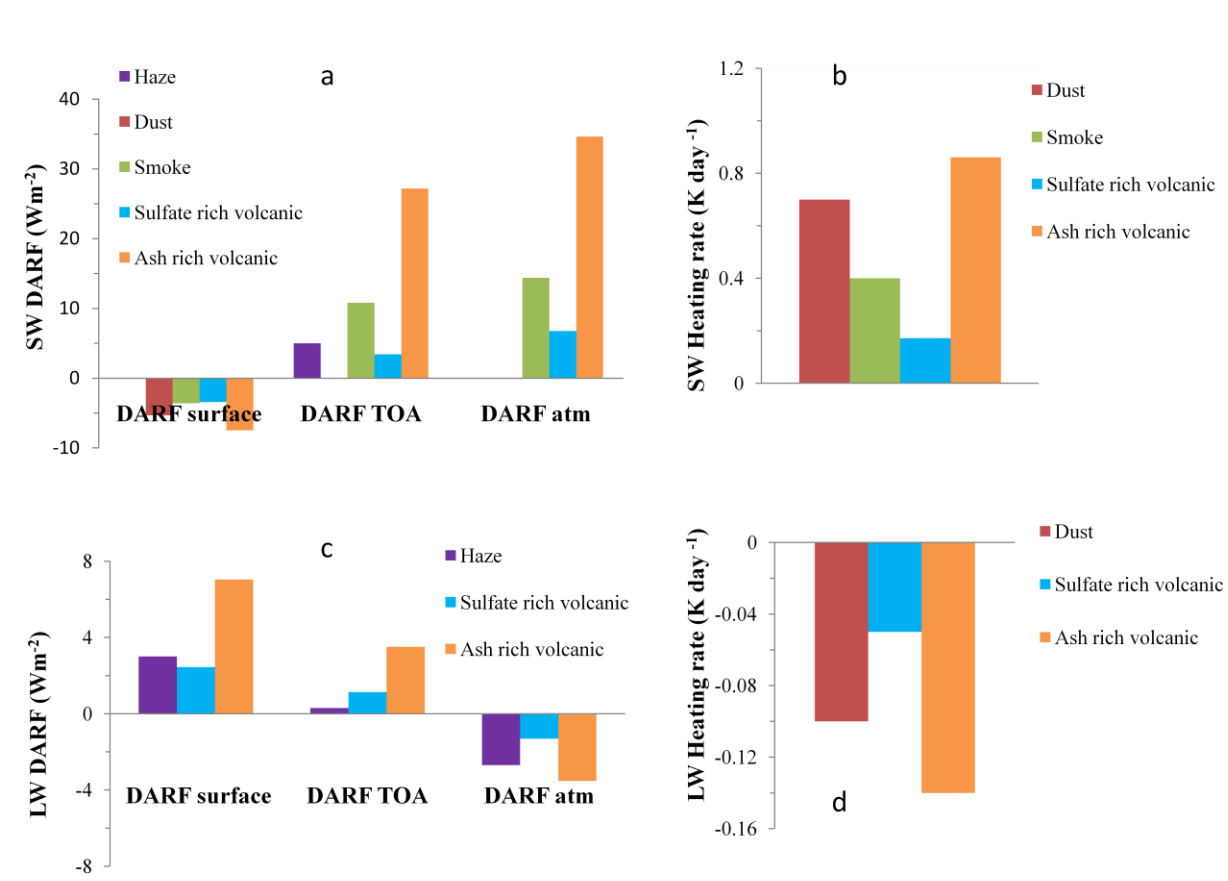

Figure 2.15: (a) SW direct radiative forcings (DARFs) and (b) SW heating rates for haze [*Quinn et al*., 2007], dust [*Stone et al*., 2007], smoke [*Stone et al*., 2008], and ash rich and sulfate rich volcanic aerosols (this study). Values of forcing for dust were only available at the surface. (c) LW DARFs for haze [*Ritter et al*., 2005] and ash rich and sulfate rich volcanic aerosols (this study). (d) LW cooling rates for dust [*Stone et al*., 2007] and ash rich and sulfate rich volcanic aerosols (this study).

While there are multiple factors which control the regional radiative impact, the most comparable surface albedo, AOD, SZA, and plume thickness for each study were selected in efforts to only assess the effects of differing aerosol compositions and size distributions (Table 2.4).

Table 2.4: Studies chosen for comparisons of DARF and heating rates (HR) of Arctic aerosols, along with aerosol types, surface albedo, AOD at 500 or 550 nm, ω_0 (singe scattering albedo) at 550 nm, solar zenith angle (SZA), vertical plume thickness and placement within the atmosphere that were used. Boxes filled with an X indicate information was not available. [a] TOA SW DARF for SZA=62.6^o obtained from Dr. Quinn, [*personal communication*, 2011]. [b] Vertical placement of the layer is unknown, but thickness is reported as 1 km.

Study	Aerosol type	Quantity	Surface albedo	AOD	ω_o (550 nm)	SZA	Placement (km)
Quinn et al., 2007	haze	SW DARF	0.92	0.12	0.94	daily mean[a]	X[b]
Stone et al., 2007	dust	SW DARF	0.825	0.18	0.89	62	2 - 4
		SW HR	0.830	0.15	0.89	75	2 - 4
		LW HR	N/A	0.4	0.89	N/A	2 - 4
Stone et al., 2008	smoke	SW DARF	0.8	0.18	0.95	50	0.25 - 2.8
		SW HR	0.2	0.28	0.95	65	0.25 – 2.8
Ritter et al., 2005	haze	LW DARF	N/A	X	X	N/A	X
This study	Sulfate rich volcanic	SW DARF	0.973	0.18	0.98	55	2.5 -7
		SW HR	0.973	0.18	0.98	75	2.5 - 7
		LW DARF	N/A	0.18	0.98	N/A	2.5 - 7
		LW HR	N/A	0.18	0.98	N/A	2.5 - 7
This study	ash rich volcanic	SW DARF	0.973	0.18	0.89	55	2.5 -7
		SW HR	0.973	0.18	0.89	75	2.5 - 7
		LW DARF	N/A	0.18	0.89	N/A	2.5 – 7
		LW HR	N/A	0.18	0.89	N/A	2.5 - 7

Figure 2.15a compares the surface SW DARF. The ash rich volcanic mixture attenuates more solar radiation per AOD than any other compositions, producing the most negative surface forcing. Mineral dust runs a close second to the ash rich mixture, indicating

dust must have similar SW extinction coefficients. The ash rich mixture also produces the most warming at TOA and within the atmosphere, which is because the ash rich mixture is the better absorber of SW radiation, as further illustrated by the SW heating rates in Fig. 2.15b. At the TOA, the DARFs of the sulfate rich mixture and haze are very similar. This may be due to the haze presented in *Quinn et al*. [2007] consisting of large proportions of sulfate.

The LW DARFs for the two compositions of volcanic aerosol and haze [*Ritter et al*., 2005], and LW cooling rates for the two volcanic mixtures and dust [*Stone et al*., 2007] are compared in Fig. 2.15c and 2.15d, respectively. The LW forcing for smoke is very small because of small particle sizes [*Myhre et al*., 2007] and is not shown here. LW forcings of dust and volcanic aerosols are important, although seldom calculated in radiative studies of Arctic aerosols. The ash rich mixture seems to dominate the LW radiation as well. Both SW and LW comparisons indicate that even a moderately thin layer of ash rich volcanic aerosol can be a main driver of the aerosol induced radiative impact in the Arctic region. Additionally, the signal due to volcanic aerosol would be expected to be even more powerful given that volcanic eruptions routinely produce aerosol layers with AODs and vertical thicknesses much larger than those of other aerosol types.

2.4 Conclusions

The 2009 eruption of Redoubt volcano provided a source of aerosol to the Arctic environment. The extent to which a given volcanic aerosol layer perturbs the radiation balance depends upon environmental factors, such as surface reflectivity and SZA, and plume specific factors, such as aerosol composition and size distributions, and vertical profile of AOD. We used a satellite integrated approach to investigate the role these factors play in determining the radiative impact of volcanic aerosols in the Arctic. In general, environmental factors can

govern both the sign and magnitude of the DARF, DARFE and heating/cooling rates. The ability of environmental conditions to change whether an aerosol layer will warm or cool at TOA and the surface is especially significant when considering the Arctic region, where surfaces vary from ocean to snow, and seasons dramatically shift the amount of incoming solar radiation. The deposition of volcanic ash onto ice and snow surfaces also has strong potential to greatly alter surface reflectivity and thereby cause a perturbation that may last long after the aerosol plume has gone.

Plume specific factors influence the magnitudes of DARF, DARFE and heating/cooling rates. The compositions, thicknesses and AODs of volcanic plumes vary greatly and are in many cases difficult factors to constrain. Due to the remote locations of many volcanoes and the dangers involved in making direct measurements, satellites are absolutely necessary to monitor the spatial and temporal development of volcanic plumes. However, eruption specific size distributions and ash to sulfate ratios are challenging to constrain, even with the help of satellite sensors. The development of multiphase models [*Dufek and Bergantz*, 2007; *Neri et al*., 2007] to study eruption dynamics may assist in creating better microphysical models for volcanic aerosol. Other plume related simplifications that are often made in radiative transfer modeling which need to be addressed include: the partitioning of volcanic aerosol types at different altitudes and the nonsphericity of ash.

Volcanic eruptions are high intensity events, capable of providing a huge, sporadic aerosol signal compared to other Arctic aerosols. However, volcanic eruptions typically have durations shorter than the season long occurrences of Arctic haze or wildfire smoke. Like other Arctic aerosols, volcanic aerosols from high northern latitude eruptions can cover large areas, as in the recent eruption of Eyjafjallajökull in Iceland, which disrupted air travel across Europe.

According to the AVO, Alaskan volcanoes have had an average eruption frequency of two per year over the past 40 years, but the appearance of Arctic haze, wildfire smoke, and dust occur only yearly. Therefore, Alaskan volcanic eruptions are on average more frequent than events responsible for the emission of Arctic haze, wildfire smoke, and dust into the Arctic environment. Depending on the time of year, volcanic aerosol may be present along with other aerosol types. Following an eruption in Arctic springtime, dust, haze and volcanic aerosol can contribute to the overall aerosol signal. For eruptions in boreal summer, wildfire smoke will be present along with volcanic aerosols. In boreal winter, aerosols from a volcanic eruption will be accompanied by haze.

Our results demonstrate a potential for volcanic aerosol to provide a sizeable contribution to the radiative effects and even outshine other types of aerosol when significant proportions of volcanic ash are present, as in young volcanic plumes. Therefore, volcanic aerosol, although sporadically present, can have a significant radiative impact in the region. We recommend that volcanic aerosols be included in future assessments of the Arctic regional radiation budget. This will facilitate efforts to understand the radiative impacts of natural aerosols on the Arctic environment in order to create successful mitigation strategies for warming due to anthropogenic sources.

CHAPTER 3

ASSESSMENT OF DEPOSITIONAL ASH LOADINGS FROM THE 2009 ERUPTION OF MT. REDOUBT

The work presented in this chapter has been submitted to the Journal of Volcanology and Geothermal Research and publication has been recommended

[Young et al., 2014]

3.1 Introduction

Surface reflectivity is an important factor in controlling the regional Arctic radiation balance [e.g. *Anisimov et al*., 2007]. According to the 2005 Arctic Climate Impact Assessment (ACIA), changes in regional climate could damage ecosystems and have negative impacts on the health and the economic stability of human populations (www.acia.uaf.edu). In the Arctic, the surface reflectivity and sun angle can vary widely depending on time of year and can change the magnitude, and even the sign, of the radiative effects [*Stone et al*., 2008; *Young et al*., 2012]. Volcanic ash deposited onto ice and snow covered surfaces is expected to alter surface reflectivity and cause early snowmelts in a manner similar to dust [*Painter et al*., 2010] and soot [*Flanner et al*., 2007]. However, we are unaware of any studies to date that assess the radiative impacts due to volcanic ash deposition in the Arctic.

High northern latitude volcanic eruptions are capable of emitting large quantities of ash into the Arctic environment, and these events occur quite frequently. In fact, there are ~ 4 volcanoes currently erupting and ~ 10 volcanoes experiencing unrest above 55^{o}N, as of October 2013 (www.volcanodiscovery.com). The Alaska Volcano Observatory (AVO) reports that in Alaska alone there are on average two eruptions each year. Ash deposited from volcanic

eruptions can remain long after an eruption has ended and may thereby have greater radiative impacts than an eruptive plume. This is particularly true in the Arctic region, where snowfall that could cover deposits is sparse due to the dry climate.

The 2009 eruption of Mt. Redoubt was selected as a case study to assess volcanic ash deposits because of reports of extensive deposit areas and documented early snowmelts due to the deposition of ash onto ice and snow covered surfaces [*Schaefer et al*., 2012]. Mt. Redoubt is a stratovolcano located in Alaska, USA (60.49 N, -152.74 W). According to the AVO, deposits from this event were reported in the Alaskan cities of Anchorage, Kenai, Homer, Seldovia, Skwentna, and Talkeetna, with trace amounts as far north as Fairbanks. Because of changing meteorology during the entire course of explosive activities, ash was deposited hundreds of kilometers away in nearly every direction from the source volcano. Deposits occurred over both land and ocean, but larger areal extents of ash were deposited over land ice and snow covered surfaces.

The areal extent of ash deposits can be obtained directly from field observations and satellite measurements. However, field observations are made only at a few locations, making satellites instrumental at providing the coverage necessary to gain knowledge of the areal extent of the deposits. The Moderate Resolution Imaging Spectroradiometer (MODIS) instrument flying aboard Aqua and Terra satellites and the Ozone Monitoring Instrument (OMI) on the Aura spacecraft are two such sensors capable of detecting volcanic ash. Both sensors are on polar orbiting satellites, which provide excellent coverage of the Arctic region, allowing for mapping out the spatial extent of volcanic plumes and deposits. The MODIS instrument provides true color images of ash plumes and deposits and aerosol optical depth (AOD) of volcanic plumes. The OMI sensor provides a UV aerosol index (AI), which can detect the presence of UV

absorbing aerosols, such as ash, dust, and smoke. However, in the Arctic, environmental conditions, such as meteorological clouds and high surface reflectivities, often hamper retrievals for passive instruments measuring in the visible and UV, such as MODIS and OMI.

In cases with sparse satellite and field data, transport models can aid in providing the quantitative characterization of volcanic aerosols and ash deposits. Past studies have used General Circulation Models (GCMs) to simulate the transport and deposition of volcanic ash [e.g., *Niemeier et al*., 2009]. However, the source conditions (i.e., distribution of ash in the eruptive column) of volcanic eruptions are not treated in GCMs, which handle volcanic eruptions by assigning a flux amount of material into the atmosphere [*Kravitz et al*., 2011; *Robock et al*., 2009; *Robock et al*., 1995]. Neglecting the dynamics of the actual explosion will influence regional transport and deposition of ash. Recent development of a preprocessing tool has allowed for the computation of initial ash fields from source conditions for input into mesoscale atmospheric chemistry models, such as WRF-Chem [*Stuefer et al*., 2013]. Alternatively, volcanic ash transport and dispersion models (VATDMs) calculate initial ash fields directly from eruption source input parameters. In addition, VATDMs consider a full size spectrum of ash and can include nonspherical ash particles. Due to the dangers involved with measuring the size distributions of ash in plumes in situ, the size distributions used in VATDMs are measured from deposits in the field. These measurements are often depleted in fine ash (aerodynamic diameter < 2.5 μm) because fine particles can be swept to great distances from the volcano, where they cannot be collected and measured [*Rose and Chesner*, 1987]. In this study, we use a VATDM, Fall 3D, considering a broad range of ash particle sizes. This model is an open source Eulerian ash dispersion and transport model, which is widely used by the ash forecasting community [e.g., *Folch et al*., 2009; *Costa et al*., 2006].

Recent studies have performed dispersion modeling for selected explosive events from the Mt. Redoubt eruption and compared model output to satellite and field data [*Steensen et al*., 2013*; Mastin et al*., 2013]. Complimentary to these studies, the goal of our study is to quantify the depositional loading fields from the 2009 eruption of Mt. Redoubt. We perform a comprehensive study of the major land-depositing eruptive events and conduct a quantitative error evaluation of modeled deposits. In particular, we investigate the loading fields and spatial/temporal loading gradients for each deposition event along with associated uncertainties. Our approach utilizes the capabilities of the Fall3D model to track transport and deposition of ash, as well as obtain ash deposit loadings, AOD fields within plumes, and areal extents of deposits and plumes. Section 3.2 details the methodology used to produce realistic ranges of model parameters from the literature for the best-studied explosive event in the eruption and extrapolate that information for modeling other events. Section 3.3 presents a validation of modeled ash plume extents and deposit loadings against NASA A-train satellite data and field measurements reported by the AVO. Ash deposit fields for each event, total ash deposit fields for all eruptive events and associated uncertainties, and spatial loading gradients and loading histories are then discussed in Section 3.4. Section 3.5 summarizes the major findings of this work.

3.2 Methodology, Fall3D setup, and data

The most recent eruption of Mt. Redoubt began on 23 March 2009 UTC and lasted through 4 April 2009 UTC. The eruption consisted of 19 explosive events, creating plumes that were carried over both snow covered land and sea surfaces. The explosive volcanic events were all short bursts of ash or “puffs” which were 7 - 38 minutes in duration. These durations are consistent with the interpretation of near vent explosions, which can be triggered by phreato-

magmatic activity [*Scott et al*., 2001]. The formation of meltwater from the interaction of pyroclasts with ice and snow [*Schaefer et al*., 2012] and the exceptionally fine ash sizes observed for the 2009 eruption of Mt. Redoubt [*Wallace et al*., 2013; *Van Eaton et al*., 2012] provides support for phreato-magmatic activity. In this study, we analyze the eruptive events listed in Table 3.1.

Table 3.1: Eruption events, dates, times, durations, plume heights, and mass flow rates (MFRs) used in simulations.

Event number	Date (UTC)	Time (UTC)	Duration (minutes)	plume height (km)	MFR (kg/s)
2	3/23/2009	7:02	7	13.4	2.8×10^6
3	3/23/2009	8:14	20	14.6	4.3×10^6
4	3/23/2009	9:38	38	13.1	2.5×10^6
5	3/23/2009	12:30	20	18.3	1.3×10^7
6	3/24/2009	3:40	15	18.3	1.3×10^7
low-level emissions	4/2/2009	4:00	1200	4.6	1.6×10^3
19	4/4/2009	13:58	31	15.2	5.3×10^6
low-level emissions	4/4/2009	14:29	570	4.9	3.1×10^3

Fall 3D was employed to calculate transport of ash, quantities of ash deposited and areas covered. Events 2 – 6, which occurred on March 23 and 24, produced significant deposits over land only [*Schaefer and Wallace*, 2012; *Schaefer et al*., 2012]. Modeled depositional loadings of these events were corroborated where possible using field data. However, comparison was hampered due to limited field sampling during these events and sparse satellite data, caused by highly reflective snow covered land surfaces and extensive cloud cover. Additional events occurring in early April were selected in order to test that the model can reproduce the areal extents of ash plumes (Table 3.1). These events produced ash plumes over dark ocean surfaces, and the modeled areal extents were verified against satellite data. The April events producing low-level emissions were not classified by *Schaefer et al*. [2012] as major explosions. However,

these events were documented in *Carlile and Nelson* [2009] and observed in satellite data. Of all the events listed in Table 1, event 5 has been the most intensively studied [*Mastin et al*., 2013; *Wallace et al*., 2013; *Steensen et al*., 2013; *Schmehl et al*., 2012]. Given the wealth of information that exists for event 5, it was selected as the baseline for which the best-fit parameters were determined by comparison to field data. All other events employed the best-fit parameters from event 5 for particle shape and size distribution, source type, and diffusion coefficients, but we used event specific times, durations, plume heights and eruption rates (Table 3.1). For each event, model output was verified using the available satellite and/or field data. A schematic of this methodology is displayed in Fig. 3.1.

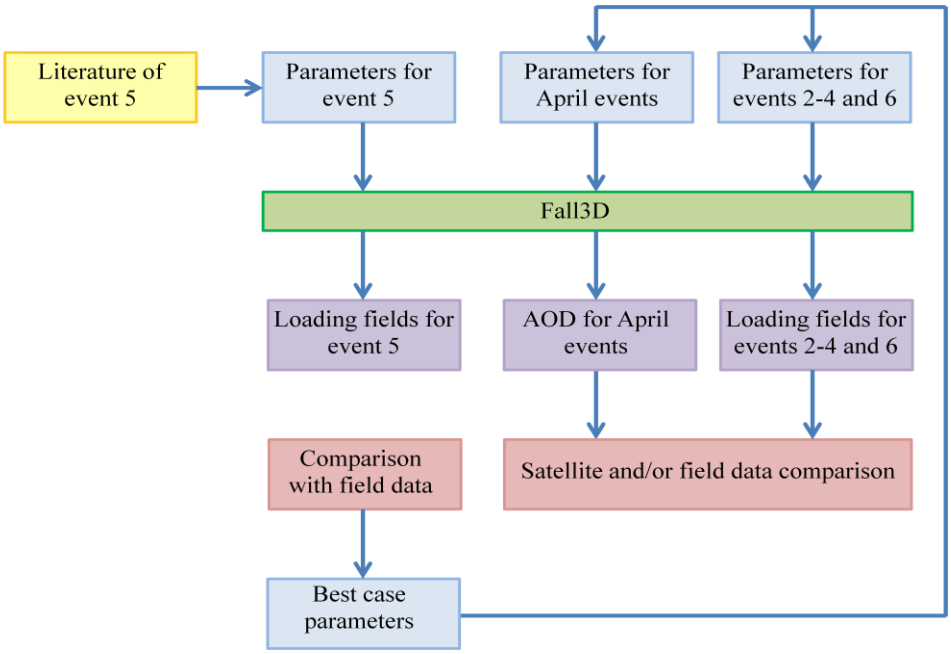

Figure 3.1: A schematic of the methodology used for determining the best-fit case for event 5 and selecting parameters for other eruptions. Literature of event 5 (yellow box) is used to determine event 5 input parameters. Blue boxes denote Fall3D inputs, and purple boxes represent Fall3D output. Satellite and/or field data comparison steps are depicted by red boxes.

3.2.1 The Fall 3D model

Fall3D was used to calculate ash ground loading and to assess the aerial extent of deposits throughout the explosive period of the eruption. The model was also used to determine

the transport of ash plumes in the atmosphere and calculate the AOD of the plumes using modeled concentrations and ash aerosol size distributions. The model calculates the ash concentration in the atmosphere and the ash deposit loadings, considering advection, gravitational settling of particles, and turbulent diffusion according to the continuity equation [*Costa et al*., 2006]:

$$\frac{\partial C}{\partial t} + V_X \frac{\partial C}{\partial X} + V_Y \frac{\partial C}{\partial Y} + \left(V_Z - V_{sj}\right)\frac{\partial C}{\partial Z} =$$

$$-C\nabla \cdot V + C\frac{\partial V_{sj}}{\partial Z} + \frac{\partial}{\partial X}\left(\rho_* K_X \frac{\partial C/\rho_*}{\partial X}\right) + \frac{\partial}{\partial Y}\left(\rho_* K_Y \frac{\partial C/\rho_*}{\partial Y}\right) + \frac{\partial}{\partial Z}\left(\rho_* K_Z \frac{\partial C/\rho_*}{\partial Y}\right) + S_* \qquad (3.1)$$

where C is the scaled average concentration, V = (V_X, V_Y , V_Z) is the scaled average wind speed, K_X, K_Y and K_Z are the diagonal terms of the scaled average eddy diffusivity tensor, ρ_* is the scaled average atmospheric density, and S_* is the scaled average source term. A new reference frame where the coordinate system follows the terrain is defined using scaling factors detailed in *Costa et al*. [2006].

The model requires meteorological data input, which was obtained from *NCEP* Reanalysis data provided by the NOAA/OAR/ESRL PSD, Boulder, Colorado, USA, (http://www.esrl.noaa.gov/psd/). The meteorological data had a horizontal resolution of 210 km with 28 vertical levels, spanning from 0.15 – 30 km [*Kalnay et al*., 1996]. Of the 28 vertical levels, 22 were below 18 km, which is approximately the maximum plume height out of all eruptive events considered here (Table 3.1). More levels were located closer to the sea level to capture interactions in the boundary layer.

The settling model selected for all simulations was the Ganser model [*Ganser*, 1993]:

$$C_d = \frac{24}{R_e K_1}\left\{1 + 0.1118(R_e K_1 K_2)^{0.6567}\right\} + \frac{0.4305\,K_2}{1 + \frac{3305}{R_e K_1 K_2}} \qquad (3.2)$$

where Re is the Reynolds number, C_d is the drag coefficient, and $K_1 = 3/[(d_n/d)+2\psi^{-0.5}]$, $K_2 = 10^{1.8148}(-\mathrm{Log}\psi)^{0.5743}$ are two shape factors (d_n is the average between the minimum and the maximum axis, d is the equal volume sphere, and ψ is the particle sphericity). A typical plume temperature of 1000 K [*Mastin et al*., 2013; *Swanson et al*., 1994] and a constant particle density of 2.5g cm^{-3}, realistic to andesitic ashes [*Schmehl et al*., 2012; *Scott and McGimsey*, 1994], were assumed in all simulations. Although variation in plume temperature between events and thermal heterogeneity in the near source may be expected, sparse data and the small anticipated compositional variation guided our selection of constant thermal source conditions in these simulations. Other input parameters necessary for advection-diffusion models include both source conditions (i.e., mass flow rate (MFR), source type), and material and transport properties (i.e., ash size distribution, sphericity, and diffusion coefficients). These parameters are difficult to determine by in situ measurements. Therefore, we investigated a range of input parameters (described in Sections 3.2.1.1-3.2.1.4 and recorded in Table 3.2) and evaluated best-fit cases.

Table 3.2: Cases selected for event 5 and Δ values.

Run	MFR (kg/s)	Column model	Size distribution	Sphericity	Horizontal diffusion coefficient (m^2/s)	Δ
0	1.3 X 10^7	Point	*Mastin et al*. [2013]	1.0	10,000	0.410
1	1.1 X 10^5	Point	*Mastin et al*. [2013]	1.0	10,000	0.993
2	7.1 X 10^4	Point	*Mastin et al*. [2013]	1.0	10,000	0.995
3	1.3 X 10^7	Suzuki	*Mastin et al*. [2013]	1.0	10,000	0.440
4	1.3 X 10^7	Plume	*Mastin et al*. [2013]	1.0	10,000	0.747
5	1.3 X 10^7	Point	*Rose and Durant* [2009] with fine fraction	1.0	10,000	0.459
6	1.3 X 10^7	Point	*Rose and Durant* [2009]	1.0	10,000	0.485
7	1.3 X 10^7	Point	*Mastin et al*. [2013]	0.7	10,000	0.500
8	1.3 X 10^7	Point	*Mastin et al*. [2013]	0.4	10,000	0.711
9	1.3 X 10^7	Point	*Mastin et al*. [2013]	1.0	10	0.474
10	1.3 X 10^7	Point	*Mastin et al*. [2013]	1.0	100	0.474

Best-fits were determined using a method described in *Scollo et al*. [2008] to quantify the difference between each model simulation and field data, employing the following equation:

$$\Delta = \frac{\sqrt{\frac{1}{N}\sum_{k=1}^{N}(w_{0k} - w_k)^2}}{\sqrt{\frac{1}{N}\sum_{k=1}^{N}(w_{0k})^2}} \quad (3.3)$$

where N is the number of model grid points for which measured loadings were available, and w_{0k} and w_k are the respective values of deposit loading at point k for the measured samples and the model simulation in question. The resulting Δ value is a metric for how closely modeled deposits matched loadings measured in the field. High Δ values represent larger differences in modeled and measured values, and lower values indicate smaller differences. The agreement

between modeled and measured loadings for each simulation is considered good if $\Delta \leq 0.33$, moderate if $0.33 < \Delta \leq 0.66$, poor if $0.66 < \Delta \leq 0.99$, and extremely poor if $\Delta \geq 1$.

3.2.1.1 Mass flow rate (MFR) determinations

A common approach to estimate MFR is to examine plume heights and compare them with heights expected from simple plume theory with a given flux condition [*Wilson et al*., 1978; *Mastin et al*., 2009]. This approach assumes that there is no variation in plume height during the eruptive activity. Errors can occur in measurement of plume height, or when the eruptive behavior deviates from assumptions. Another widely used method is to use erupted masses determined from mapped out deposits [*Wallace et al*., 2013; *Mastin et al*., 2013], assuming MFR does not change for the duration of the eruption. This method requires that the regions of deposited ash be well-characterized, adequately sampled, and measured as quickly as possible after the eruptive event. Care must be taken to collect ash only from the event of interest, and eruption durations must be accurate. The fine ash fraction will likely be carried much farther than other deposits, making it difficult to include in these measurements [*Rose and Chesner*, 1987; *Rose et al*., 2008].

From the Redoubt 2009 eruption, there are not many estimates of MFR, with the exception of event 5 (Table 3.1). *Mastin et al*. [2013] uses a MFR of 3.7×10^6 kg s^{-1} calculated from the deposits for event 5 from *Wallace et al*. [2013] and for a seismic duration of 20 minutes. One of the challenges in any MFR estimation is that this rate is normally assumed to be constant. *Mastin et al*. [2013] reports that MFR for event 5 was likely variable and that most of the mass was likely erupted in the first 10 minutes of the eruption. Therefore, *Mastin et al*. [2013] adjusted MFR to 7.3×10^6 kg s^{-1} for a 10 minute eruption duration. However, *Mastin et al*. [2013] found that a MFR of 1.3×10^7 kgs^{-1} produces plumes that more closely match the

heights reported in radar observations. In a different approach, *Schmehl et al*. [2012] uses a genetic algorithm to arrive at a solution that minimizes the errors between observed and modeled variable values. *Schmehl et al*. [2012] reports a predicted MFR for event 5 of 1.1 X 10^5 ± 1.2 X 10^5 kg s^{-1}, with the best-fit simulation having a MFR of 7.1 X 10^4 kgs^{-1}, assuming constant emissions. These values are considerably different than those reported from the *Mastin et al*. [2013] study. Here, the MFR were systematically varied to find the best-case scenario. We found that using an MFR of 1.3 X 10^7 kgs^{-1}, as in *Mastin et al*. [2013], over a duration of 20 minutes produced the most realistic deposit loadings as compared to field data. This is unsurprising, given the similar approach between *Mastin et al*. [2013] and this work.

Event 5 was used as a reference event to evaluate the MFR for the other events listed in Table 3.1. For other events, the MFR was computed using the following relationship between MFR and plume height (H), derived from [*Wilson and Walker*, 1987]:

$$MFR = MFR_{Event\ 5}\left(\frac{H}{H_{Event\ 5}}\right)^4 \quad (3.4)$$

where $MFR_{Event\ 5}$ is the MFR for event 5, $H_{Event\ 5}$ is the plume height for event 5, and H and MFR are the respective plume heights and MFR values for the event in question. Plume heights for explosive events were taken from *Schaefer et al*. [2012], which were derived from the Federal Aviation Administration Next Generation Weather Radar (FAA NEXRAD) and/or USGS radar. Low-level emission plume heights were taken from pilot reports in *Carlile and Nelson* [2009]. Plume heights used in equation 3.4 are heights above the vent, which is located at 3 km above sea level.

3.2.1.2 Initial ash size distribution and sphericity

We considered three size distributions in order to investigate a range of size distributions that would be realistic for the Redoubt eruption. There have been few in situ

measurements of size distribution of volcanic ash plumes, mainly due to the dangers involved in making this measurement. Therefore, all size distributions used in this study were measured on ash fall samples. These values are not truly representative of the ash size distribution in the atmosphere due to sorting which occurs during transport and underrepresentation of the fine ash fraction [*Rose and Durant*, 2009]. Ground measurements from *Durant and Rose* [2009] produced one of the size distributions used in our study (Fig. 3.2).

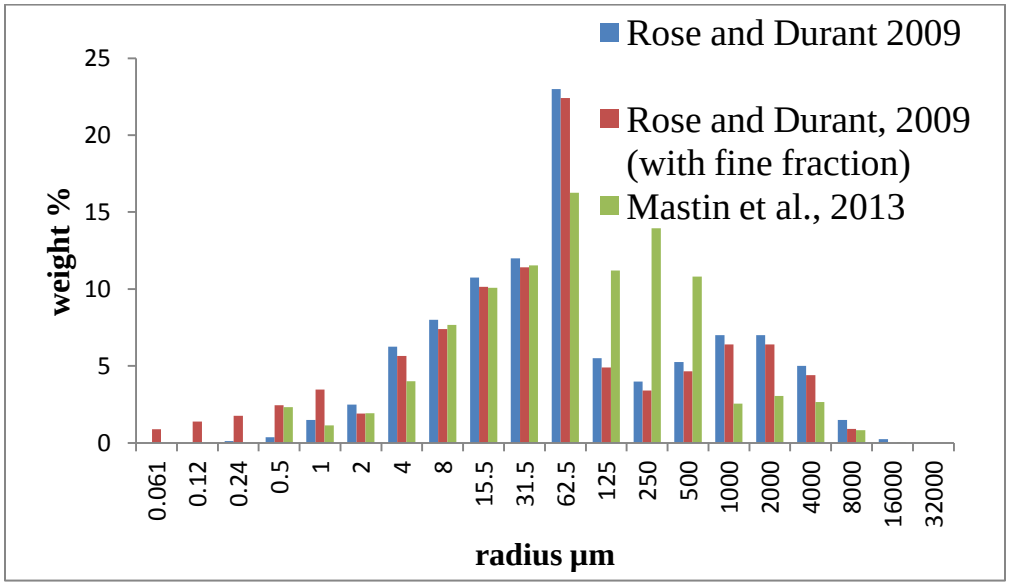

Figure 3.2: Size distributions selected for Fall3D simulations.

This measurement was done for the 1992 eruption of Mt. Spurr, which has similar source conditions, eruptive size, and composition as Redoubt [*Steensen et al*., 2013; *Mastin et al*., 2009].

In addition, we used two other size distributions that attempt to represent the fine fraction present in the atmosphere. The first was introduced to reconstruct a fine fraction for the deposits measured by *Durant and Rose* [2009]. This was done by assessing MODIS fine mode fractions (aerodynamic diameter < 2.5 µm) around the vent throughout the period of explosivity.

The lowest fine fraction determined was about 10%. This was taken to be an upper bound on the initial fine mode fraction, as this value was not from directly over the vent. Sulfate aerosol fractions, which would also be included in the fine mode fraction, were assumed to be negligible for the beginning of the eruption. This fine fraction was subtracted uniformly from fractions for coarser particles in *Durant and Rose* [2009] and was added uniformly to fine bins, creating a fine mode making up 10% of the total distribution (Fig. 3.2). The last size distribution was reported for the 2009 Redoubt eruption in *Mastin et al*. [2013] (Fig. 3.2).

Particle size and shape affect the settling rate of ash. For each particle size class, the sedimentation equation is solved for the size and shape associated with that class. The Ganser settling model allows calculating the settling behavior nonspherical particles. Due to the highly variable fragmentation processes in magma, particles can vary greatly in shape, ranging from spherical particles to nonsphericities as low as 0.4 [*Bonadonna et al*., 2011; *Alfano et al*., 2011]. In this study, we consider a sphere (sphericity = 1) and nonsphericities of 0.7 and 0.4, in order to cover the full range of sphericities for volcanic ash particles reported in the literature. The nonsphericity is assumed to be uniform across all sizes, because past studies have not found a significant correlation between particle size and shape [*Bonadonna et al*., 2011; *Alfano et al*., 2011].

3.2.1.3 Source type

The source type was varied for three different column models: plume, point, and Suzuki. The plume source represents ash that is propelled into the atmosphere at first by the momentum resulting from rapidly depressurized material. Higher in the atmosphere, ash is lifted by the buoyancy of a hot plume rising until it reaches a point of neutral buoyancy with the atmosphere [*Ernst et al*., 1996]. The height of neutral buoyancy is computed from the MFR, velocity and gas

fraction. The MFR was taken from the literature, as further described in Section 2.1.1 (Table 3.1). Velocity (v), particle volume fraction(ε_p), and gas mass fraction (X) were computed from the following system of equations, assuming choked flow conditions at the vent [*Papale and Dobran*, 1994], where v = the speed of sound (c):

$$\varepsilon_p = \frac{MFR}{A_{vent} * \rho_p * v} \tag{3.5}$$

$$X = \left[1 + \left(\frac{\frac{\varepsilon_p}{\rho_p}}{(1-\varepsilon_p)\rho_g}\right)\right] \tag{3.6}$$

$$v = c = \sqrt{\frac{RT}{X}}\left[X + \left(\frac{\rho_g}{\rho_p}\right)(1-X)\right] \tag{3.7}$$

where A_{vent} is the area of the volcanic vent, ρ_p is the particle density, T is the plume temperature, R is the specific gas constant, and ρ_g is the density of the gas calculated from the ideal gas law, assuming water vapor is the only gas. For MFR = 1.3 X 10^7 kgs^{-1}, v ~ 530 ms^{-1}, ε_p ~ 0.055%, and X ~ 61%. The area of the vent was estimated from Google Earth images as ~ 18,000 m^2, and uncertainties in this estimate exist in locating the exact bounds of the eruption crater from the satellite imagery.

The point source disperses all ash from one height in the atmosphere. The Suzuki source disperses ash according to the following equation [*Pfeiffer et al*., 2005]:

$$S(x,y,z,t) = S_0\{1 - \frac{z}{H}\exp\left[A(\frac{z}{H} - 1)\right]\}^{\lambda} \times \delta(t - t_0)\delta(x - x_0)\delta(y - y_0) \tag{3.8}$$

where $S(z) = \{1 - z/H \exp[A(z/H - 1)]\}^{\lambda}$ is the vertical mass distribution function, z is the column altitude, S_0 is a normalization factor, H is the maximum plume height, A and λ are two dimensionless parameters, and δ is the Dirac's distribution for filiform and instantaneous release. The parameter A is the Suzuki coefficient, which describes the vertical position of the maximum concentration relative to the maximum column height, located at (A - 1)/A of the maximum

plume height. Smaller values of A represent plumes with ash distributed more equally at all heights, whereas larger values of A indicate that the area of highest ash concentration occurs closer to the maximum plume height, as in stronger volcanic eruptions. The parameter λ is a measure of how closely the total mass is concentrated around the maximum at H(A - 1)/A. Values of A and λ were systematically varied, as in *Pfeiffer et al*. [2005], to obtain a combination that produced the best agreement with field data. Because the event 5 eruption was strong, a relatively large A of 10 produced the better fit, and a value of λ of 3 was selected. In this study, we do not explicitly consider the impact of wind shear and bent over plume entrainment due to lack of constraints, although we note that the enhanced entrainment due to near vent winds may alter the deposition patterns, particular near to the volcanic summit [*Degruyter and Bonadonna*, 2012].

3.2.1.4 Diffusion coefficients

Diffusion coefficients represent the dispersion of ash due to small-scale turbulent motion without directly modeling the scale of this flow [*Bonadonna et al*., 2005; *Costa et al*., 2006]. The process occurs as particles move in a random walk from areas of high to low particle concentration. The diffusion coefficients set the width of ash plumes and deposits. Values of diffusion coefficients used in ash dispersal models vary widely and are difficult to constrain [e.g., *Scollo et al*., 2011]. Therefore, diffusion coefficients are often adjusted to produce results that agree with observations and in this way also account for some of the turbulent processes not directly resolved in the model. In large eruptive columns, most of the transport processes occur outside the boundary layer, where the vertical diffusion coefficient is small [*Pasquill*, 1974]. Therefore, the vertical diffusion coefficient will be negligible compared to the horizontal diffusion coefficient [*Macedonio et al*., 2008], and we set the vertical diffusion coefficient equal

to zero for all cases, as recommended by *Bonadonna et al*. [2005]. A horizontal diffusion coefficient ($K_x = K_y$) was varied from 10 m^2 s^{-1} to 10000 m^2 s^{-1}, which is within a range of horizontal diffusion coefficient values used for eruptions of this scale [*Pasquill* 1974; *Bonadonna et al*., 2005; *Scollo et al*., 2011].

3.2.3. Satellite and field data

We used several datasets from MODIS and OMI satellite sensors and field measurements to compare to model results. The MODIS level 2 Collection 5 AODs at 550 nm and true color images were used to compare to the areal extent and transport of modeled volcanic plumes during early April. True color images of ash deposits, when available, were also used to aid in validation of modeled deposition areas for eruptions on March 23 and 24. In addition, we used MODIS AODs to perform a comparison with modeled ash AODs at 500 nm. The MODIS lookup table for aerosol retrievals over ocean contains an effective radius (r_{eff}) range of 0.10 – 2.50 μm. This range does not include r_{eff} above 2.50 μm, because it could be misclassified as a cirrus cloud or ice [*Levy et al*., 2003]. The model contains a wider range of r_{eff} values in AOD calculations, which range from 0.014 – 10 μm. Both volcanic ash and sulfate aerosol are included in the MODIS AOD signal. In order to estimate the AOD due to ash and to eliminate any signals due to sulfate, a coarse mode AOD was calculated by multiplying the total MODIS AOD by the MODIS fine mode fraction and subtracting this value from the total AOD. This was done to make MODIS and modeled AODs more comparable, but it is noted that eruptive plumes can contain large portions of fine ash [*Rose and Durant*, 2009].

The OMI instrument has an ultraviolet – visible spectral range of 0.27-0.50 μm and provides the UV AI [*Torres et al*., 2007]. The AI is a semi-quantitative indicator of the

presence of UV-absorbing aerosols, such as volcanic ash, smoke, and dust. We used OMI AIs to verify aerial extent and transport of plumes during early April. The MODIS and OMI instruments both have difficulties in retrieving aerosol and surface information in the presence of meteorological clouds or over highly reflective surfaces, both of which are common environmental conditions during early spring in the Arctic. Therefore, satellite retrievals for this eruption were challenging.

Ash deposition loadings for events on March 23 and 24 were compared to loadings measured in the field by *Shaefer et al*. [2011] and *Wallace et al*. [2013]. In these studies, samples were collected at 189 field stations between March 18 and July 11, 2009. Particle size analyses of samples were performed at the USGS Cascades Volcano Observatory (CVO) Sediment Laboratory using sieve and SediGraph techniques [*Wallace et al*., 2013]. Ashes from events 5 and 6 were measured and characterized individually, but ashes from events 2-4 were measured collectively. The authors report difficulties in distinguishing between ash layers from different events in some cases, as well as difficulty in sampling at farther locations from the volcano, leading to sparser sampling coverage in these areas.

3.3 Investigation of model performance

We first present our Δ values and selection of best case conditions, followed by a satellite validation of modeled plume areal extents in order to show the capability of the model to reproduce areal extents of ash deposits. Deposition fields of cumulative ash deposits are then presented for eruptive events 2-6. Uncertainties in modeled ash deposition fields and the spatial/temporal gradients in ash deposits are discussed.

3.3.1 Examination of Δ values and selection of best-fit case

The best-fit case for event 5 (Run 0, Table 3.2) showed moderate agreement with field data (Δ = 0.410). This best-fit case was the result of 200 simulations that were used to constrain best-fit input parameters. Run 0 used a point source with a MFR of 1.3 X 10^7 kgs^{-1} over a 20 minute eruption duration, the size distribution from *Mastin et al*. [2013] with spherical ash particles, and a horizontal diffusion coefficient of 10,000 m^2s^{-1}. As a first check of the feasibility of event 5 simulated deposits, modeled total volumes were compared to those estimated by *Wallace et al*. [2013] from measured deposits, which were ~1.7 X 10^6 m^3. In this calculation, *Wallace et al*. [2013] employed the root-area method of *Pyle* [1989] and *Fierstein and Nathenson* [1992] to account for the mass of ash fall beyond the most distal isomass contour. For run 0, the total deposited volume was ~ 2.9 X 10^6 m^3, which was on the same order of magnitude as total volume estimated by *Wallace et al*. [2013]. We performed this calculation by dividing the total mass of deposits at the end of the simulation by the density of ash.

In each subsequent simulation, only one parameter in Table 3.2 is varied at a time in order to determine how sensitive modeled loadings are to each parameter. For each simulation, moderate agreement to field data similar to the best case simulation show that the modeled loadings were not very sensitive to the parameter that was varied. Poor agreement indicates that the parameter in question produced widely different modeled loadings from those measured in the field, and that modeled loadings were sensitive to the parameter and the range over which it was varied. Run 3 gave a similar Δ value (Δ = 0.440) for using a Suzuki source instead of a point source, indicating that the Suzuki source used in our simulations distributed ash in a similar way to the point source. Our Suzuki simulations used a large A value, which placed the largest concentration of ash near the maximum plume height. In this way, the Suzuki source with a large

A value is similar to a point source, which releases all ash at a single point at the maximum height. Runs 9 ($\Delta = 0.474$) and 10 ($\Delta = 0.474$) also produced moderate Δ values for horizontal diffusion coefficients, which were varied by several orders of magnitude from that used in the best case simulation. This suggests that changes in horizontal diffusion coefficient do not greatly affect modeled loadings, which is consistent with other parametric studies [e.g., *Courtland et al.*, 2012]. The different size distributions in runs 5 ($\Delta = 0.459$) and 6 ($\Delta = 0.485$) show moderate agreement with field data as well, with the simulation containing more fine classes performing slightly better.

Varying ash particle nonsphericity (runs 7 and 8) produced moderate agreement for a nonsphericity of 0.7 ($\Delta = 0.500$) but had poor agreement with field data for nonsphericity of 0.4 ($\Delta = 0.711$). Poor agreement was also observed in run 4, which used a plume source ($\Delta = 0.747$), and runs 1 ($\Delta = 0.993$) and 2 ($\Delta = 0.995$) in which MFR was varied. The poor agreement of runs 1, 2, and 4 indicates that the values of parameters varied in these simulations were not realistic to the eruption.

3.3.2 Validation of modeled areal extent of ash plumes

The eruptions on April 2 and 4 provide for MODIS retrievals of areal plume extent and AOD, because the optically bright volcanic plumes passed over the dark ocean surface of the Gulf of Alaska. The eruption on April 2 was not a violent event, but produced continuous low-level ash emissions for several hours on that day (Table 3.1). The OMI reveals the presence of UV-absorbing aerosols in the region east to southeast of the volcano (Fig. 3.3a).

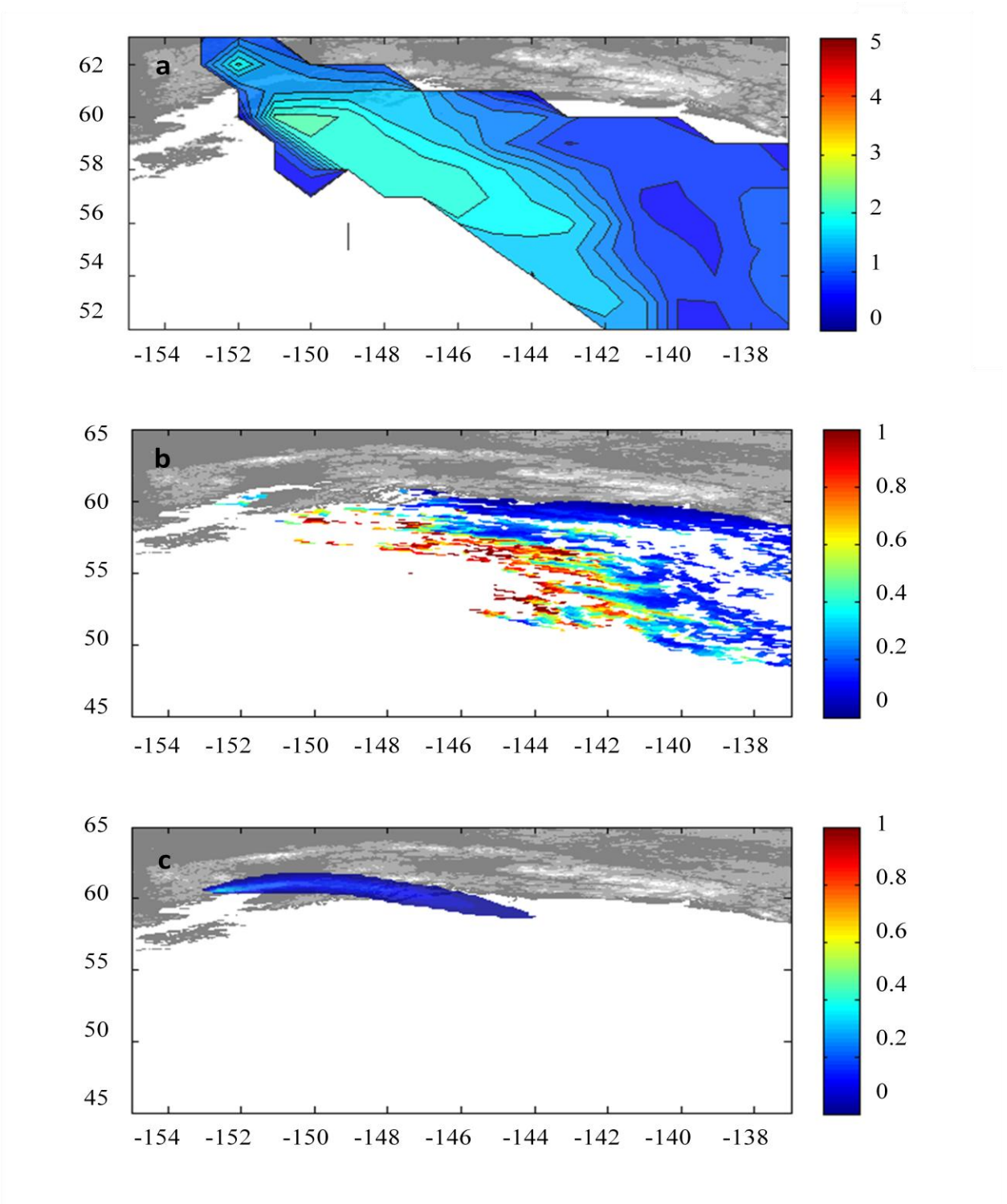

Figure 3.3: (a) OMI AI on April 2 showing UV absorbing aerosol moving southeast of Mt. Redoubt. (b) Terra MODIS coarse AOD at 550 nm on April 2 at 20:55 UTC. Coarse aerosol is located from about 45°N to 60°N east to southeast of the volcano. (c) Modeled ash AOD at 500 nm from low-level emissions on April 2 at 21:00 UTC. Ash is located roughly above 58°N and is moving east of the volcano.

Retrievals of Terra MODIS coarse AOD at 20:55 UTC also show an aerosol plume located east to southeast from the volcano (Fig. 3.3b). The MODIS coarse AOD within this plume ranged from 0.01 - 1.30, and the mean was 0.3. The model predicted a plume positioned more east of the volcano, with less of a southerly component in the trajectory (Fig. 3.3c). Modeled AODs ranged from 0.01 - 0.52, with a mean of 0.08. Discrepancies in plume location and extent can be attributed to problems with resolution of wind fields. A horizontal resolution of 210 km was likely too large to capture smaller scale dynamics of ash transported through areas of rugged mountain terrain. If volcanic ash is only present roughly above 58^{o}N in the MODIS image, as is the case for the modeled AODs, the range of coarse mode AOD in this region of the plume is 0.01 – 1.1, with an average of 0.1, which agrees better with the model.

On April 4, there was a large, discrete explosion at 13:58 UTC (event 19), followed by low-level ash emissions throughout the remainder of the day [*Carlile and Nelson*, 2009; Table 3.1]. Elevated values of OMI AI indicate that UV-absorbing aerosols are present southeast of the volcano, over the Gulf of Alaska, and east to northeast of the volcano, over Alaska (Fig. 3.4a).

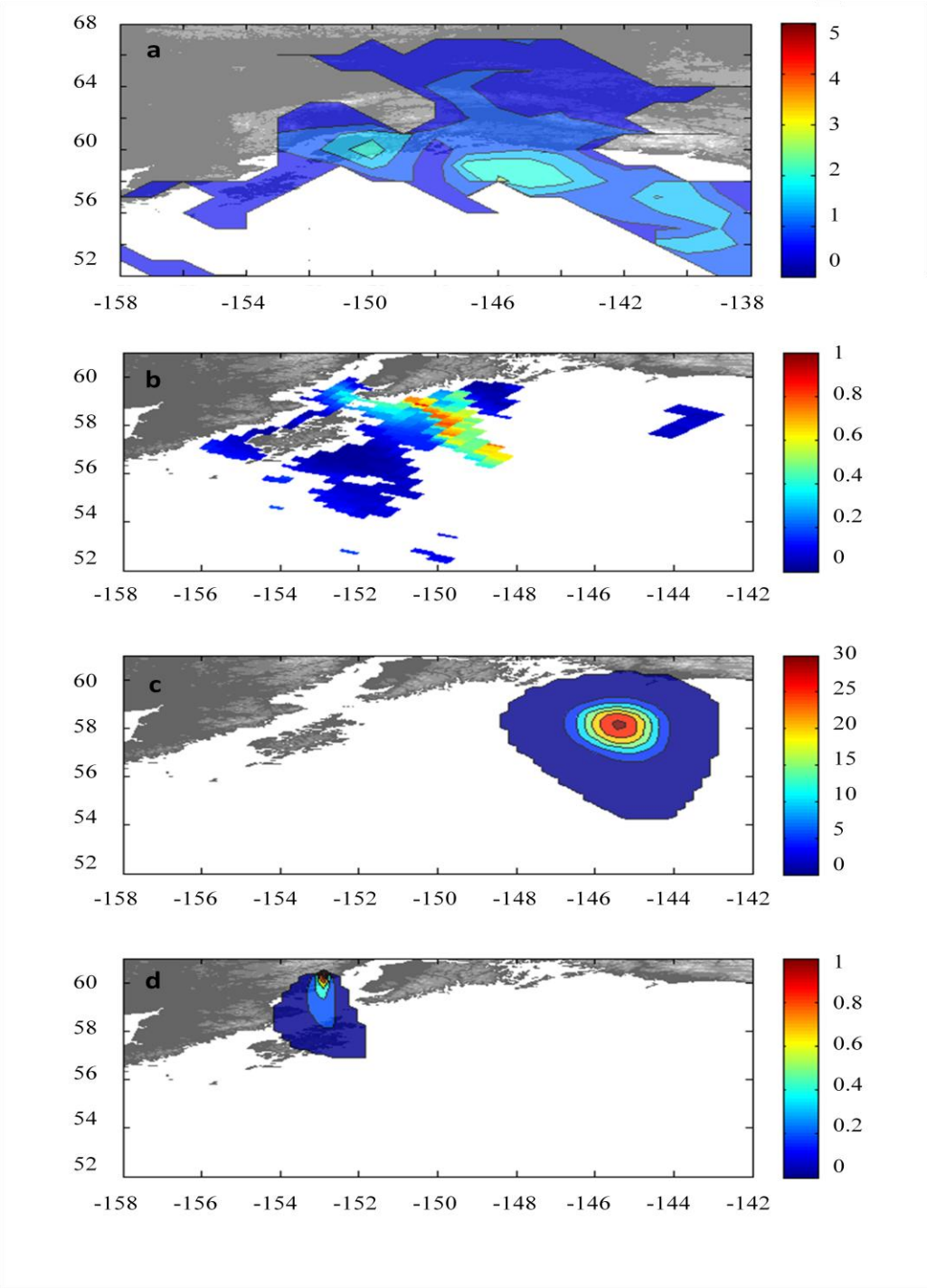

Figure 3.4: (a) OMI AI on April 4 showing UV absorbing aerosol traveling southeast of Mt. Redoubt. (b) Terra MODIS coarse AOD at 550 nm on April 4 at 22:20 UTC. Coarse aerosol is located southeast of the volcano. (c) Modeled ash AOD at 500 nm from event 19 at 22:00 UTC. An optically thick ash plume is shown east to southeast of the volcano, further away than plumes detected by MODIS and OMI. (d) Modeled ash AOD at 500 nm from low-level emissions on April 4 at 22:00 UTC, which displays an ash plume with about the same optical thickness as the MODIS image and in a similar location to plumes in both MODIS and OMI images.

Coarse AOD retrieved from Terra MODIS at 2220 UTC shows coarse aerosol southeast of the volcano, having AODs ranging from 0.02 - 0.86 and a mean of 0.19 (Fig. 3.4b). Modeled AODs of event 19 revealed an extremely optically thick plume with maximum AODs in the 30s, which had moved far to the east of the aerosol detected by MODIS at 2220 UTC (Fig. 3.4c). Meteorological clouds, which are typically not thicker than a few kilometers, can also have high optical depths which are comparable to, and can even exceed, those modeled for the 13:58 UTC eruption [*Hahn et al*., 2001]. Therefore, it is reasonable that a freshly erupted volcanic plume with a thickness of several kilometers would have large AODs similar to meteorological clouds. However, because of the placement of the plume at 22:20 UTC and the much higher AODs compared to MODIS AODs, we believe the aerosol observed in the MODIS image was produced by the low-level emissions which occurred after event 19. Modeled AODs from the low-level emissions ranged from 0.01 – 1.38, with an average of 0.13, and produced a plume in a similar location to the aerosol detected by MODIS at 2220 UTC (Fig. 3.4d). The general agreement between plumes detected by satellites and modeled plumes is a good indication that the model is capable of reproducing the areal extent of ash deposits from this eruption.

3.4 Assessment of areal extent and amount of deposited ash

3.4.1 Modeled deposit loading fields and associated uncertainties

For events 2-4, the total area of the deposited ash was 2.7 X 10^6 km^2, which was quantified by multiplying the area of one pixel in the model by the number of pixels with ash loadings greater than 0 gm^{-2} at the end of the simulations. Loadings ranged from ~3000 gm^{-2} near the vent to < 0.1 gm^{-2} in the northern-most deposits, with trace amounts falling near Fairbanks, ~ 550 km north-northwest of Mt. Redoubt (Fig. 3.5).

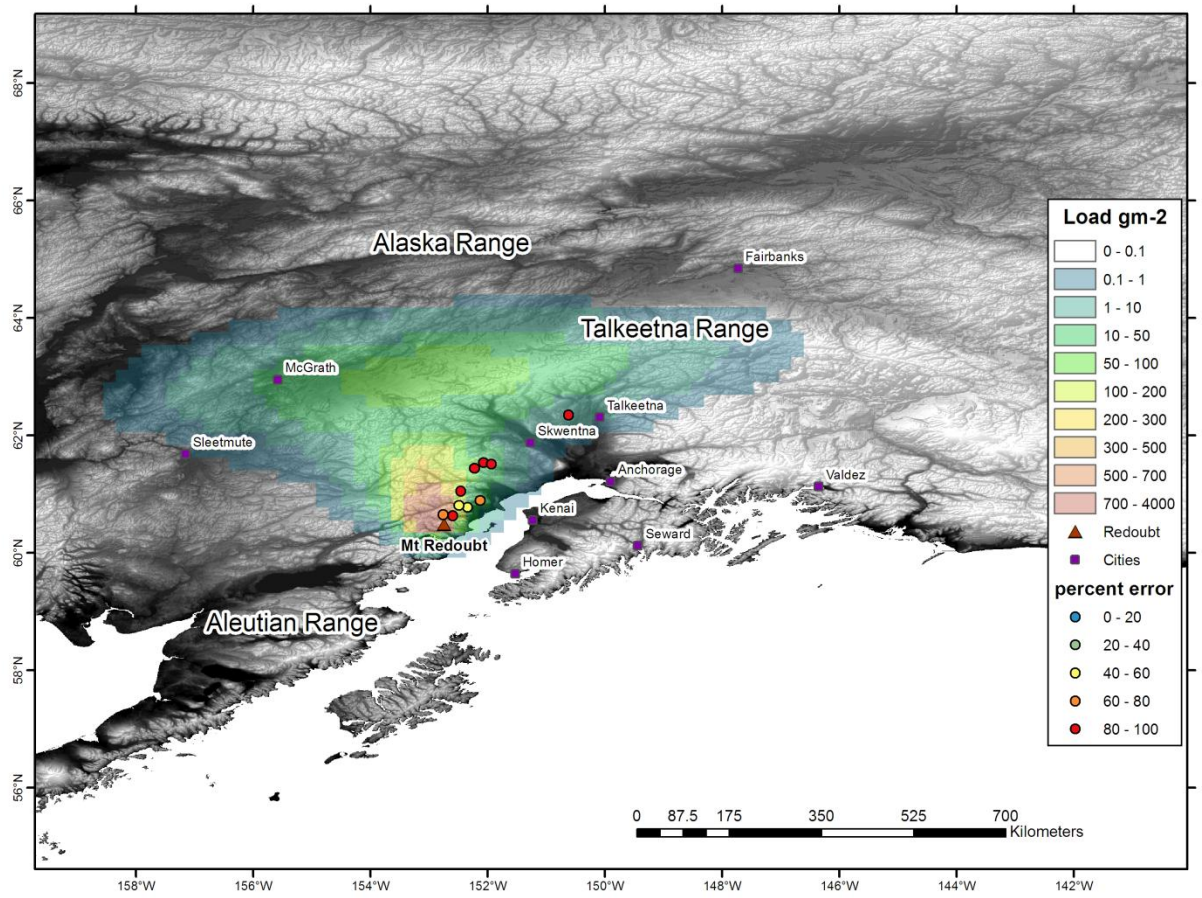

Figure 3.5: Events 2-4 run 0 summed loadings in gm^{-2}. Mt. Redoubt is marked by a brown triangle. Alaskan cities are denoted by purple squares. The circles are field sampling locations from *Schaefer and Wallace* [2012], and colors represent the associated percent error between modeled and measured values at those locations.

Lower levels of loading may occur over a wider region but were not resolved [*Bonadonna et al.*, 2011]. Ash was deposited in both the Alaska and Talkeetna Mountain Ranges. Deposits covered the towns of Skwentna, Talkeetna and McGrath, and the western edge of deposits reached to Sleetmute, ~ 270 km northwest of the volcano. A secondary maximum in ash loading is observed north of the volcano near McGrath and occurs where loading values increase again to ~ 50 – 100 gm^{-2}. There are no sampling sites located in this region, so it is difficult to determine if this is a true feature of the deposits. Secondary maxima are often attributed to the ash aggregation, or the

adhesion and coalescence of ash particles through hydrodynamic or electrostatic forces [Carey *and Sigurdsson*, 1982; *Telling et al*., 2013]. However, no aggregation processes were considered in the model. Here, the secondary maximum could be an artifact potentially caused by the size bins used in the initial size distribution. *Mastin et al*. [2013] found that the secondary maximum in event 5 modeled deposits disappeared upon dividing the initial size distribution into more size bins. However, if the secondary maximum was an artifact due to size binning, it might be expected to appear in deposit loadings for other eruptions, but it does not.

Event 5 deposits covered a total area of 2.2×10^6 km^2, and loadings ranged from ~ 4000 gm^{-2} near the vent, to ~0.1 gm^{-2} in the Alaska Mountain Range (Fig. 3.6).

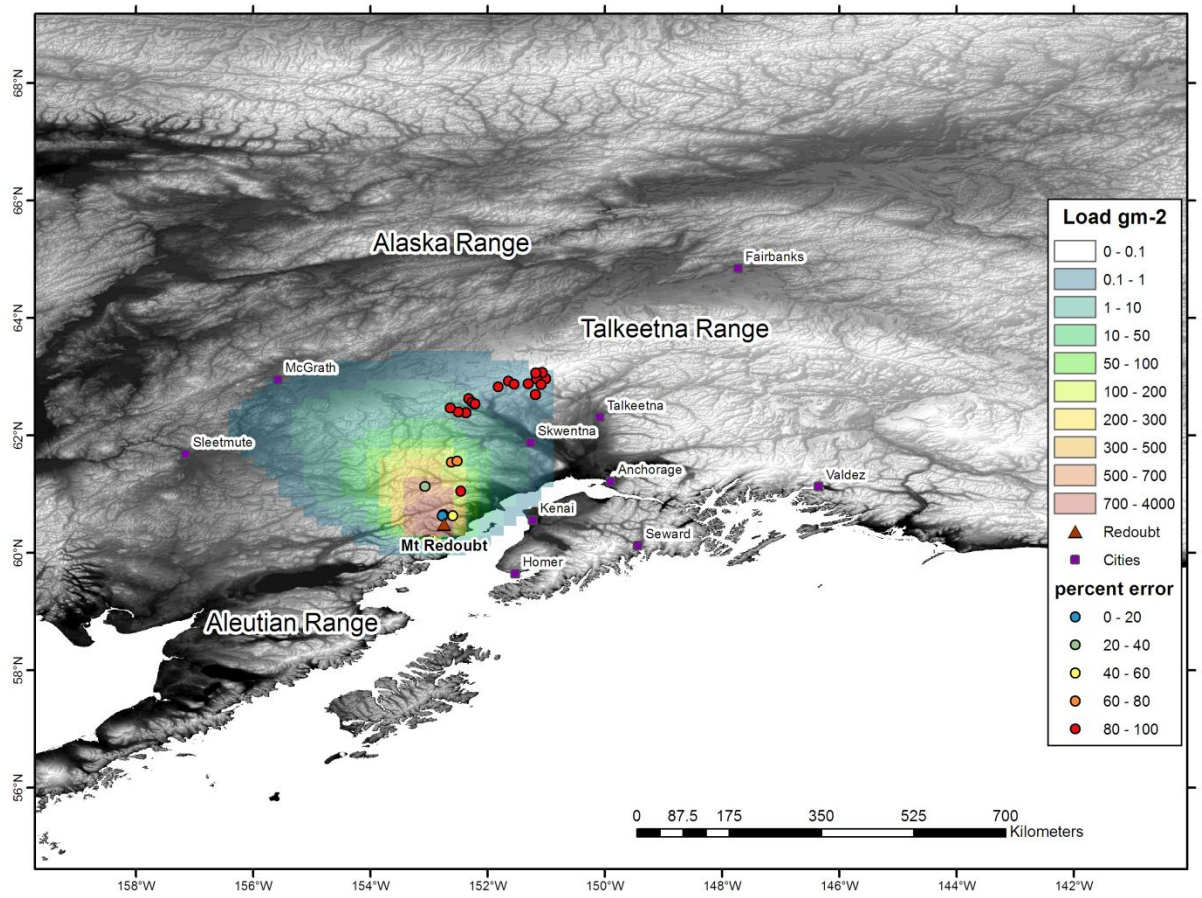

Figure 3.6: Event 5 run 0 loadings in gm^{-2}. Mt. Redoubt is marked by a brown triangle. Alaskan cities are denoted by purple squares. The circles are field sampling locations from *Schaefer and Wallace* [2012], and colors represent the associated percent error between modeled and measured values at those locations.

Deposits reached Skwentna (~ 180 km northeast of the volcano) and reached McGrath (~ 310 km north-northwest of the volcano). Although event 5 was the best sampled event, it is still not sufficiently sampled to discern the entire extent of the deposits from these points.

The total area of deposits from event 6 was 3.4 X 10^6 km^2, with loadings ranging from ~3000 gm^{-2} near the source to <0.1 gm^{-2} at the furthest extents of the deposits (Fig. 3.7).

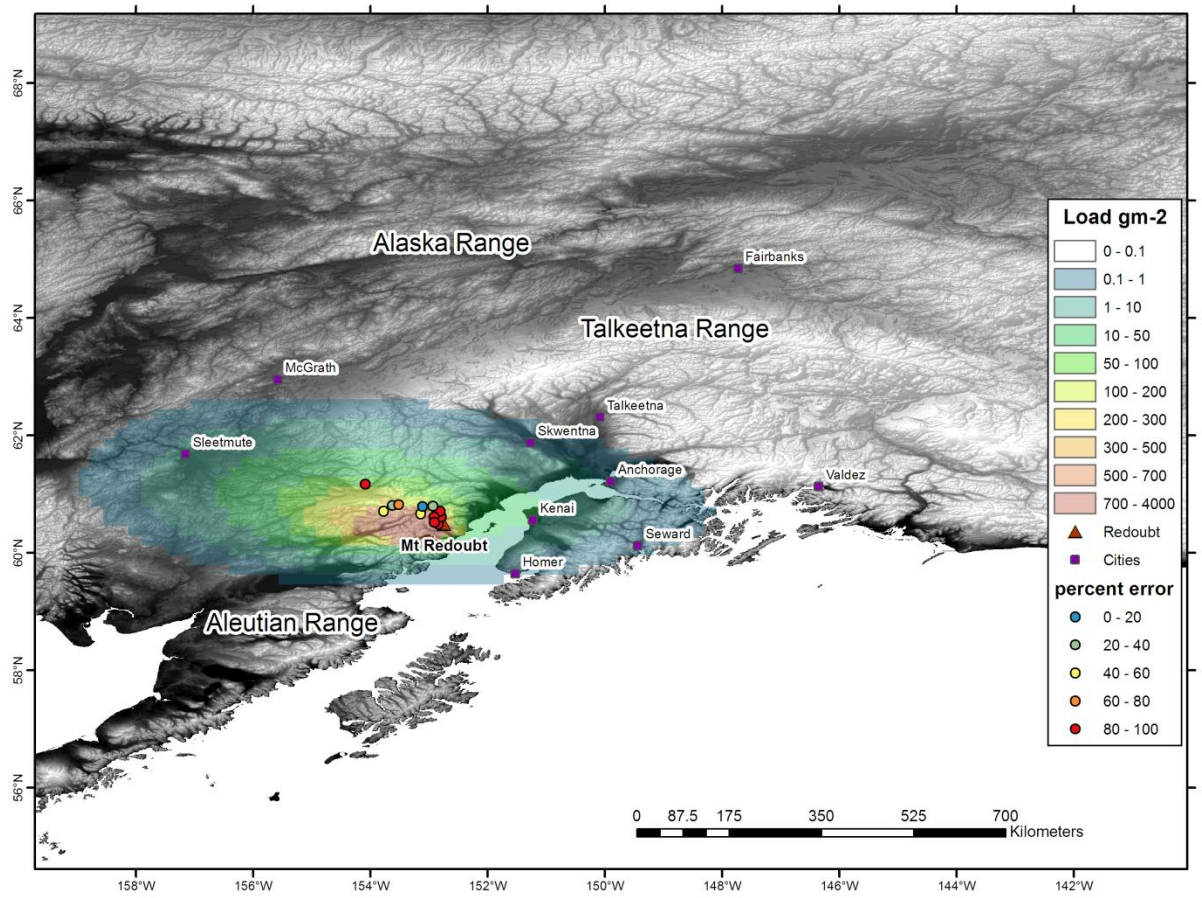

Figure 3.7: Event 6 run 0 loadings in gm^{-2}. Mt. Redoubt is marked by a brown triangle. Alaskan cities are denoted by purple squares. The circles are field sampling locations from *Schaefer and Wallace* [2012], and colors represent the associated percent error between modeled and measured values at those locations.

Deposits covered the cities of Homer, Kenai, Anchorage, and Skwentna, and the southeastern most deposits reached Seward (~190 km away). The northwestern deposits covered Sleetmute. Fig. 3.8 displays a MODIS true color image of the north to north-northwestern deposits, which agrees with the modeled extents for these deposits. The image is obscured by clouds so that the farthest extents in other directions cannot be seen.

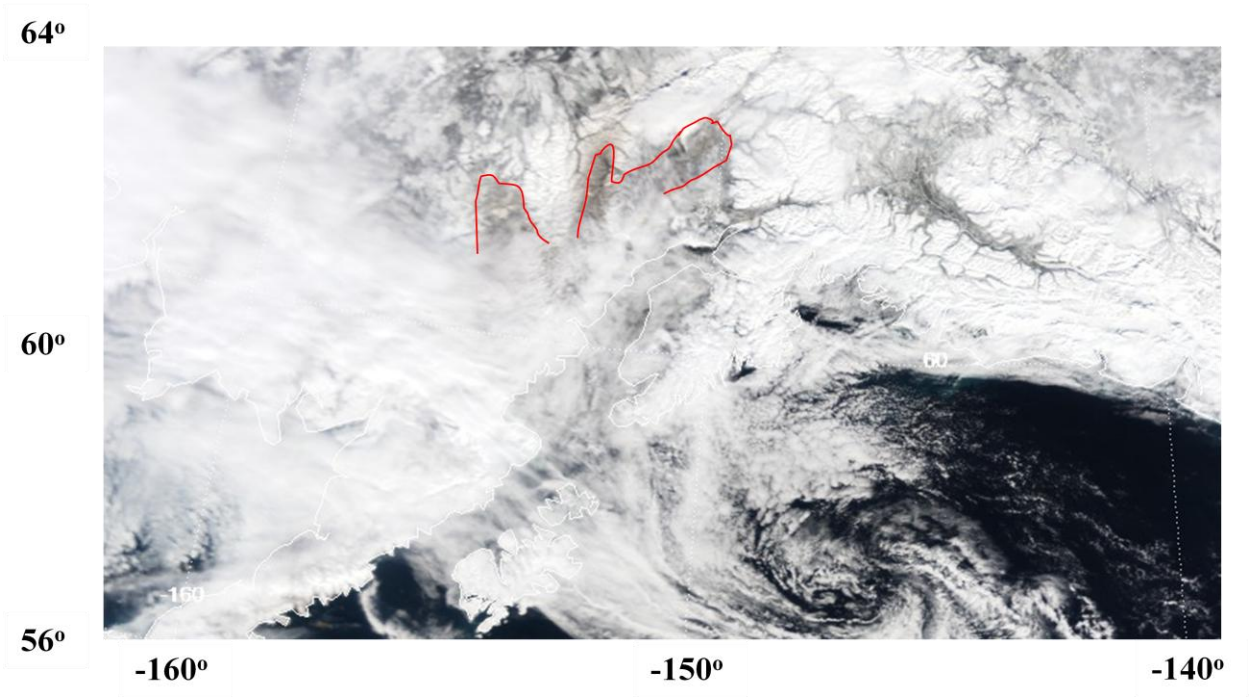

Figure 3.8: MODIS Terra true color image on March 24 at 21:00 UTC. Ash deposits are outlined in red.

Uncertainties in modeled deposit loadings were assessed in order to bracket a realistic range of total cumulative loadings. Percent errors between samples measured from each site and modeled data at that location are presented for each eruption in Fig. 5 – 7. For events 2 – 4 and 6, percent errors were overall higher than those for event 5 because much of the information needed to model these events was unavailable and therefore derived from the event 5 best-fit case. In general, the simulations have difficulty reproducing loadings for sample points located farther from the vent, as in event 5 (Fig. 3.6). *Schaefer and Wallace* [2012] reported that loadings at the northern most sampling points for event 5 were ~10 gm^{-2}, an order of magnitude lower than our modeled values. *Mastin et al.* [2013] and *Steensen et al*. [2013] both employed Eulerian models, Ash3d and WRF-Chem, and used similar model setups to simulate event 5. *Mastin et al*. [2013] and *Steensen et al*. [2013] had similar difficulty with reproducing sufficient loadings at points located furthest from the volcano for many simulations. In all studies, model disagreement with

observations could be due to field measurement errors, resulting from difficulties in separating ash from different events [*Schaefer et al*., 2012; *Wallace et al*., 2013], ash aggregation effects not accounted for in the models, or problems with wind field resolution through areas of higher elevation. Wind fields may also have not been resolved enough to capture small scale motion between sample points, as the points located furthest from the vent were only ~300 km away and the horizontal resolution was 210 km.

An examination of Δ values with distance from the volcano for event 5 showed that run 0 is the best case simulation for points near the vent, 16 – 18 km away (Fig. 9).

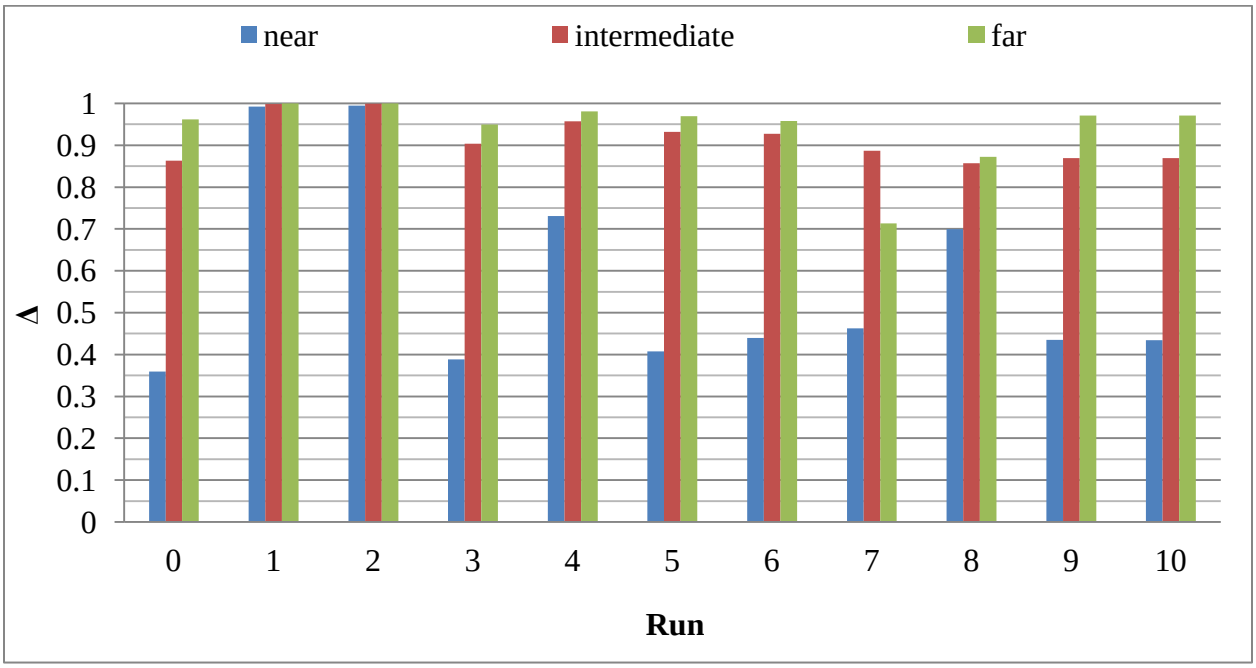

Figure 3.9: Event 5 simulations with three part Δs: near vent region (60.65 N to 60.63 N and 152.60 W to -152.76 W, 16 km – 18 km from the volcano), intermediate region (61.05 N to 61.56 N and -152.46 W to -153.07 W, 61 km - 120 km), and far region (62.39 N to 63.07 N and -150.32 W to -152.64 W, 212 – 300 km).

However, run 7 (with nonsphericity = 0.7) yields a much better agreement with samples measured far (210 – 300 km) from the volcano. Therefore, total loadings for events 2 - 6 for runs 0 and 7 were averaged. The standard deviation was computed in order to produce a realistic

range of loading values, based on uncertainties existing between modeled and field data (Fig. 3.10).

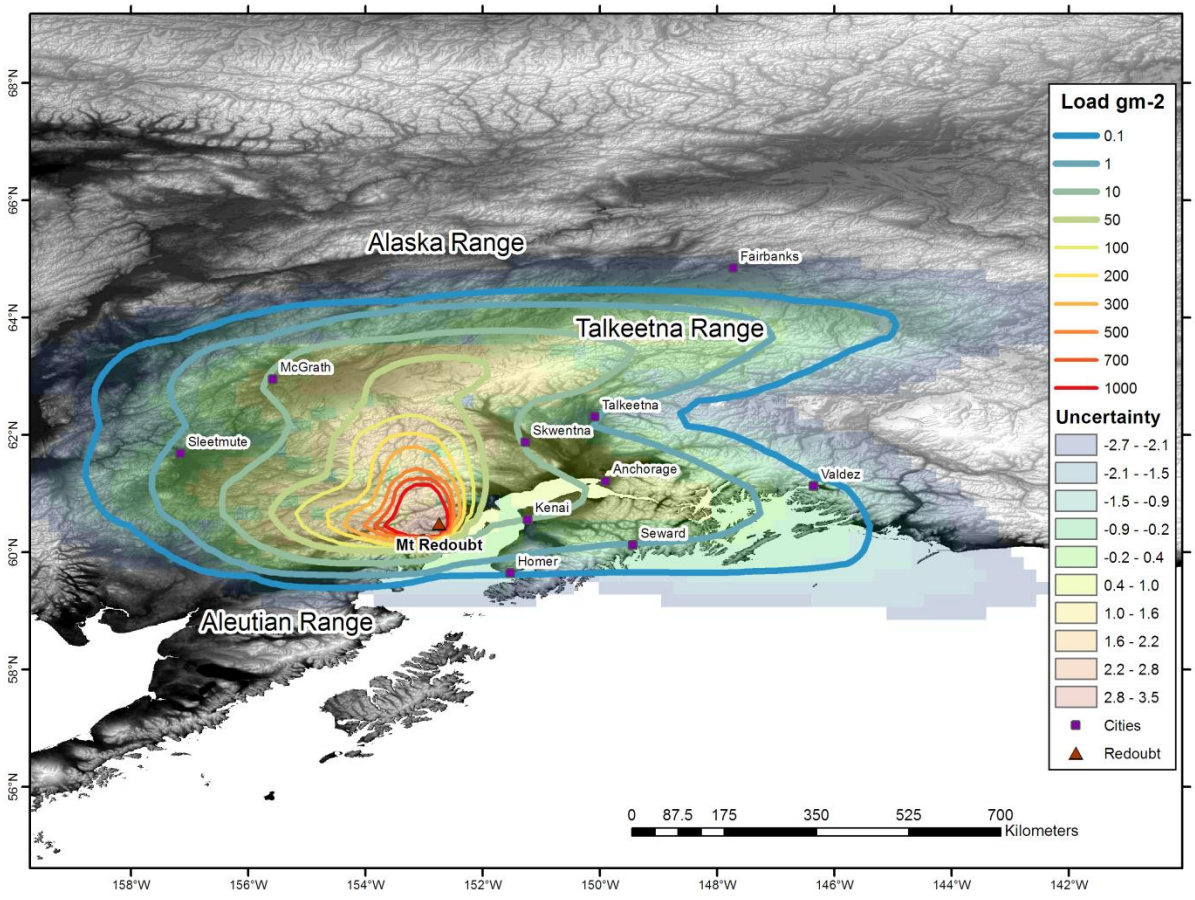

Figure 3.10: Total loadings (gm^{-2}) of events 2-6 were computed as the average of the cumulative total loadings for runs 0 and 7. Uncertainties in model loadings were calculated as the log_{10} of the standard deviation. Mt. Redoubt is marked by a brown triangle, and cities are denoted by purple squares. The gray vertical line represents the cross-section over which spatial and temporal deposit gradients were examined.

Incorporating this uncertainty range, the total cumulative deposit loadings varied from ~7000 ± 3000 g/m^{-2} near the vent to <0.1 ± 0.002 gm^{-2} on the outskirts of the deposits. Deposits from events 2 - 6 covered a total area of 3.7 X 10^6 km^2 and stretched hundreds of kilometers in all directions from the source.

3.4.2 Spatial and temporal gradients of total deposit loadings

The vertical line drawn from Mt. Redoubt and extending ~ 600 km north in Fig. 3.10 denotes a cross-section of the region of most overlap in deposits from each event. This line was constructed to investigate the contributions of each of events 2 – 6 to the total deposit loading, as well as the timescales important for the deposition of ash from these short "puff" events. The contribution of each event to the total cumulative loading for events 2 – 6 are shown in Fig. 3.11.

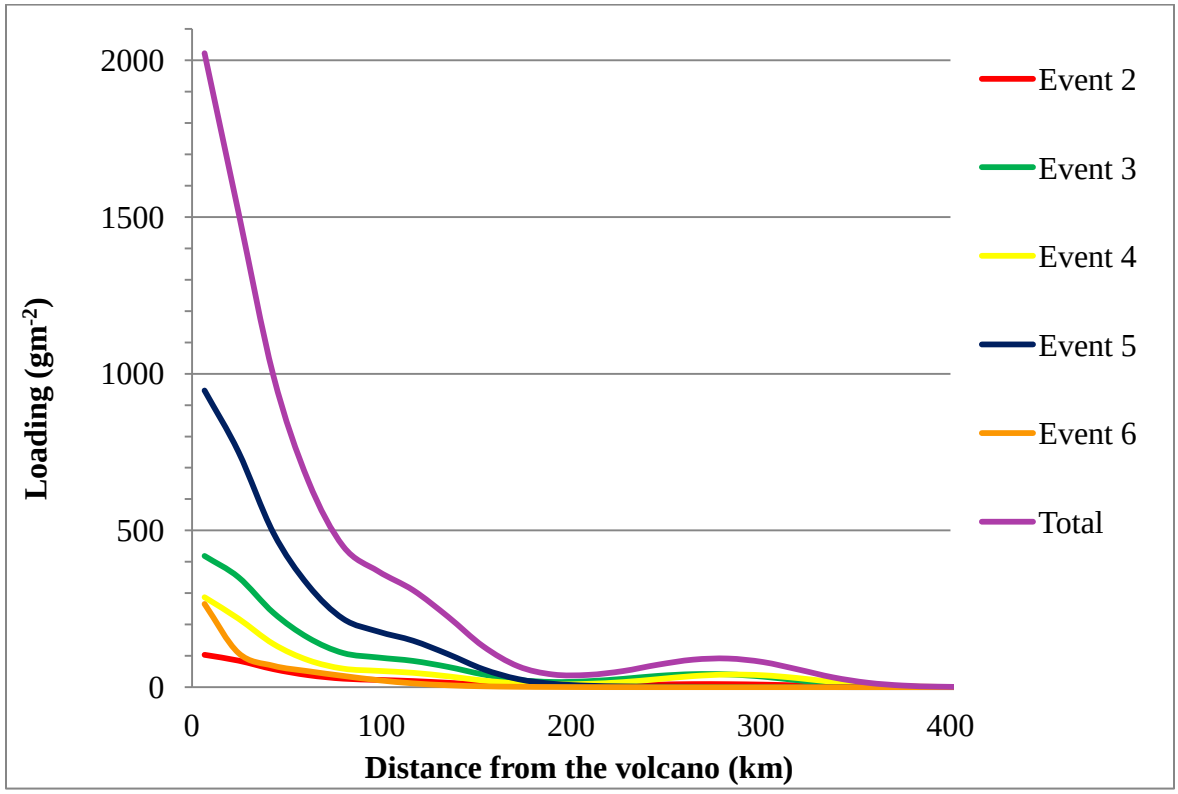

Figure 3.11: Gradients of total ash loadings for events 2 – 6 and total cumulative loading for all events, calculated for the cross-section drawn in Figure 9.

In this cross-section, event 5 contributed most to the total loading from 0 – 200 km, followed by events 3, 4, 6, and 2. Event 6 contributes comparatively little ash despite having one of the highest maximum loadings because the cross-section did not include the areas of highest loading for this event. Cross-sectional loadings for events 2, 5, and 6 fall to ~ 1 gm^{-2} at distances greater than 200 km, and gradually taper off to zero around 500 km. However, loadings for events 3 and

4 fall to ~ 10 gm^{-2} around 200 km and increase again to ~ 40 gm^{-2} around 250 km. This indicates that events 3 and 4 are the main contributors to the secondary maximum observed in Fig. 3.5.

Total deposit loading histories along the cross-section line shown in Fig. 3.10 are depicted in Fig. 3.12a – e.

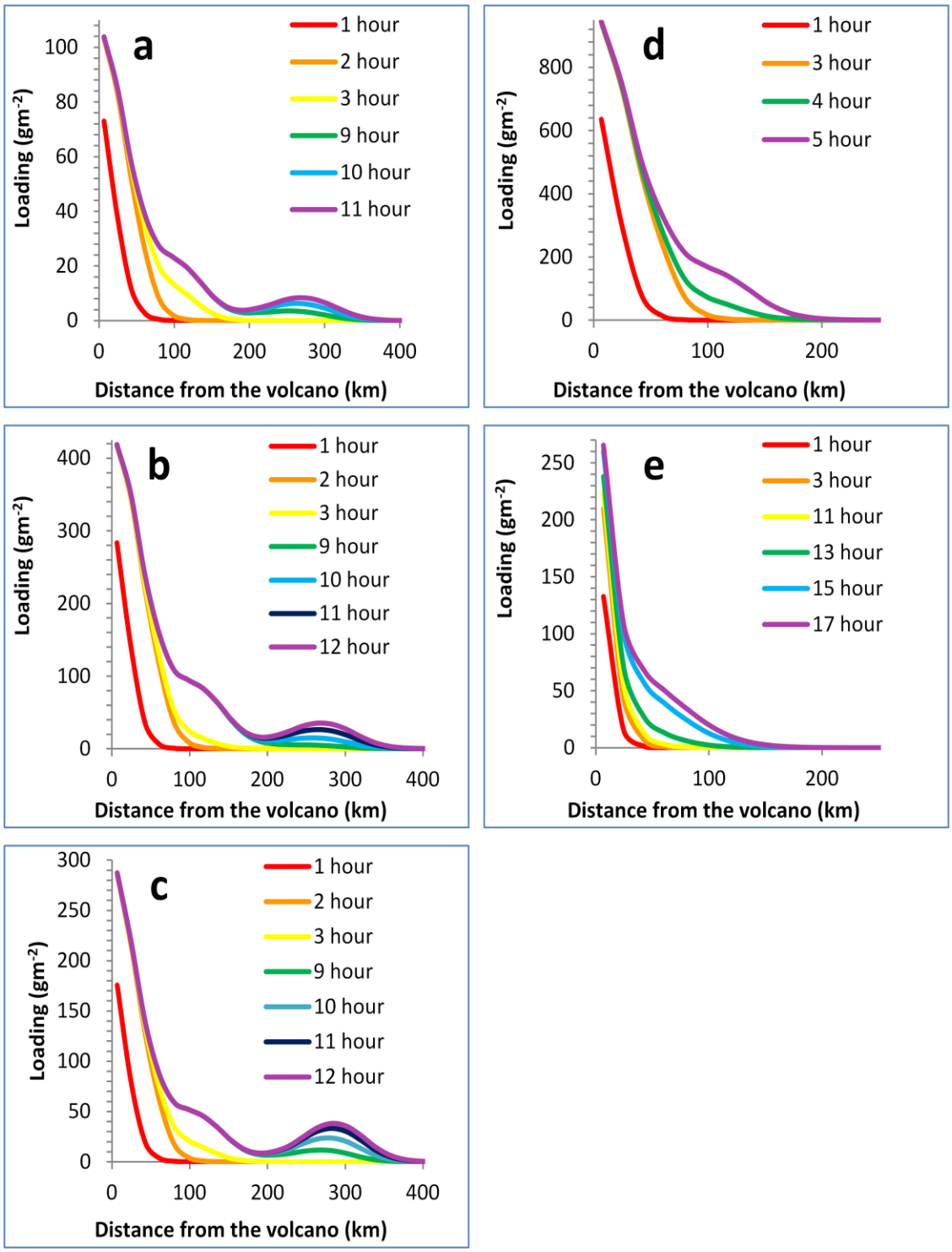

Figure 3.12: Temporal gradients of ash loadings from event 2 (a), event 3 (b), event 4 (c), event 5 (d), and event 6 (e) for a cross-section drawn in Figure 9. Each curve shows the loading along the cross-section at a number of hours after the onset of the eruption. Times for which the loadings were the same were omitted. The purple curve represents the last time for which the loading changed, or the time for all ash from the eruption to settle out along the cross-section.

Times were computed as the number of hours lapsed after the onset of the eruption. Times for which the loading gradients overlap are not shown. The last time plotted in each figure denotes the time at which the loading gradient does not change with subsequent time steps. This time is the number of hours required for the total deposit to form and represents the timescale over which deposition occurred along the cross-section for the particular eruptive event. Events 2 – 4 (Fig. 3.12a – c) all had similar times for all ash to accumulate, ~ 11 – 12 hours. These events occurred in short succession of one another and had similar plume heights and MFRs, but the duration of event 2 was much shorter. The shorter duration led to smaller amounts of ash in the atmosphere than produced by events 3 and 4, which took an hour less to fully settle out. Each of events 2 – 4 also exhibited a secondary maximum, which developed ~ 200 – 400 km from the vent around 9 hours after each of the eruptions.

Event 5 (Fig. 3.12d) occurred a few hours after the conclusion of event 4, and had a larger plume height and MFR. Despite having similar durations as events 3 and 4, event 5 deposited all ash along the cross-section in ~ 5 hours. This is likely due to changing meteorological conditions around the volcano throughout the day, as evidenced by ash from events 2 – 4 being transported much farther north and dispersed over a wider area than ash from event 5 (Fig. 3.5 and 3.6). Meteorological conditions also lead to the more westerly direction of ash transport and deposition field for event 6 (Fig. 3.7). Event 6 had a similar duration, plume height, and MFR to event 5, yet the time for all ash to settle out along the cross-section was significantly longer, ~ 17 hours (Fig. 3.12e). This longer settling time can likely be attributed to different meteorology between the two events.

3.1 Conclusions

To our knowledge, there have been no studies on radiative impacts of volcanic ash deposits in the Arctic, despite their potential to be regionally very important. In order to determine changes in surface reflectivity caused by ash deposited on ice and snow, loading fields and areal extents of deposits must first be characterized. The 2009 eruption of Mt. Redoubt was chosen as a case study because of extensive deposits reported from this eruption by the AVO and documented early snowmelts caused by ash deposits unto ice and snow by *Schaefer et al*. [2012]. We assessed the areal extents and loadings of ash deposits from the eruption of Mt. Redoubt using a VATDM, which allowed for treatment of the source conditions of the eruption. Our approach constrained best-fit model parameters of a well-studied event to estimate parameters for other ash depositing eruptive events. The Fall3D simulations were validated against satellite data and field measurements. Satellite retrievals were often impaired by cloudy conditions and high surface reflectivities, which are common to the Arctic in late winter and early spring. To test the ability of the model to reproduce areal extent, additional eruptive events which transported plumes over dark ocean surfaces were selected and compared to satellite observations.

Modeled ash plume extent and deposit loadings showed overall good to moderate agreement with satellite and field data. Discrepancies in modeled and measured loadings tend to be larger farther from the vent, which could indicate issues with wind field resolution or processes, such as ash aggregation, not considered in the model. The range of uncertainties and corresponding range in loadings would be expected to produce large variations in surface albedo changes due to ash deposition. This must be considered in assessments of radiative forcing. Modeled loadings were particularly sensitive to MFR, ash particle nonsphericity, and plume

source type. The model had an intermediate to low sensitivity to particle size distribution, and low sensitivities were observed for horizontal diffusion coefficients and Suzuki source type.

Eruptive events produced significant loadings of deposited ash that covered large areas. A total cumulative deposit area of 3.7×10^6 km^2 was produced from events 2 - 6. Total cumulative deposit loadings ranged from ~7000 ± 3000 g/m^{-2} near the vent to <0.1 ± 0.002 gm^{-2} on the outskirts of the deposits. Spatial gradients in total ash deposit loading revealed the contributions of each event to the total loading along a cross-section. Temporal gradients of total ash deposit loading showed that fallout time along the cross-section for each event ranged from ~5 – 17 hours. Our deposit loading results suggest that ash from a series of short duration "puff" events can produce significant deposits hundreds of kilometers from the volcano that are important on a regional level.

It must be stressed that while ash dispersion models may produce good overall larger scale agreement, there are still problems capturing smaller scale dynamics, on the order of tens of kilometers. However, these models are absolutely essential for calculations of the radiative impacts of ash deposition in the absence of sufficient satellite and field data. Because of the persistent cloudiness, highly reflective surfaces, and the remoteness of the Arctic region, this approach would be necessary for a large number of Arctic volcanic eruptions. Future work will address the need for better constrained eruption-specific model input parameters, particularly those for which the model is highly sensitive (i.e., MFR, source type, and nonsphericity of ash particles). This will provide more accurate ash deposition estimates.

CHAPTER 4

SURFACE RADIATIVE IMPACTS OF ASH DEPOSITS FROM THE 2009 ERUPTION OF MT. REDOUBT

4.1 Introduction

The climate of the Arctic region is especially sensitive to perturbations in the regional radiative energy budget [e.g. *Curry et al. 1996, Alexeev 2007*]. An important modulator of Arctic radiation climate is the presence of aerosols [*Shindell*, 2007], both natural and anthropogenic. The radiative effects of smoke, dust, and haze in the Arctic have been well-studied [e.g. *Stone et al.*, 2007, 2008; *Quinn et al*., 2008], but the impacts of volcanic aerosols on the Arctic environment have largely been ignored [*Young et al*., 2012]. Compared to the more predictable seasonal frequencies of the occurrences of smoke, dust, and haze, volcanic eruptions in the Arctic occur unexpectedly and quite frequently. As of October 2013, there are ~ 4 volcanoes currently erupting and ~ 10 volcanoes experiencing unrest above 55^{o}N (http://www.volcano.si.edu/). Although the durations and intensities of eruptions can vary, volcanic eruptions have the capacity to be long duration (months to years [*Simkin and Siebert*, 1994]) and high intensity events, expelling large amounts of ash and gases into the atmosphere.

Young et al. [2012] calculated a range of radiative effects that can be expected for a plume from a typical mid-sized Arctic eruption and compared the magnitudes of the effects to those for plumes of the other aerosols types typical to the Arctic environment. It was found that volcanic plumes with compositions rich in ash have magnitudes of forcing which are much higher than those for other aerosol types under the same environmental conditions [*Young et al*., 2012].

The radiative importance of volcanic ash in the Arctic is expected to be magnified, because surface deposits can remain long after a volcanic plume has passed over and dissipated. In addition, the Arctic is the second largest desert in the world. As such, little snowfall would cover ash deposits, although winds could scatter them, reducing their surface loadings. Deposition of solar absorbing particles, such as soot, dust and volcanic ash, has been shown to alter surface albedo and cause early snowmelts, which can have profound impacts on the regional climate and hydrologic cycle. Additionally, ash fall is capable of increasing the amount of diffuse radiation available to plants. In the Arctic, the raditive impacts of surface dust [*Painter et al*., 2010] and soot [*Flanner et al*., 2007] deposits have been studied, but to our knowledge, the surface radiative impacts of volcanic ash deposits from an Arctic eruption have never before been considered.

The 2009 eruption of Mt. Redoubt in Alaska, USA (60.49 N, 152. 74 W) was selected as a case study because it produced extensive ash deposits that stretched hundreds of kilometers in all directions from the volcanic source [*Schaefer et al*., 2012; *Young et al*., 2014] and was associated with early snowmelt [*Schaefer et al*., 2012]. According to the Alaska Volcano Observatory (AVO), Alaska experiences on average two volcanic eruptions per year. The 2009 eruption of Mt. Redoubt was considered a mid-sized volcanic eruption. Small to mid-sized volcanic eruptions occur more frequently in the Aleutian arc and provide an intermittent source of ash and gases to the environment than larger eruptions.

This paper assesses a range of surface albedo change and radiative forcing due to ash deposition that can be expected from a mid-sized volcanic eruption, using the ash loading fields reported for the 2009 eruption of Mt. Redoubt in *Young et al*. [2014]. We assess the hydrological importance of this eruption by making estimates of snowmelt amounts, and we compare the

calculated surface albedo change and radiative forcing,to other depositional events associated with different aerosol types.

4.2 Methodology

The SNow, ICe, and Aerosol Radiation model (SNICAR) [e.g., *Flanner and Zender*, 2005, 2006*; Flanner et al*., 2007] was employed to calculate the solar albedo change and net radiative flux fields at the surface produced by total cumulative ash deposits from the major land depositing events from the March 2009 eruption of Mt. Redoubt in Alaska, USA (Table 4.1).

Table 4.1: Dates and times (UTC) for major land depositing events from the 2009 eruption of Mt. Redoubt.

Event number	Date (UTC)	Time (UTC)
2	3/23/2009	7:02
3	3/23/2009	8:14
4	3/23/2009	9:38
5	3/23/2009	12:30
6	3/24/2009	3:40

The SNICAR model allows the user to choose from different two-stream approximations, and a multi-layer solution from *Toon et al*. [1989], to solve the plane parallel radiative transfer equation for multiple layers in snow. In allowing for multiple layers, the model can address the vertical differences in snow and impurity properties. This work utilizes a hemispheric mean two-stream approximation *Toon et al*. [1989], because other approximations can give unphysical results in the near-infrared. Therefore, the hemispheric mean was deemed more appropriate for a larger variety of situations, including calculating shortwave broadband albedos. The model requires solar zenith angle (SZA) and underlying surface spectral or monochromatic reflectance, snow layer properties (i.e., snow layer thickness, snow density for each layer, and snow effective radius), and impurity properties (i.e., particle mass mixing ratios, effective radius, and refractive index).

A monochromatic underlying surface reflectance of 0.25 was used to simulate snow cover on dry grass [*Coakley*, 2002]. At approximately 60^{o}N, the highest SZA for a day in mid March is 55^{o}. A lower SZA of 75^{o} was chosen to represent a middle point between the highest and lowest daily sun angles. Solar fluxes for a clear sky in Greenland were used to compute direct-beam incident fluxes [*Mark Flanner*, personal communication]. Daily snow layer thickness from the Natural Resources Conservation Service's (NRCS's) SNow TELemetry (SNOTEL) for Alaskan sampling stations were used to estimate snow layer thickness and Snow Water Equivalent (SWE) for the entire deposit region. Snow density was computed from SWE data. A snow depth of 1 m and a snow density of 190 kg m^{-3} were used. Effective snow grain size radius can range from 50 – 1100 μm [*Painter et al*., 2003], with older snow having larger grains. Profiles of snow effective radius for the region and times of the eruption were not available. Therefore, a snow grain radius of 100 μm was selected to represent newer snow, and a radius of 1000 μm was selected to simulate aged snow. Optical properties of snow from *Warren et al.* [2006] were used.

Ash deposit particle mixing ratio fields (in ppb by mass) were determined from total cumulative ash deposit loading fields taken from *Young et al*. [2014] for the entire period of major land-depositing events (March 23 and 24), listed in Table 4.1. In this study, spherical ash particles produced better agreement, except in locations that were ≥ 210 km from the volcanic vent. In these regions, particles with nonsphericity = 0.7 produced loadings that agreed better with field data. Therefore, we used loading fields produced by spherical particles for locations < 210 km and loading fields of particles with nonsphericity = 0.7 for locations ≥ 210 km. The effects of loading variations on modeled integrated solar albedo are discussed. The Fall3D volcanic ash dispersion and transport model (VADTM) [*Folch et al*., 2009; *Costa et al*., 2006]

was used in a setup similar to that of *Young et al*. [2014] to produce spatial and temporal fields of deposited ash median radius and standard deviation.

The optical properties of the ash were computed according to Mie theory for a lognormal particle distribution, using total cumulative deposited ash mean effective radii and standard deviation fields calculated from Fall3D and the spectral refractive indices for andesitic ash [*Pollack et al*., 1973]. Although consideration of nonspherical particles is an important part of determining total cumulative ash deposit loadings [*Young et al*., 2014], only spherical particles were considered in calculating the optical properties of ash. This is because the single scattering properties of nonspherical particles in radiative flux calculations are well-approximated using spheres [*Fu et al*., 2009]. Only aerosol-sized ash particles (radius ≤ 50 μm) were considered in this study. This is because the larger sized ash particles, are minor in abundance and confined to areas very close to the vent.

In the SNICAR model, ash was deposited on top of the snowpack. Some regions did experience new snowfall on top of the ash layer [*Schaefer and Wallace*, 2012]. However, the areas and locations over which this occurred are not reported. Although initially ash deposits might be blanketed by new snow, ash is a hydrophobic particle and will therefore not be incorporated into deeper layers of the snowpack, even as the snow melts. Rather, ash will be concentrated at the surface as the melt water trickles through the snow matrix, straining the ash out at the top layer of the snowpack. All of the ash in this study is concentrated in the first centimeter of the snowpack. Winds could be an issue in blowing and dispersing ash initially, but after some melting has occurred, the particles become wetted and adhere to the snow [*Schaefer et al*., 2012]. Therefore, the blanketing of ash deposits by snow and the dispersion of deposits by

wind were not considered here in assessing a range of radiative impacts from a typical mid-sized Arctic eruption.

Snowmelt estimations were made using the restricted degree-day radiation balance approach described in *Melloh* [1999]:

$$M = r\,T_d + m_Q\,F_{net,\,SW} \quad (4.1)$$

Where M is the snowmelt (cm day^{-1}), r the constant restricted degree-day factor (cm day^{-1} $^oC^{-1}$), T_d the daily mean temperature over 24 hours (^oC day), m_Q a physical constant converting radiation to SWE and is equal to 0.026 cm day^{-1} (W m^{-2})$^{-1}$, and $F_{net\,SW}$ the net solar surface radiation (W m^{-2}). Values of T_d were taken from SNOTEL and $F_{net\,SW}$ was calculated by the SNICAR model. *Martinec* [1989] showed that the values of r vary only slightly, from 0.20 to 0.25 cm day^{-1} $^oC^{-1}$, throughout the snowmelt period. According to *Kustas et al*. [1994], low values of r occur when low relative humidity increases latent heat loss due to evaporation. Because the Arctic air is very dry, we use a r value of 0.20 cm day^{-1} $^oC^{-1}$.

4.3 Results and Discussion

The median radius by mass for all sizes of ash particle deposits decreases with distance from the volcanic vent (Fig. 4.1a) and is comparable to the mass median radii of deposits measured by *Mastin et al*. [2013] for this eruption at four points located at various distances from the vent (Table 4.2).

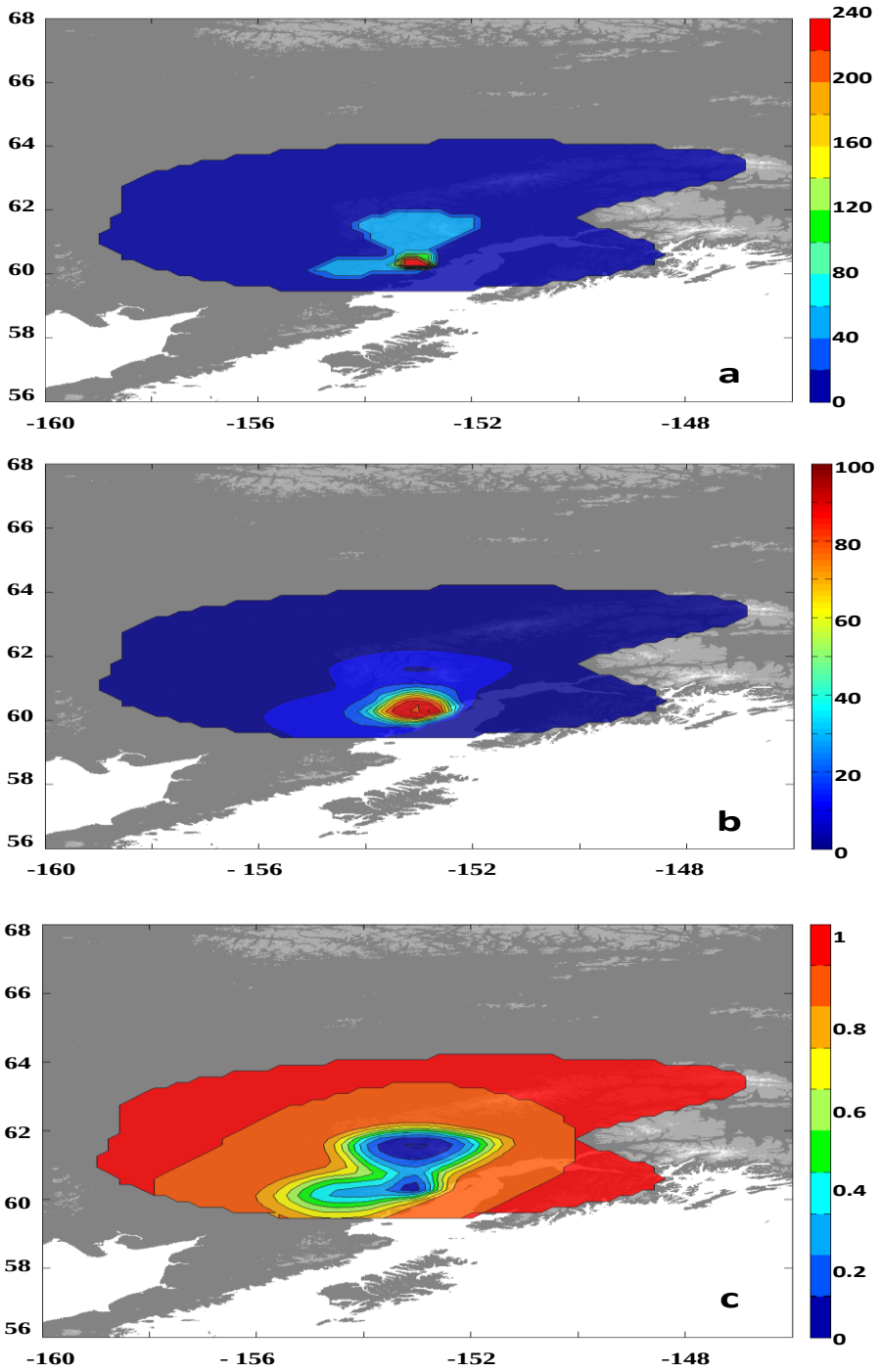

Figure 4.1: (a) Mass median radius for all particle sizes (b) standard deviation for all particle sizes (c) fraction of ash deposits that are aerosols (≤ 50 μm). The last contour in all plots corresponds to a loading of 0.1 g m^{-2}, as in *Young et al*. [2014].

Table 4.2: Measured and modeled mass median radius for all particle sizes at four distances north of the volcanic vent.

Distance (Km)	**Mass median radius (μm)** ***Mastin et al.* [2013]**	**Mass median radius (μm) Modeled with Fall3D**
218	≤ 31	15.75 – 31.25
120	≤ 31	31.25
29	125	62.5
12	1000	250

The median radii from *Mastin et al.* [2013] are similar to those modeled at the same distances, except for at the closest distance to the vent (12 km), where the measured radius is an order of magnitude larger than the modeled radius. This discrepancy may be due to the effect of particle aggregation occurring near the vent, which is not accounted for in the Fall3D model. Fig. 4.1b displays the standard deviation of the deposit size distribution, which decreases with increasing distances from the vent. As larger sizes are removed and the number of size bins decrease, the spread of the distribution also decreases moving towards the outskirts of the deposits. The fractions of ash that are in the aerosol size range are shown in Fig. 4.1c. The aerosol size fraction is carried further than larger sizes, and therefore the ratio of aerosol ash increases with distance from the vent. The median radii for only ash sizes ≤ 50 μm are shown in Fig. 4.2, and were used in optical modeling.

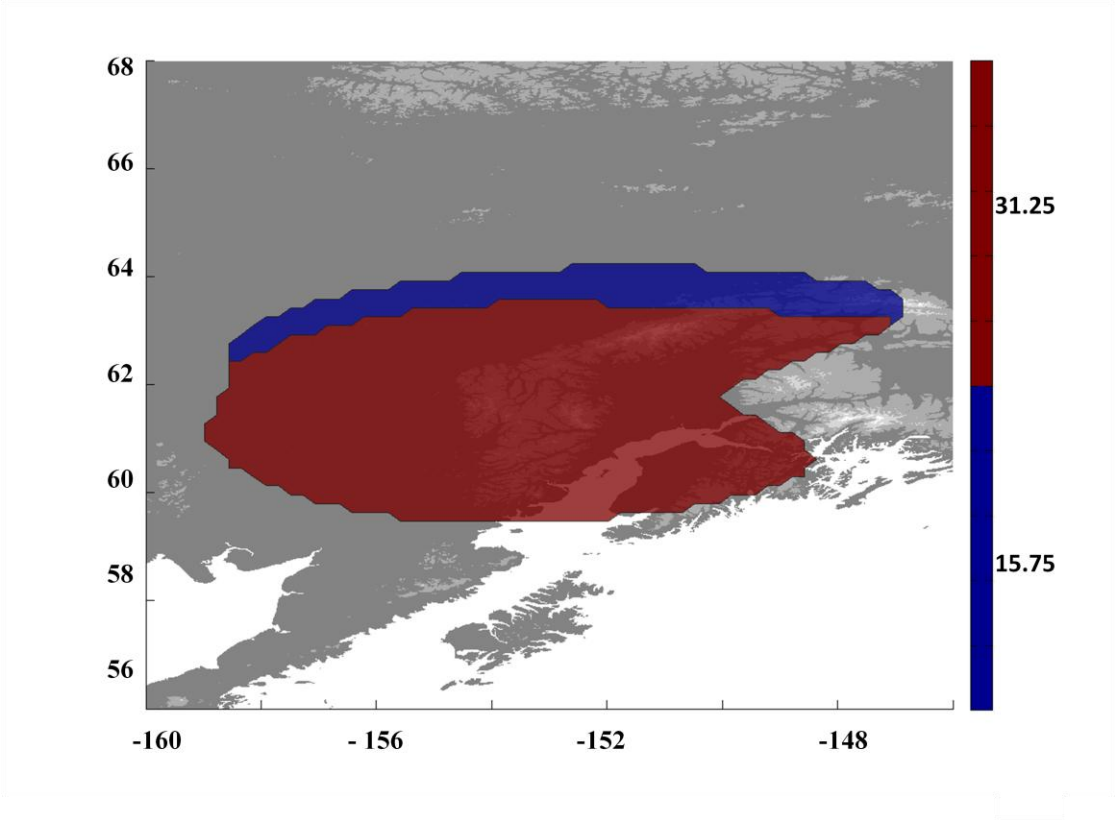

Figure 4.2: Median radius fields for ash radii ≤ 50 μm.

Note that the median radius did not vary much because of comparatively few size bins in this range, and the spread for the distributions was small and approached zero. This is a direct result of the discrete size bins, and in nature, more spread would be expected.

In order to calculate the albedo change caused by ash deposits, the albedos of pure snow for the selected snow grain size radius and SZA must first be calculated using SNICAR. At a SZA of 75^{o}, the solar integrated albedo is 0.8476 and 0.7394, for grain sizes of 100 μm and 1000 μm, respectively. Coarser-grained, older snow is optically darker, because the radiation must travel through a greater optical depth of snow to get the same amount of extinction, increasing the probability of a photon being absorbed [*Flanner et al*., 2007].

The albedos computed for ash deposits are subtracted from albedos of pure snow to obtain the change in albedo caused by the deposits. Reductions in integrated solar albedo for a snow grain size of 100 μm are shown in Fig. 4.3a and range from 0.4969 closest to the vent to 0.0023 on the outskirts of the deposits, around a loading of 0.1 g m^{-2}.

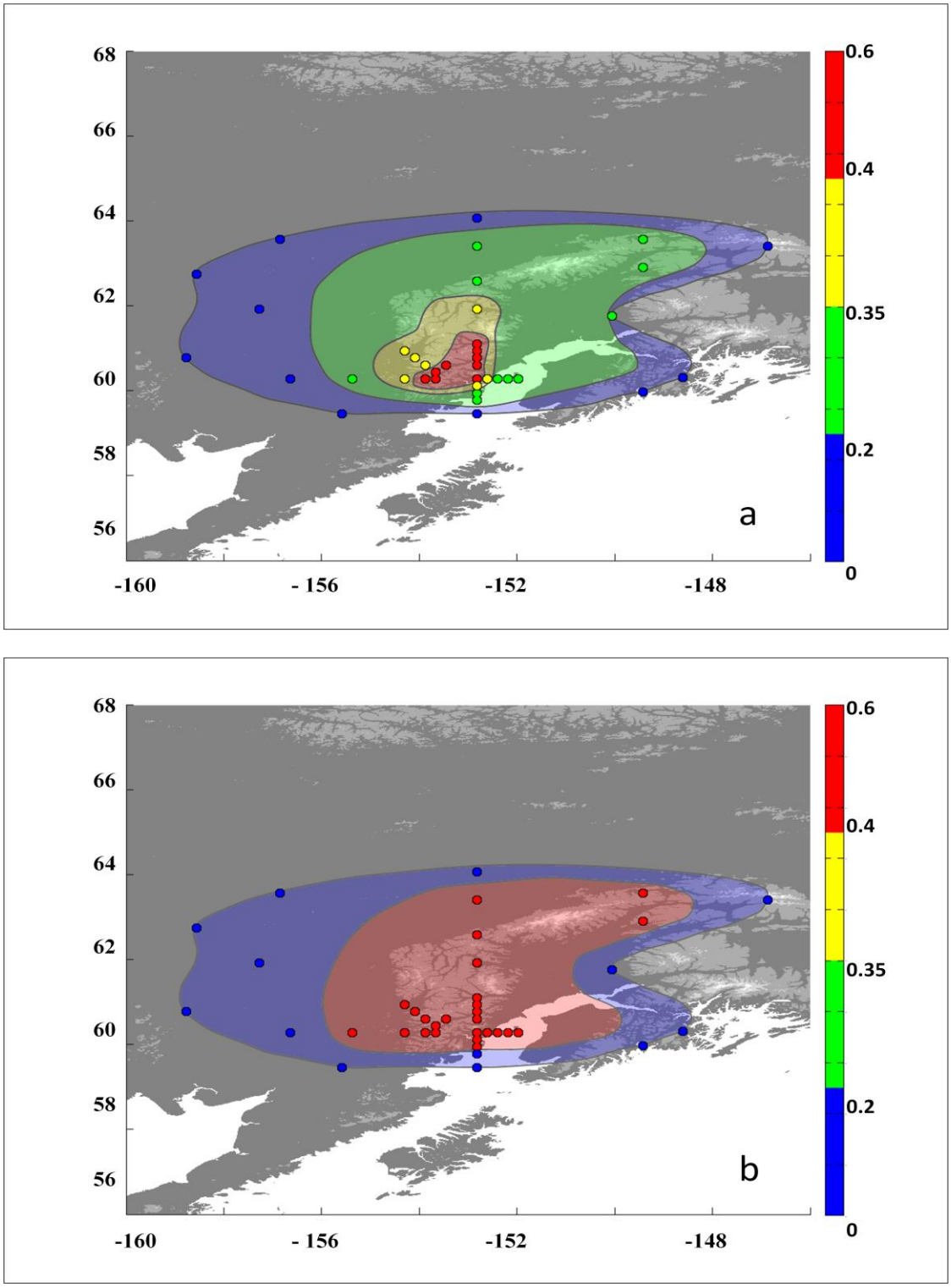

Figure 4.3: Reductions in solar broadband albedo for (a) ash deposits on new snow (median radius = 100 µm) (b) ash deposits on old snow (median radius = 1000 µm). Note that Fall3D and SNICAR are not coupled, so fields were drawn based on calculations made at several points, which are denoted by circles.

The high and low albedo change values corresponded to concentrations of ~ $1x10^8$ and $6.9x10^4$ ppb, respectively. Because the median radius over which optical calculations were performed did not vary much across the deposits, the optical properties of the aerosol-sized ash deposits were similar across much of the region. Therefore, much of the variation in the albedo reduction fields is due to the ash loading, making loading assessments a key player in these analyses. Solar integrated albedo reductions for 1000 μm snow grain size are displayed in Fig. 4.3b. These values vary from 0.6293 closest to the vent to 0.0029 on the outskirts of the deposits. The large snow grain size and the increasing amounts of ash moving closer to the vent amplify the reduction in albedo. This causes the larger changes in albedo that occur further from the vent in Fig. 4.3b when compared to Fig.4.3a.

There were no satellite observations of albedo for deposits from this eruption, because bright surfaces and clouds were a constant issue for retrievals. No field measurements of albedo were made. Citizen scientists did document and photograph the extent of ash deposit coverage in their areas, as in Fig. 4.4, taken from *Schaefer et al*. [2012].

Figure 4.4: Documentation of ash coverage in Skwentna, AK (61.9 N, 151.25 W) from *Schaefer et al*. [2012].

Figure 4.4 was taken at Bentalit Lodge, near Skwentna (61.9 N, 151.25 W), and shows complete coverage of the surface by ash. Based on this photograph, it is expected that albedo change would be significant for this region. Significant albedo reductions are observed in Fig. 4.3a and b near Skwentna.

Here, we report concentrations of ash in snow that range from ~ 6.9×10^4 – 1×10^8 ppb, and integrated solar albedo reductions of ~ 0 – 59% for new snow and ~ 0 – 85% for old snow. Some typical concentrations of black carbon in snow are ~ 5 – 50 ppb corresponding to a spectrally averaged albedo reduction of ~1 – 3% [*Clark and Noone*, 1985; *Warren and Wiscombe*, 1985]. Although black carbon would be expected to be more absorbing than volcanic ash for a similar particle size and concentration, the extreme loadings and larger particle sizes that can be present from a mid-sized volcanic eruption produce albedo changes that dwarf those

due to black carbon. Integrated solar albedos for volcanic deposits in Antarctica were reported by *Dadic et al*. [2013]. It was found that for a range of concentrations between ~ 1 – $1x10^6$ ppb of ash in snow, the albedo reduction was ~ 0 – 37 % for clear sky conditions. The largest deposit concentration in *Dadic et al.* [2013] was two orders of magnitude smaller than the largest deposit concentration reported here, either because *Dadic et al*. [2013] was only considering ash located a greater distance from the volcanic source, or the eruptions which produced the ash were of a smaller scale. At an ash concentration of 2.8 x 10^7 (~ 200 km from the vent), we calculate an albedo reduction of ~37% for new snow, which is similar to what *Dadic et al*. [2013] computed as the largest albedo reduction for the highest ash concentration. However, these studies are not directly comparable, because deposit concentrations from *Dadic et al*. [2013] also included all ash sizes, while this study only focuses on aerosol-sized ash deposits. Hence, the albedo changes for this study would be expected to be even more extreme if calculated in the same manner as *Dadic et al*.[2013], further demonstrating the capabilities of mid-latitude eruptions to significantly alter surface albedo.

Shortwave surface net flux fields are shown in Fig. 4.5 and are defined as the difference between incoming and outgoing surface shortwave radiation.

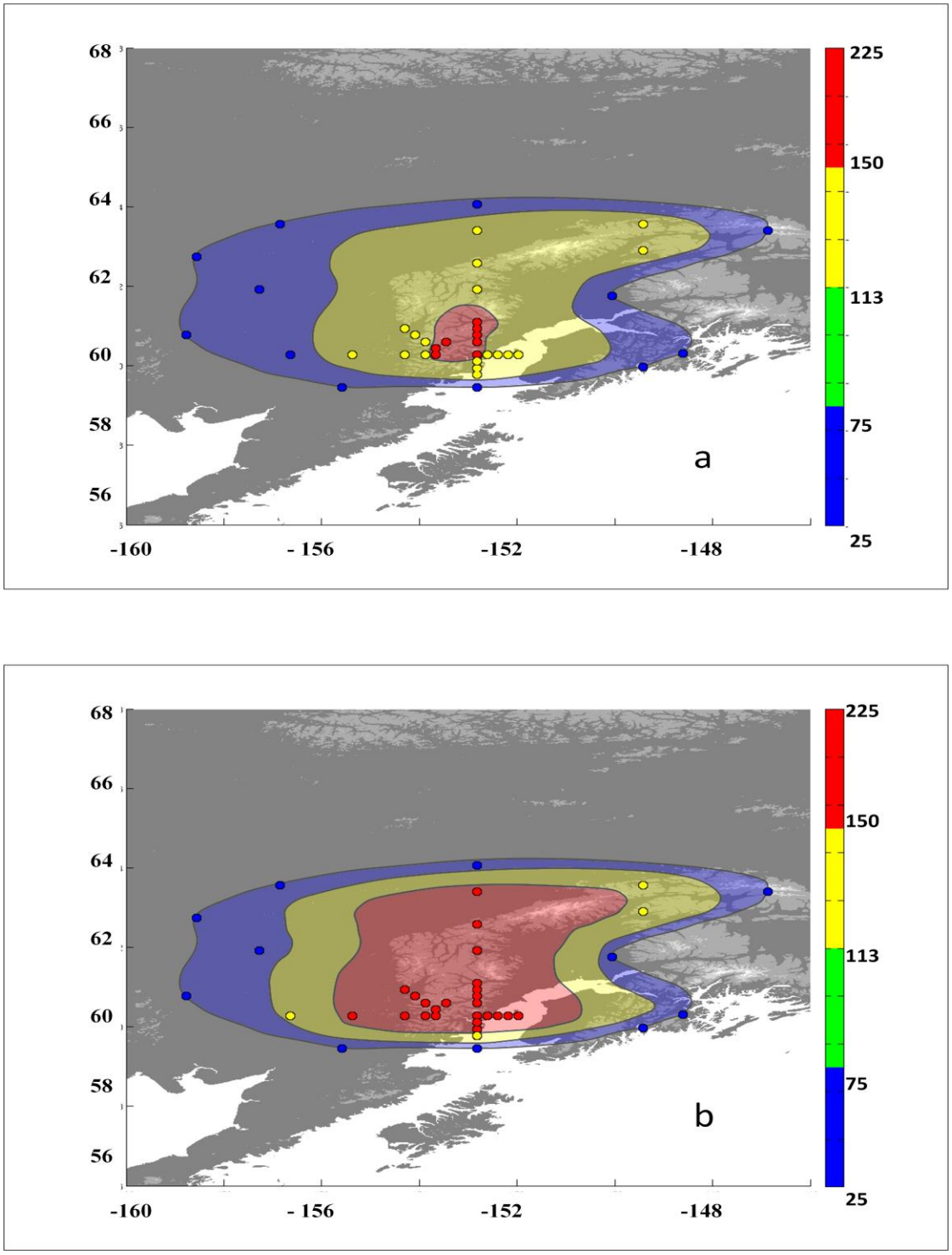

Figure 4.5: Daily mean surface solar net fluxes in Wm^{-2} for (a) ash deposits on new snow (median radius = 100 µm) (b) ash deposits on old snow (median radius = 1000 µm). Note that Fall3D and SNICAR are not coupled, so fields were drawn based on calculations made at several points, which are denoted by circles.

The shortwave surface net fluxes for pure snow are 38.1 $Wm^{-2}$for new snow and 65.2 Wm^{-2} for aged snow. The net fluxes associated with ash deposits on snow ranged from 38.7 – 162 Wm^{-2} for new snow and 65.9 – 222 Wm^{-2} for aged snow. Since these values were all computed at a mid SZA, they can be viewed as daily averages. As a comparison to similar work, *Skiles et al*. [2012] calculated springtime daily mean forcings for dust deposits on snow in Colorado to be ~ 35 – 70 Wm^{-2}, corresponding to concentration values of $2x10^5$ – $4x10^6$ ppb, respectively. When forcings for ash deposition from this eruption are calculated using the method put forth in *Skiles et al.* [2012], minimum forcing values due only to the direct effects of ash deposition onto snow range from ~ 0 – 96 Wm^{-2}, from the outmost deposits to the vent.

All calculations were done for total deposits from each eruptive event listed in Table 4.1. However, one can hypothetically consider the effects of surface darkening due to ash fallout of a passing plume, such as for the plumes from *Young et al*. [2012], and how this would be expected to change the shortwave radiative effects caused by the plume. The decreased surface albedo due to ash deposits will cause a reduction in upwelling surface radiation, which will decrease multiple scattering between the surface and the plume and cause less absorption and less warming of the plume. The plume will also start to absorb less radiation because it is continually losing ash and will begin to scatter more radiation, which combined with the darkening of the surface, will lead to less warming at the top of the atmosphere.

Total snowmelt was calculated from shortwave surface net fluxes. It should be noted that ash deposit thicknesses for these events totaled to < 1 cm. This is important because layers in excess of 2.4 cm tend to insulate rather than melt the snow [*Lipman and Mullineaux*, 1981]. According to equation 4.1, snowmelt starts to occur when the average daily surface temperature warms to above 0^oC, which normally occurs at the end of March to early - mid April, according

to SNOTEL. If snowmelt is calculated at 0^{o}C, this will represent a lower bound on snowmelt amount and will quantify the melt that would be produced initially by radiative heating alone. This melting would cause further reduction in snow albedo, leading to increases in $F_{net,SW}$ and surface temperature, which would cause more snowmelt. Fig. 4.6 shows snowmelt fields for ash deposits over new and aged snow at 0^{o}C.

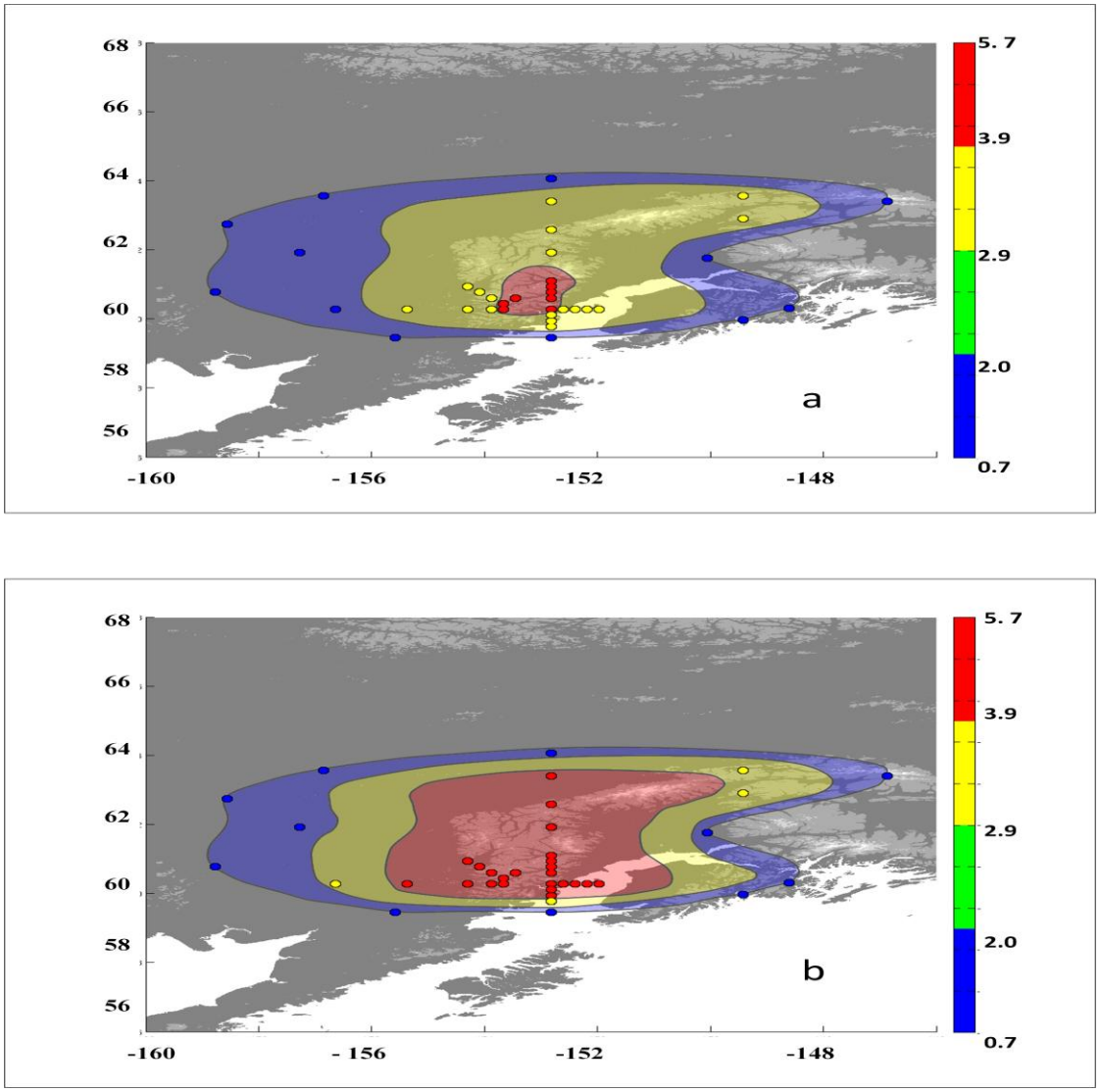

Figure 4.6: Snowmelt rate in cm day^{-1} for calculated for $T_d = 0^{o}$C (a) ash deposits on new snow (median radius = 100 µm) (b) ash deposits on old snow (median radius = 1000 µm). Note that Fall3D and SNICAR are not coupled, so fields were drawn based on calculations made at several points, which are denoted by circles.

It is noted that for this time of year, the snow is more likely to be aged. The snowmelts ranges for new snow were ~ 1.0 – 4.2 cm day^{-1} with the highest snowmelt near the vent and the lowest value at the edges of the deposits. For old snow, the ranges were ~1.8 – 5.8 cm day^{-1}. Pure snow at 0^{o}C melts at a rate of ~ 1.0 for new snow and ~ 1.8 cm day^{-1} for old snow. Therefore, no significantly accelerated snowmelts are expected on the outskirts of the deposits. However, for areas of higher ash loadings/concentrations, daily melt rates are significantly higher (~ 220 – 320%) because of volcanic ash deposits. Many of the highest concentrations were found in mountainous areas where snow would be expected to melt later in the year. Early and accelerated snowmelts can be expected to lead to depletion of runoff in later months and shortages of water resources *Qian et al*. [2009].

4.4 Conclusions

The results presented here demonstrate the importance of volcanic ash deposits from mid-sized eruptions on surface albedo and snow melt. The SNICAR model was used to calculate a range of albedo change, forcing, and snowmelt that is expected for ash deposits unto snow and ice from a mid-sized Arctic eruption, using the 2009 eruption of Mt. Redoubt as a case study. The results show concentrations of ash in snow range from ~ $6.9x10^{4}$ – $1x10^{8}$ ppb, with higher values closer to the vent and lowest at the edge of the deposits, and integrated solar albedo reductions of ~ 0 – 59% for new snow and ~ 0 – 85% for old snow. These albedo reductions are much larger than those typical for black carbon, because of the larger loadings involved, but are on the same order of magnitude as those reported for volcanic deposits in Antarctica. The surface shortwave forcings associated with ash deposits on snow ranged from 0 – 96 Wm^{-2} from the outmost deposits to the vent. The snowmelt ranges at 0^{o}C were ~ 1.0 – 4.2 cm $day^{-1}$for new snow, and ~1.8 – 5.8 cm day^{-1} for old snow. There were no significantly accelerated snowmelts

calculated for the outskirts of the deposits. However, for areas of higher ash loadings/concentrations, daily melt rates are significantly higher (~ 220 – 320%) because of volcanic ash deposits.

Although these calculations have been done for a mid-sized eruption, there have been notable larger eruptions in the Arctic's past (e.g. Laki, 1783 and Nova Erupta-Katmai, 1912). It may be that larger eruptions would tend to deposit enough ash to insulate the snow rather than melt it. This would make ash deposits from mid-sized volcanic eruptions a major agent of deposit-induced snowmelt in the Arctic, as their loadings close to the vent can cause greater albedo reductions than other aerosol types, but the loadings are typically not so great to insulate the snow.

Future studies will include improving ash loading estimates and the acquisition of eruption-specific snow and ash properties for the SNICAR model. Because of the lack of satellite data that is often problematic for this region due to the presence of clouds and the high surface reflectivity, field measurements of albedo change and snow ablation rates would be very useful. If traveling to the field is not possible, conditions could be simulated on a smaller scale in the lab. In addition, the radiative calculations done here could be made more sophisticated with coupling volcanic eruption source conditions, transport, and deposition, along with the SNICAR model, to a General Circulation Model (GCM), which would allow for the calculation of global effects, if any. We could also consider vegetation fraction and the surface emissivity change caused by ash deposits on snow in future runoff calculations. Clouds are often present in the Arctic, and their effects on the radiative impacts in the presence of volcanic ash deposits should be investigated in the future. The effects of volcanic ash deposition on other types of environments might also be considered, these include glaciers at lower latitudes (e.g. in the

Andes) and in Antarctica, where Mt. Erebus is currently erupting. Since the Antarctic is more pristine than the Arctic, volcanic ash may be the only impurity present in the snowpack.

CHAPTER 5

CONCLUSIONS

5.1 Dissertation Summary

In Chapter 2, we used a satellite-integrated approach to investigate the radiative impact of volcanic aerosols in the Arctic. In general, environmental factors can govern both the sign and magnitude of the direct aerosol radiative forcing, direct aerosol radiative forcing efficiency and heating/cooling rates. The ability of environmental conditions to change whether an aerosol layer will contribute to warming or cooling at TOA and the surface is especially significant when considering the Arctic region, where surfaces vary from ocean to snow, and seasons dramatically shift the amount of incoming solar radiation.

Our results demonstrate a potential for volcanic aerosol to provide a sizeable contribution to the radiative effects and even exceed the impacts other types of aerosol when significant proportions of volcanic ash are present, as in young volcanic plumes. Therefore, volcanic aerosol, although sporadically present, can have a significant radiative impact in the region.

In Chapter 3, we assessed the areal extents and loadings of ash deposits from the eruption of Mt. Redoubt using a volcanic ash transport and dispersion model, which allowed for treatment of the source conditions of the eruption. Our novel approach constrained best-fit model parameters of a well-studied event to estimate parameters for other ash depositing eruptive events. The simulations were validated against satellite data and field measurements.

Modeled ash plume extent and deposit loadings showed good to moderate agreement with satellite and field data. Modeled loadings were particularly sensitive to mass flow rate, ash particle nonsphericity, and plume source type. The model had an intermediate to low sensitivity

to particle size distribution, and low sensitivities were observed for horizontal diffusion coefficients and Suzuki source type.

Eruptive events produced significant loadings of deposited ash that covered large areas. A total cumulative deposit area of 3.7 X 10^6 km^2 was produced from events 2 - 6. Total cumulative deposit loadings ranged from ~7000 ± 3000 g/m^{-2} near the vent to <0.1 ± 0.002 gm^{-2} on the outskirts of the deposits. Our deposit loading results suggest that ash from a series of short duration "puff" events can produce significant deposits hundreds of kilometers from the volcano that are important on a regional level.

In Chapter 4, the snow, ice and aerosol radiation model was used to calculate a range of albedo change, forcing, and snowmelt that is expected for ash deposits unto snow and ice from a mid-sized Arctic eruption, using the 2009 eruption of Mt. Redoubt as a case study. The results show concentrations of ash in snow range from ~ $6.9x10^4$ – $1x10^8$ ppb, with higher values closer to the vent and lowest at the edge of the deposits, and integrated solar albedo reductions of ~ 0 – 59% for new snow and ~ 0 – 85% for old snow. These albedo reductions are much larger than those typical for black carbon, because of the larger loadings involved, but are on the same order of magnitude as those reported for volcanic deposits in Antarctica. The surface shortwave forcings associated with ash deposits on snow ranged from 0 – 96 Wm^{-2} from the outmost deposits to the vent. There were no significantly accelerated snowmelts calculated for the outskirts of the deposits. However, for areas of higher ash loadings/concentrations, daily melt rates are significantly higher (~ 220 – 320%) because of volcanic ash deposits. These early and accelerated snowmelts have the capacity to reduce runoff in later months and deplete water resources.

5.2 Implications for future research

In Chapter 2, we saw that plume specific factors influence the magnitudes of direct aerosol radiative forcing, direct aerosol radiative forcing efficiency and heating/cooling rates. The compositions, thicknesses and aerosol optical depth of volcanic plumes vary greatly and are in many cases difficult factors to constrain. The development of multiphase models [*Dufek and Bergantz*, 2007; *Neri et al*., 2007] to study eruption dynamics may assist in creating better microphysical models for volcanic ash and have the capacity to be modified to treat the formation and transport of other volcanic aerosols, such as sulfates and ice. The deployment of balloons with particle counters attached would help to study the evolution of size distributions. Other plume related simplifications that are often made in radiative transfer modeling which need to be addressed include: the partitioning of volcanic aerosol types at different altitudes, the nonsphericity of ash, and sulfate, water, and/or ice coatings of ash.

In this study, clouds hampered satellite retrievals in many instances. Because of the important radiative effects of volcanic aerosols in the Arctic reported for this study, we recommend that volcanic aerosols be included in future assessments of the Arctic regional radiation budget to facilitate efforts in understanding the radiative impacts of natural aerosols on the Arctic environment.

In Chapter 3, we highlighted the need for better constrained eruption-specific model input parameters, particularly those for which Fall3D was highly sensitive (i.e., mass flow rate, source type, and nonsphericity of ash particles). This will provide more accurate ash deposition estimates. Discrepancies in modeled and measured loadings tend to be larger farther from the vent, which could indicate issues with wind field resolution or processes, such as ash aggregation, not considered in the model. Aggregation models, such as the one developed by

Telling et al. [2013], should be incorporated in volcanic ash dispersion and transport models. Additionally, the process of comminution, which is the breakup of particles due to collisions, is not considered. Comminution is likely very important in the initial conduit, where particle densities and energies are very high and more bounce events between particles occur than aggregation events [*Dufek et al.*, 2012].

In Chapter 4, we identified that loading of ash and the optical properties of ash and snow were important to radiative calculations. Future studies will include improving ash loading estimates and the acquisition of eruption-specific snow and ash properties for the radiative modeling. Though the calculations here have been done for a mid-sized eruption, there have been notable larger eruptions in the Arctic's past (e.g. Laki, 1783 and Nova Erupta-Katmai, 1912). It would be interesting to consider what effects these eruptions would have on albedo and snowmelt. It may be that larger eruptions would tend to deposit enough ash to insulate the snow rather than melt it. This would make ash deposits from mid-sized volcanic eruptions a key player in producing deposit-induced snowmelt in the Arctic, as their loadings can cause greater albedo reductions than other aerosol types close to the vent, but the loadings are typically not so great to cause insulating of the snow. Because of the potential of ash deposits to alter the hydrologic cycle of the Arctic, it is important that the albedo reduction due to the deposition of volcanic ash, along with the deposition of other absorbing aerosols, be considered in Arctic warming mitigation strategies.

Acquiring satellite data in this region is often problematic, due to the presence of clouds and the high surface reflectivity. Therefore, field measurements of albedo change and snow ablation rates would be very useful. If traveling to the field is not possible, conditions could be simulated on a smaller scale in the lab. In addition, the radiative calculations done here could be

made more sophisticated with coupling volcanic eruption source conditions, transport, and deposition, along with the snow, ice, and aerosol radiation model, to a global circulation model, which would allow for the calculation of global effects, if any. We could also consider vegetation fraction and the surface emissivity change caused by ash deposits on snow in future runoff calculations. Clouds are often present in the Arctic, and their effects on the radiative impacts in the presence of volcanic ash deposits should be investigated in the future. The effects of volcanic ash deposition on other types of environments might also be considered, these include glaciers at lower latitudes (e.g. in the Andes) and in Antarctica, where Mt. Erebus is currently erupting. Since the Antarctic is more pristine than the Arctic, volcanic ash may be the only impurity present in the snowpack.

REFERENCES

Alexeev, V. A.,2007. Polar amplification as a preferred response in an idealized aquaplanet GCM. In Geophysical Research Abstracts (Vol. 9, p. 01338).

Alfano, F., Bonadonna, C., Delmelle, P., Costantini, L., 2011. Insights on tephra settling velocity from morphological observations, J. Volcanol. Geotherm. Res. 208(3-4), 86-98, doi:10.1016/j.jvolgeores.2011.09.013.

Anisimov, O.A., Vaughan, D.G., Callaghan, T.V., Furgal, C., Marchant, H., Prowse, T.D., Vilhjálmsson, H., Walsh, J.E., 2007. Polar regions (Arctic and Antarctic). Climate Change 2007: Impacts, Adaptation and Vulnerability. Contribution of Working Group II to the Fourth Assessment Report of the Intergovernmental Panel on Climate Change, Parry, M.L., Canziani, O.F., Palutikof, J.P., van der Linden, P.J., Hanson, C.E. Eds., Cambridge University Press, Cambridge, 653-685.

Bonadonna, C., Connor, C.B., Houghton, B.F., Connor, L., Byrne, M., Laing, A., Hincks, T.K., 2005. Probabilistic modeling of tephra dispersal: Hazard assessment of a multiphase rhyolitic eruption at Tarawera, New Zealand, J. Geophys. Res.-Sol. Ea. 110(B3), doi:10.1029/2003JB002896.

Bonadonna, C., Genco, R., Gouhier, M., Pistolesi, M., Cioni, R., Alfano, F., Hoskuldsson, A., Ripepe, M., 2011. Tephra sedimentation during the 2010 Eyjafjallajokull eruption (Iceland) from deposit, radar, and satellite observations, J. Geophys. Res.-Sol. Ea. 116, doi:10.1029/2011JB008462.

Boucher, O., & Lohmann, U. (1995). The sulfate-CCN-cloud albedo effect. Tellus B, 47(3), 281-300.

Carey, S.N., Sigurdsson, H., 1982. Influence of particle aggregation on deposition of distal tephra from the May 18, 1980 eruption, of Mount St. Helens Volcano, J. Geophys. Res. 87(NB8), 7061-7072.

Carlile, J., Nelson, K., 2009. Redoubt Volcano Eruption/ Ash Synopsis - November 2008 - July 2009, Report, Federal Aviation Administration, Anchorage, Alaska.

Carlile, J., and Nelson, K.: Redoubt Volcano eruption/ ash synopsis - November 2008 - July 2009, Federal Aviation Administration, unpublished summary document, 39, 2009.

Carn, S. A., Pallister, J. S., Lara, L., Ewert, J. W., Watt, S., Prata, A. J., Thomas, R. J., and Villarosa, G.: The unexpected awakening of Chaiten Volcano, Chile, Eos, 90, 2009.

Clarisse, L., Coheur, P. F., Prata, A. J., Hurtmans, D., Razavi, A., Phulpin, T., Hadji-Lazaro, J., and Clerbaux, C.: Tracking and quantifying volcanic SO2 with IASI, the September 2007 eruption at Jebel at Tair, ACP, 8, 7723-7734, 2008.

Clarke, A. D., & Noone, K. J. (1985). Soot in the Arctic snowpack: A cause for perturbations in radiative transfer. Atmospheric Environment (1967), 19(12), 2045-2053.

Coakley, J.A., Jr., 2002: Reflectance and albedo, surface. Encyclopedia of the Atmosphere. J.R. Holton and J.A. Curry, Eds. Academic Press. 1914-1923.

Costa, A., Macedonio, G., Folch, A., 2006. A three-dimensional Eulerian model for transport and deposition of volcanic ashes, Earth and Planet. Sci. Lett. 241(3-4), 634-647, doi:10.1016/j.epsl.2005.11.019.

Courtland, L., Kruse, S.E., Connor, C.B., Connor, L.J., Savov, I.P., Martin, 2012. GPR investigation of tephra fallout, Cerro Negro volcano, Nicaragua: a method for constraining parameters used in tephra sedimentation models, Bull. Volcanol. 74, 1409-1424, doi: 10.1007/s00445-012-0603-3.

Curry, J. A., Schramm, J. L., Rossow, W. B., & Randall, D., 1996. Overview of Arctic cloud and radiation characteristics. Journal of Climate, 9(8), 1731-1764.

Dadic, R., Mullen, P. C., Schneebeli, M., Brandt, R. E., & Warren, S. G. (2013). Effects of bubbles, cracks, and volcanic tephra on the spectral albedo of bare ice near the Transantarctic Mountains: Implications for sea glaciers on Snowball Earth. Journal of Geophysical Research: Earth Surface, 118(3), 1658-1676.

Degruyter, W., Bonadonna, C., 2012. Improving on mass flow rate estimates of volcanic eruptions, Geophys. Res. Lett. 39(L16308), doi:10.1029/2012GL052566.

Deshler, T., Hofmann, D. J., Johnson, B. J., and Rozier, W. R.: Balloon-borne measurements of the Pinatubo aerosol size distribution and volatility at Laramie, Wyoming during the summer of 1991, Geophys. Res. Lett., 19, 199-202, 1992.

Deshler, T., Johnson, B. J., and Rozier, W. R.: Balloonborne measurements of Pinatubo aerosol during 1991 and 1992 at 41-degrees-n - vertical profiles, size distribution, and volatility, Geophys. Res. Lett., 20, 1435-1438, 1993.

Deshler, T.: A review of global stratospheric aerosol: Measurements, importance, life cycle, and local stratospheric aerosol, Atmos. Res., 90, 223-232, 10.1016/j.atmosres.2008.03.016, 2008.

Draxler, R. R, and Rolph, G. D.: HYSPLIT (Hybrid Single-Particle Langrangian Integrated Trajectory model) Model access via NOAA ARL READY website (http://ready.arl.noaa.gov/HYSPLIT.php), 2011.

Dufek, J., and Bergantz, G. W.: Suspended load and bed-load transport of particle-laden gravity currents: The role of particle-bed interaction, Theor. Comp. Fluid Dyn., 21, 119-145, 10.1007/s00162-007-0041-6, 2007.

Dufek, J., Manga, M., Patel, A., 2012. Granular disruption during explosive volcanic eruptions, Nature Geoscience, 5, 561-564.

Durant, A.J., Rose, W.I., 2009. Sedimentological constraints on hydrometeor-enhanced particle deposition: 1992 Eruptions of Crater Peak, Alaska, J. Volcanol. Geotherm. Res. 186(1-2), 40-59, doi:10.1016/j.jvolgeores.2009.02.004.

Ernst, G.G.J., Sparks, R.S.J., Carey, Bursik, M.I., 1996. Sedimentation from turbulent jets and plumes, J. Geophys. Res.-Sol. Ea. 101(B3), 5575-5589, doi: 10.1029/95JB01900.

Fierstein, J., Nathenson, M., 1992. Another look at calculation of fallout tephra volumes: Bulletin of Volcanology, 54, 156–167.

Folch, A., Costa, A., Macedonio, G., 2009. FALL3D: A computational model for transport and deposition of volcanic ash, Comput. Geosci. 35(6), 1334-1342, doi:10.1016/j.cageo.2008.08.008.

Flanner, M. G., Zender, C. S., Randerson, J. T., and Rasch, P. J.: Present-day climate forcing and response from black carbon in snow, J. Geophys. Res. – Atmos., 112, D11202, 10.1029/2006jd008003, 2007.

Flanner, M.G., Zender, C.S., Randerson, J.T., Rasch, P.J., 2007. Present-day climate forcing and response from black carbon in snow, J. Geophys. Res.-Atmos. 112(D11), doi:10.1029/2006JD008003.

Frogner Kockum, P. C., Herbert, R. B., & Gislason, S. R., 2006. A diverse ecosystem response to volcanic aerosols. Chemical geology, 231(1), 57-66.

Ganser, G.H., 1993. A rational approach to drag prediction of spherical and nonspherical particles, Powder Technol. 77(2), 143-152.

Griggs, R.F., 1922, The Valley of Ten Thousand Smokes: Washington, D.C., National Geographic Society, 340 p

Gu, L., Baldocchi, D. D., Wofsy, S. C., Munger, J. W., Michalsky, J. J., Urbanski, S. P., & Boden, T. A. (2003). Response of a deciduous forest to the Mount Pinatubo eruption: Enhanced photosynthesis. Science, 299(5615), 2035-2038.

Hahn, C.J., Rossow, W.B., Warren, S.G., 2001. ISCCP cloud properties associated with standard cloud types identified in individual surface observations, J. Climate 14(1), 11-28, doi:10.1175/1520-0442(2001)014<0011:ICPAWS>2.0.CO;2.

Hess, M., Koepke, P., and Schult, I.: Optical properties of aerosols and clouds: The software package OPAC, B. Am. Meteorol. Soc., 79, 831-844, 1998.

Hildreth, W., & Fierstein, J., 2012. The Novarupta-Katmai Eruption of 1912: Largest Eruption of the Twentieth Century: Centennial Perspectives (p. 259). US Department of the Interior, US Geological Survey.

Humphreys, W.J., 1913, Volcanic dust and other factors in the production of climatic changes and their possible relation to ice ages: Mount Weather Observatory Bulletin, v. 6, p. 1–34.

Jager, H., and Deshler, T.: Lidar backscatter to extinction, mass and area conversions for stratospheric aerosols based on midlatitude balloonborne size distribution measurements, Geophys. Res. Lett., 29, 1929, 10.1029/2002gl015609, 2002.

Kalnay, E., Kanamitsu, M., Kistler, R., Collins, W., Deaven, D., Gandin, L., Iredell, M., Saha, S., White, G., Woollen, J., Zhu, Y., Chelliah, M., Ebisuzaki, W., Higgins, W., Janowiak, J., Mo, K.C., Ropelewski, C., Wang, J., Leetmaa, A., Reynolds, R., Jenne, R., Joseph, D., 1996. The NCEP/NCAR 40-year reanalysis project, Bull. Am. Meteorol. Soc. 77(3), 437-471.

Kearney, C. S., and Watson, I. M.: Correcting satellite-based infrared sulfur dioxide retrievals for the presence of silicate ash, J. Geophys. Res. – Atmos., 114, D22208, 10.1029/2008jd011407, 2009.

Kimball, H. H., 1913. The effect upon atmospheric transparency of the eruption of Katmai Volcano. Monthly Weather Review, 41, 153.

Klonecki, A., Hess, P., Emmons, L., Smith, L., Orlando, J., and Blake, D.: Seasonal changes in the transport of pollutants into the Arctic troposphere-model study, J. Geophys. Res. – Atmos., 108, 8367, 10.1029/2002jd002199, 2003.

Kravitz, B., Robock, A., Bourassa, A., Deshler, T., Wu, D.C., Mattis, I., Finger, F., Hoffmann, A., Ritter, C., Bitar, L., Duck, T.J., Barnes, J.E., 2011. Simulation and observations of stratospheric aerosols from the 2009 Sarychev volcanic eruption, J. Geophys. Res.-Atmos. 116, doi:10.1029/2010JD015501.

Kustas, W. P., Rango, A., & Uijlenhoet, R. (1994). A simple energy budget algorithm for the snowmelt runoff model. Water Resources Research, 30(5), 1515-1527.

Lambert, A., Grainger, R. G., Rodgers, C. D., Taylor, F. W., Mergenthaler, J. L., Kumer, J. B., and Massie, S. T.: Global evolution of the Mt Pinatubo volcanic aerosols observed by the infrared limb-sounding instruments CLAES and ISAMS on the upper atmosphere research satellite, J. Geophys. Res. – Atmos., 102, 1495-1512, 1997.

Langmann, B., Zaksek, K., Hort, M., Duggen, S., 2010. Volcanic ash as fertilizer for the surface ocean, Atmos. Chem. Phys., 10, 3891 – 3899.

Lathem, T. L., P. Kumar, A. Nenes, J. Dufek, I. N. Sokolik, M. Trail, and A. Russell 2011, Hygroscopic properties of volcanic ash, Geophys. Res. Lett., 38, L11802, doi:10.1029/2011GL047298.

Levy, R.C., Remer, L.A., Tanre, D., Kaufman, Y.J., Ichoku, C., Holben, B.N., Livingston, J.M., Russell, P.B., Maring, H, 2003. Evaluation of the Moderate-Resolution Imaging Spectroradiometer (MODIS) retrievals of dust aerosol over the ocean during PRIDE, J. Geophys. Res.-Atmos. 108(D19), doi:10.1029/2002JD002460.

Lipman, P. W., & Mullineaux, D. R. (Eds.). (1981). The 1980 eruptions of Mount St. Helens, Washington (No. 1250). US Dept. of the Interior, US Geological Survey.

Liu, X. and Penner, J. E.: Effect of Mt. Pinatubo H2SO4/H2O aerosol on ice nucleation in the upper troposphere using a global chemistry and transport model (IMPACT), J. Geophys. Res., 107, 4141, doi:10.1029/2001JD000455, 2002.

Lohmann, U., Karcher, B., and Timmreck, C.: Impact of the Mount Pinatubo eruption on cirrus clouds formed by homogeneous freezing in the echam4 gcm, J. Geophys. Res. – Atmos., 108, 4568, 10.1029/2002jd003185, 2003.

Macedonio, G., Costa, A., Folch, A., 2008. Ash fallout scenarios at Vesuvius: Numerical simulations and implications for hazard assessment, J. Volcanol. Geotherm. Res. 178(3), 366-377, doi:10.1016/j.jvolgeores.2008.08.014.

Martin, R. S., Mather, T. A., Pyle, D. M., Power, M., Tsanev, V. I., Oppenheimer, C., Allen, A. G., Horwell, C. J., and Ward, E. P. W.: Size distributions of fine silicate and other particles in Masaya's volcanic plume, J. Geophys. Res. – Atmos., 114, D09217, 10.1029/2008jd011211, 2009.

Martinec, J., 1989. Hour-to-hour snowmelt rates and lysimeter outflow during an entire ablation period. Snow Cover and Glacier Variations, 19-28.

Mastin, L.G., Guffanti, M., Servranckx, R., Webley, P., Barsotti, S., Dean, K., Durant, A., Ewert, J.W., Neri, A., Rose, W.I., Schneider, D., Siebert, L., Stunder, B., Swanson, G., Tupper, A., Volentik, A., Waythomas, C.F., 2009. A multidisciplinary effort to assign realistic source parameters to models of volcanic ash-cloud transport and dispersion during eruptions, J. Volcanol. Geotherm. Res. 186(1-2), 10-21, doi:10.1016/j.jvolgeores.2009.01.008.

Mastin, L.G., Schwaiger, H., Schneider, D.J., Wallace, K.L., Schaefer, J., Denlinger, R.P., 2013. Injection, transport, and deposition of tephra during event 5 at Redoubt Volcano, 23 March, 2009, J. Volcanol. Geotherm. Res. 259, 201-213, doi:10.1016/j.jvolgeores.2012.04.025.

McClatchey, R. A., Fenn, R. W., Selby, J. E. A., Volz, F. E., and Garing, J. S.: Optical properties of the atmosphere, 3rd ed. AFCRL Environ. Res. Pap., 411, 108, 1972.

Melloh, R. A., 1999. A synopsis and comparison of selected snowmelt algorithms (No. CRREL-99-8). Cold Regions Research and Engineering Lab Hanover, NH.

Munoz, O., Volten, H., Hovenier, J. W., Veihelmann, B., van der Zande, W. J., Waters, L., and Rose, W. I.: Scattering matrices of volcanic ash particles of Mount St. Helens, redoubt, and mount spurr volcanoes, J. Geophys. Res. – Atmos., 109, D16201, 10.1029/2004jd004684, 2004.

Myhre, C. L., Toledano, C., Myhre, G., Stebel, K., Yttri, K. E., Aaltonen, V., Johnsrud, M., Frioud, M., Cachorro, V., De Frutos, A., Lihavainen, H., Campbell, J. R., Chaikovsky, A. P., Shiobara, M., Welton, E. J., and Torseth, K.: Regional aerosol optical properties and radiative impact of the extreme smoke event in the European Arctic in spring 2006, Atmos. Chem. Phys., 7, 5899-5915, 2007.

Neely, R. R., O. B. Toon, S. Solomon, J- P. Vernier, C. Alvarez, J. M. English, K. H. Rosenlof et al. "Recent anthropogenic increases in SO2 from Asia have minimal impact on stratospheric aerosol." Geophysical Research Letters (2013).

Neri, A., Ongaro, T. E., Menconi, G., Vitturi, M. D., Cavazzoni, C., Erbacci, G., and Baxter, P. J.: 4d simulation of explosive eruption dynamics at Vesuvius, Geophys. Res. Lett., 34, L04309, 10.1029/2006gl028597, 2007.

Niemeier, U., Timmreck, C., Graf, H.-F, Kinne, S., Rast, S., and Self, S.: Initial fate of fine ash and sulfur from large volcanic eruptions, Atmos. Chem. Phys., 9, 17531-17577, 2009.

Niemeier, U., Timmreck, C., Graf, H.F., Kinne, S., Rast, S., Self, S., 2009. Initial fate of fine ash and sulfur from large volcanic eruptions, Atmos. Chem. Phys. 9(22), 9043-9057, doi:10.5194/acp-9-9043-2009.

Painter, T. H., Dozier, J., Roberts, D. A., Davis, R. E., & Green, R. O., 2003. Retrieval of subpixel snow-covered area and grain size from imaging spectrometer data. Remote Sensing of Environment, 85(1), 64-77.

Painter, T. H., Deems, J. S., Belnap, J., Hamlet, A. F., Landry, C. C., and Udall, B.: Response of Colorado River runoff to dust radiative forcing in snow, P. Natl. Acad. Sci. USA, 10.1073/pnas.0913139107, 2010.

Painter, T.H., Deems, J.S., Belnap, J., Hamlet, A.F., Landry, C.C., Udall, B., 2010. Response of Colorado River runoff to dust radiative forcing in snow, P. Natl. Acad. Sci. USA 107(40), 17125-17130, doi:10.1073/pnas.0913139107.

Papale, P., Dobran, F., 1994. Magma flow along the volcanic conduit during the Plinian and pyroclastic flow phases of the May 18, 1980, Mount St. Helens eruption, J. Geophys. Res.-Sol. Ea. 99(B3), 4355-4373, doi: 10.1029/93JB02972.

Pasquill, F., 1974. Atmospheric Diffusion, John Wiley, New York.

Pfeiffer, T., Costa, A., Macedonio, G., 2005. A model for the numerical simulation of tephra fall deposits, J. Volcanol. Geotherm. Res. 140(4), 273-294, doi:10.1016/j.jvolgeores.2004.09.001.

Pollack, J. B., Toon, O. B., and Khare, B. N.: Optical properties of terrestial rocks and glasses, Icarus, 19, 372-389, 1973.

Prata, A. J., Carn, S. A., Stohl, A., and Kerkmann, J.: Long range transport and fate of a stratospheric volcanic cloud from Soufriere Hills Volcano, Montserrat, Atmos. Chem. Phys., 7, 5093-5103, 2007.

Pueschel, R. F., Russell, P. B., Allen, D. A., Ferry, G. V., Snetsinger, K. G., Livingston, J. M., and Verma, S.: Physical and optical-properties of the Pinatubo volcanic aerosol - aircraft observations with impactors and a sun-tracking photometer, J. Geophys. Res. – Atmos., 99, 12915-12922, 1994.

Pyle, D.M., 1989. The thickness, volume, and grain size of tephra-fall deposits. Bulletin of Volcanology, 51, 1–15.

Quinn, P. K., Shaw, G., Andrews, E., Dutton, E. G., Ruoho-Airola, T., and Gong, S. L.: Arctic haze: Current trends and knowledge gaps, Tellus B, 59, 99-114, 10.1111/j.1600-0889.2006.00238.x, 2007.

Quinn, P. K., Bates, T. S., Baum, E., Doubleday, N., Fiore, A. M., Flanner, M., Fridlind, A., Garrett, T. J., Koch, D., Menon, S., Shindell, D., Stohl, A., and Warren, S. G.: Short-lived pollutants in the Arctic: Their climate impact and possible mitigation strategies, Atmos. Chem. Phys., 8, 1723-1735, 2008.

Ramachandran, S., Ramaswamy, V., Stenchikov, G. L., and Robock, A.: Radiative impact of the Mount Pinatubo volcanic eruption: Lower stratospheric response, J. Geophys. Res. – Atmos., 105, 24409-24429, 2000.

Remer, L. A., et al.: The MODIS aerosol algorithm, products and validation. J. Atmos. Sci. 62, 947-973, 2005.

Ricchiazzi, P., Yang, S. R., Gautier, C., and Sowle, D.: Sbdart: A research and teaching software tool for plane-parallell radiative transfer in the earth's atmosphere, B. Am. Meteorol. Soc., 79, 2101-2114, 1998.

Riley, C. M., Rose, W. I., and Bluth, G. J. S.: Quantitative shape measurements of distal volcanic ash, J. Geophys. Res. – Sol. Ea., 108, 2504, 10.1029/2001jb000818, 2003.

Ritter, C., Notholt, J., Fischer, J., and Rathke, C.: Direct thermal radiative forcing of tropospheric aerosol in the arctic measured by ground based infrared spectrometry, Geophys. Res. Lett., 32, L23816, 10.1029/2005gl024331, 2005.

Robock, A., Taylor, K.E., Stenchikov, G.L., Liu, Y., 1995. GCM evaluation of a mechanism for El Nino triggering by the El Chichon ash cloud, Geophys. Res. Lett. 22(17), 2369-2372.

Robock, A.: Volcanic eruptions and climate, Rev. Geophys., 38, 191-219, 2000.

Robock, A., Ammann, C.M., Oman, L., Shindell, D., Levis, S., Stenchikov, G., 2009. Did the Toba volcanic eruption of similar to 74 ka BP produce widespread glaciation?, J. Geophys. Res.-Atmos. 114, doi:10.1029/2008JD011652.

Rolph, G. D.: Real-time environmental applications and display system (ready): Website (http://ready.arl.noaa.gov), 2011.

Rose, W.I., Chesner, C.A., 1987. Dispersal of ash in the great Toba eruption, 75 ka, Geology 15(10), 913-917, doi: 10.1130/0091-7613(1987)15<913:DOAITG>2.0.CO;2.

Rose, W.I., Durant, A.J., 2009. Fine ash content of explosive eruptions, J. Volcanol. Geotherm. Res. 186(1-2), 32-39, doi:10.1016/j.jvolgeores.2009.01.010.

Rose, W.I., Self, S., Murrow, P.J., Bonadonna, C., Durant, A.J., Ernst, G.G.J., 2008. Nature and significance of small volume fall deposits at composite volcanoes: Insights from the October 14, 1974 Fuego eruption, Guatemala, Bull. Volcanol. 70(9), 1043-1067 doi:10.1007/s00445-007-0187-5.

Rose, W. I., Bluth, G. J. S., and Watson, I. M.: Ice in volcanic clouds: When and where?, Proceedings of the 2nd International Conference on Volcanic Ash and Aviation Safety, OFCM Washington, D. C., 2004.

Rose, W. I., and Durant, A. J.: Fine ash content of explosive eruptions, J. Volcanol. Geoth. Res., 186, 32-39, 10.1016/j.jvolgeores.2009.01.010, 2009.

Russell, P. B., and al., e.: Global to microscale evolution of the Pinatubo volcanic aerosol, derived from diverse measurements and analyses, J. Geophys. Res., 101, 18745-18763, 1996.

Schaefer, J.R., 2012. The 2009 eruption of Redoubt Volcano, Alaska, with contributions by Bull, K.P., Cameron, C.E., Coombs, M.L., Diefenbach, A.K., Lopez, T., McNutt, S.R., Neal, C.A., Payne, A.L., Power, J.A., Schneider, D.J., Scott, W.E., Snedigar, S.F., Thompson, G., Wallace, K.L., Waythomas, C.F., Webley, P.W., Werner, C.A. Report of Investigations RI 2011-5, State of Alaska, Department of Natural Resources, Division of Geological and Geophysical Surveys, Fairbanks, Alaska.

Schaefer, J.R., Wallace, K.L., 2012. Ash fall contour map of the 2009 eruption of Redoubt Volcano, Alaska: Digital shapefiles of contours and sample locations: Miscellaneous Publication MP 143, State of Alaska, Department of Natural Resources, Division of Geological & Geophysical Surveys, Fairbanks, Alaska, USA.

Schmehl, K.J., Haupt, S.E., Pavolonis, M.J., 2012. A Genetic Algorithm Variational Approach to Data Assimilation and Application to Volcanic Emissions, Pure and Appl.Geophys. 169(3), 519-537, doi: 10.1007/s00024-011-0385-0.

Scollo, S., Folch, A., Costa, A., 2008. A parametric and comparative study of different tephra fallout models, J. Volcanol. Geotherm. Res. 176(2), 199-211, doi:10.1016/j.jvolgeores.2008.04.002.

Scollo, S., Prestifilippo, M., Coltelli, M., Peterson, R.A.,, Spata, G., 2011. A statistical approach to evaluate the tephra deposit and ash concentration from PUFF model forecasts, J. Volcanol. Geotherm. Res. 200(3-4), 129-142, doi:10.1016/j.jvolgeores.2010.12.004.

Scott K.M., Macias, J.L., Naranjo, A., Rodriguez, S., McGeehin, J.P., 2001. Catastrophic debris flows transformed from landslides in volcanic terrains: mobility, hazard assessment, and mitigation strategies, Professional Paper 1630, pp. 27, United States Geological Survey, Denver, Colorado.

Scott, W.E., McGimsey, R.G., 1994. Character, mass, distribution, and origin of tephra-fall deposits of the 1989-1990 eruption of Redoubt Volcano, south-central Alaska, J. Volcanol. Geotherm. Res. 62, 251-272.

Scott, W. E., and McGimsey, R. G.: Character, mass, distribution, and origin of tephra-fall deposits of the 1989-1990 eruption of redoubt volcano, south-central Alaska, J. Volcanol. Geoth. Res., 62, 251-272, 1994.

Seinfeld J. H., Pandis, S. N.,2006. Atmospheric Chemistry and Physics: From Air Pollution to Climate Change, 2nd edition, J. Wiley, New York.

Shaw, G. E., and Stamnes, K.: Arctic haze: Perturbation of the polar radiation budget, Ann. NY Acad. Sci., 338, 533-539, 1980.

Shindell, D., 2007. Local and remote contributions to Arctic warming, Geophys. Res. Lett., 34, doi:10.1029/2007GL030221.

Simkin T, Siebert L.,1994. *Volcanoes of the World* (2nd edition) Tucson: Geoscience Press, 369 pp.

Skiles, S. M., Painter, T. H., Deems, J. S., Bryant, A. C., & Landry, C. C. (2012). Dust radiative forcing in snow of the Upper Colorado River Basin: 2. Interannual variability in radiative forcing and snowmelt rates. Water Resources Research, 48(7).

Sokolik, I.N., J. A. Curry, and V. Radionov, Interactions of Arctic aerosols with land-cover and land-use changes in Northern Eurasia and their role in the Arctic climate system. In *Arctic land-cover and land-use in a changing climate: Focus on Eurasia*, G.Gutman and A. Reissell (Eds.), Springer, 2011.

Spinetti, C., Corradini, S., Carboni, E., Thomas, G., Grainger, R., and Buongiorno, M. F.: Mt. Etna volcanic aerosol and ash retrievals using MERIS and AATSR data, Proceedings of the 2nd MERIS/(A)ATSR Workshop, Frascati, Italy, 2008.

Steensen, T., Stuefer, M., Webley, P., Grell, G., Freitas, S., 2013. Qualitative comparison of Mount Redoubt 2009 volcanic clouds using the PUFF and WRF-Chem dispersion models and satellite remote sensing data, J. Volcanol. and Geotherm. Res. 259, 235-247, doi:10.1016/j.jvolgeores.2012.02.018.

Stenchikov, G. L., Kirchner, I., Robock, A., Graf, H. F., Antuna, J. C., Grainger, R. G., Lambert, A., and Thomason, L.: Radiative forcing from the 1991 Mount Pinatubo volcanic eruption, J. Geophys. Res. – Atmos.., 103, 13837-13857, 1998.

Stier, P., Feichter, J., Kinne, S., Kloster, S., Vignati, E., Wilson, J., Ganzeveld, L., Tegen, I., Werner, M., Balkanski, Y., Schulz, M., Boucher, O., Minikin, A., and Petzold, A.: The aerosol-climate model echam5-ham, Atmos. Chem. Phys., 5, 1125-1156, 2005.

Stohl, A.: Characteristics of atmospheric transport into the Arctic troposphere, J. Geophys. Res. – Atmos., 111, D11306, 10.1029/2005jd006888, 2006.

Stone, R. S., Herber, A., Vitale, V., Mazzola, M., Lupi, A., Schnell, R. C., Dutton, E. G., Liu, P. S. K., Li, S. M., Dethloff, K., Lampert, A., Ritter, C., Stock, M., Neuber, R., and Maturilli, M.: A three-dimensional characterization of arctic aerosols from airborne sun photometer observations: Pam-arcmip, april 2009, J. Geophys. Res. – Atmos., 115, D13203, 10.1029/2009jd013605.

Stone, R. S., Anderson, G. P., Andrews, E., Dutton, E. G., and Shettle, E. P.: Incursions and radiative impact of Asian dust in northern Alaska, Geophys. Res. Lett., 34, L14815, 10.1029/2007gl029878, 2007.

Stone, R. S., Anderson, G. P., Shettle, E. P., Andrews, E., Loukachine, K., Dutton, E. G., Schaaf, C., and Roman, M. O.: Radiative impact of boreal smoke in the arctic: Observed and modeled, J. Geophys. Res. – Atmos., 113, D14s16, 10.1029/2007jd009657, 2008.

Stone, R.S., Anderson, G.P., Shettle, E.P., Andrews, E., Loukachine, K., Dutton, E.G., Schaaf, C., Roman, M.O., 2008. Radiative impact of boreal smoke in the Arctic: Observed and modeled, J. Geophys. Res.-Atmos. 113(D14), doi:10.1029/2007JD009657.

Stuefer, M., Freitas, S.R., Grell, G., Webley, P., Peckham, S., McKeen, S.A., Egan, S.D., 2013. Inclusion of ash and SO2 emissions from volcanic eruptions in WRF-Chem: development and some applications, Geosci. Model Dev. 6(2), 457-468, doi:10.5194/gmd-6-457-2013.

Swanson, S.E., Nye, C.J., Miller, T.P., Avery, V.F., 1994. Geochemistry of the 1989-1990 eruption of Redoubt Volcano: Part II, Evidence from mineral and glass chemistry, J. Volcanol. and Geotherm. Res. 62(1-4), 453-468.

Telling, J.W., Dufek, J., Shaikh, A., 2013. Ash aggregation in explosive volcanic eruptions, Geophys. Res. Lett. 40(10), 2355-2360, doi: 10.1002/grl.50376.

Textor, C., Graf, H. F., Herzog, M., Oberhuber, J. M., Rose, W. I., and Ernst, G. G. J.: Volcanic particle aggregation in explosive eruption columns. Part I: Parameterization of the microphysics of hydrometeors and ash, J. Volcanol. Geoth. Res., 150, 359-377, 10.1016/j.jvolgeores.2005.09.007, 2006.

Thomas, H. E., Watson, I. M., Kearney, C., Carn, S. A., and Murray, S. J.: A multi-sensor comparison of sulphur dioxide emissions from the 2005 eruption of Sierra Negra Volcano, Galapagos Islands, Remote Sens. Environ., 113, 1331-1342, 10.1016/j.rse.2009.02.019, 2009.

Thomason, L. W., and Pitts, M. C.: CALIPSO observations of volcanic aerosol in the stratosphere, Proceedings of SPIE, 2008.

Thordarson, T., & Self, S. (2003). Atmospheric and environmental effects of the 1783–1784 Laki eruption: a review and reassessment. Journal of Geophysical Research, 108(D1), 4011.

Toon, O. B., McKay, C. P., Ackerman, T. P., & Santhanam, K. (1989). Rapid calculation of radiative heating rates and photodissociation rates in inhomogeneous multiple scattering atmospheres. Journal of Geophysical Research: Atmospheres (1984–2012), 94(D13), 16287-16301.

Torres, O., Tanskanen, A., Veihelmann, B., Ahn, C., Braak, R., Bhartia, P.K., Veefkind, P., Levelt, P., 2007. Aerosols and surface UV products from Ozone Monitoring Instrument observations: An overview, J. Geophys. Res.-Atmos. 112(D24), doi:10.1029/2007JD008809.

Torres, O., Tanskanen, A., Veihelmann, B., Ahn, C., Braak, R., Bhartia, P. K., Veefkind, P., and Levelt, P.: Aerosols and surface UV products from ozone monitoring instrument observations: An overview, J. Geophys. Res. – Atmos., 112, D24s47, 10.1029/2007jd008809, 2007.

Van Eaton, A.R., Herzog, M., Wilson, C.J.N., McGregor, J., 2012. Ascent dynamics of large phreatomagmatic eruption clouds: The role of microphysics, J. Geophys. Res.-Sol. Ea. 117, doi:10.1029/2011JB008892.

Viollier, M.: Teledetection des concentrations de seston et pigments chlorophylliens contenus dans l'Ocean, These de Doctorat d'Etat, 503, 1980.

Wallace, K.L, Schaefer, J.R., Coombs, M.L., 2013. Character, mass, distribution, and origin of tephra-fall deposits from the 2009 eruption of Redoubt Volcano, Alaska—Highlighting the significance of particle aggregation, J. Volcanol. Geotherm. Res. 259, 145-169, doi:10.1016/j.jvolgeores.2012.09.015.

Warren, S. G., Brandt, R. E., & Grenfell, T. C. (2006). Visible and near-ultraviolet absorption spectrum of ice from transmission of solar radiation into snow. Applied optics, 45(21), 5320-5334.

Warren, S. G., & Wiscombe, W. J. (1985). Dirty snow after nuclear war. Nature, 313(6002), 467-470.

Williams, E. R., and McNutt, S. R.: Total water contents in volcanic eruption clouds and implications for electrification and lightning, in: Research signpost, recent progress in lightning physics, edited by: Pontikis, C., Research Signpost, Kerala, India, 81-93, 2005.

Wilson, L., Sparks, R.S.J., Huang, T.C., Watkins, N.D., 1978. Control of volcanic column heights by eruption energetic and dynamics, J. Geophys. Res. 83(NB4), 1829-1836.

Wilson, L., Walker, G.P.L., 1987. Explosive volcanic eruptions -- Part VI. Ejecta dispersal in Plinian eruptions: the control of eruption conditions and atmospheric properties, Geophys. J. Roy. Astr. S. 89(2), 657-679, doi: 10.1111/j.1365-246X.1987.tb05186.x.

Wiscombe, W. J., and Warren, S. G.: A model for the spectral albedo of snow. I: pure snow, J. Atmos. Sci., 37, 2712-2733, 1980.

Yuan, T., Remer, L. A., and Yu, H.: Microphysical, macrophysical and radiative signatures of volcanic aerosols in trade wind cumulus observed by the A-Train, Atmos. Chem. Phys. Discuss., 11, 6415-6455, 2011.

Yue, G. K., Poole, L. R., Wang, P. H., and Chiou, E. W.: Stratospheric aerosol acidity, density, and refractive-index deduced from SAGE-II and NMC temperature data, J. Geophys. Res. – Atmos., 99, 3727-3738, 1994.

Young, C.L., Sokolik, I.N., Dufek, J., 2012. Regional radiative impact of volcanic aerosol from the 2009 eruption of Mt. Redoubt, Atmos. Chem. Phys. 12(8), 3699-3715, doi:10.5194/acp-12-3699-20.

Young, C.L., Dufek, J., Sokolik, I.N., 2014. Assessment of depositional ash loading from the 2009 eruption of Mt. Redoubt, J. Volcanol. Geotherm. Res.

VITA

CINDY L. YOUNG

Cindy L. Young was born in Appalachia. She attended primary school in Okinawa, Japan. The rest of her grade school education was completed in Blairsville, Georgia. In school, Ms. Young participated in academic team, drama, and chorus. During high school, she also attended Piedmont College in Demorest, Georgia and Young Harris College in Young Harris, Georgia. At Young Harris, she tutored other students in math, enjoyed astronomy and astrophotography, and received a scholarship for her study of math and science. Ms. Young graduated high school in 2001 and earned a B.S. in Earth and Atmospheric Sciences from Georgia Tech in 2005, which she attended through receiving the Georgia HOPE scholarship throughout her undergraduate education. Her senior project involved the chemical analysis of soil and rainfall samples collected at Panola Mount Research Watershed. In 2009, she received a M.S. in Earth and Atmospheric Sciences at Georgia Tech, focusing in chemical oceanography. Her thesis title was: "Marine dissolved organic phosphorus composition: insights from samples recovered using combined electrodialysis/revere osmosis."

Ms. Young has always held an interest in satellite remote sensing of earth and planetary systems, which led her to pursue her doctorate in this field in 2009. Her interdisciplinary research has allowed her to travel to many interesting places, including Mt. St. Helens and Eyjafjallajökull. She will graduate with a PhD in Earth and Atmospheric Sciences in May 2014. During her graduate studies, Ms. Young has published two papers and submitted one paper to peer-reviewed journals, has two papers in progress at the time of writing this dissertation, and has presented at five academic conferences. During her time at Georgia Tech, she has been of member of the Shaolin Kung Fu and Tai Chi club, where she assisted with teaching students martial arts. She has also been active in rescuing homeless cats and the trap, spay/neuter, and release of feral cats. When she is not researching, she enjoys being physically active, especially outdoors, and spending time with the important people and animals in her life. In March 2014, Ms. Young will begin a postdoctoral position at Emory University in environmental health and climate change.